UNIVERSITÀ DEGLI STUDI ROMA TRE

Dipartimento di Fisica "Edoardo Amaldi"

Research Doctorate in Physics

Course XXIII

Computer Simulations on Supercooled Aqueous Solutions: the Effect of Solutes on the Liquid-Liquid Critical Point

by

Dario Corradini

Academic Year 2010-2011

Supervisor
Prof. Paola Gallo

Coordinator
Prof. Guido Altarelli

Eau, tu n'as ni goût, ni couleur, ni arôme, on ne peut pas te définir, on te goûte sans te connaître. Tu n'es pas nécessaire à la vie : tu es la vie. Tu nous pénètres d'un plaisir qui ne s'explique point par les sens.

Antoine de Saint-Exupéry, *Terre des hommes* (1939).

Water, thou hast no taste, no color, no odor; canst not be defined, art relished while ever mysterious. Not necessary to life, but rather life itself, thou fillest us with a gratification that exceeds the delight of the senses.

Antoine de Saint-Exupéry, *Wind, Sand and Stars* (1939).

Contents

Chapter 1

Introduction

Water is a special substance. It is the medium in which most biological processes take place and it is the most abundant substance on Earth and in the human body [1, 2]. But water is special also because its physical properties are anomalous. In fact, despite the apparent simplicity of the water molecule, water behaves in most respects in an unexpected manner. The thermodynamics, dynamics and structure of water, all present features that distinguish water from simple liquids [3–6]. A large body of scientific works has been devoted to the understanding of the origin of the anomalous properties of water. Although many advancements have been achieved and several scenarios have been formulated in which to frame the behaviour of water [7–10], there remain many mysteries yet to be solved.

At ambient pressure, water is found in the stable liquid phase from $T = 373$ K (the boiling point) to $T = 273$ K (the freezing point). However under particular experimental conditions, water can persist in a metastable liquid phase in wider range of temperatures, from $T = 553$ K (the superheating limit) to $T = 235$ K (the supercooling limit or temperature of homogeneous nucleation) [5, 6]. A so called no man's land [11] extends from $T = 235$ K down to $T = 150$ K (close to the glass transition temperature $T = 136$ K). In this region water might still exist in the metastable liquid phase but current experimental techniques do not allow to access points in this region with a succession of metastable states, even though it would not be prohibited by thermodynamic constraints [5]. The homogeneous nucleation is in fact a kinetic constraint and it is function of the cooling rate and of the observation time [5].

The supercooled region of water is particularly interesting because many anomalies of water appear to be especially pronounced in this region [3–6]. Furthermore the so called liquid-liquid critical point (LLCP) scenario [7] predicts the existence, in the no man's land, of two distinct liquid phases,

the low density liquid (LDL) and the high density liquid (HDL). These two phases would be separated by a first order phase transition line, ending in a critical point, above which the difference between the two phases vanishes and the ordinary liquid phase is found. The LLCP scenario was first formulated on the basis on computer simulations [7] and its plausibility has been confirmed by a large number of theoretical and computer simulation works [3,12–30]. Experimentally, indirect evidence of the presence of a LLCP has been found [11,31]. However because of its location in the no man's land, it remains not directly accessible in experiments and computer simulations are the main method of investigation of this intriguing hypothesis.

Sometimes it is stated that the ultimate understanding of biology requires first the comprehension of water [3]. This is even more true for aqueous solutions. In fact aqueous solutions are ubiquitous in nature, thanks to another peculiar characteristic of water, that of being an extraordinary solvent. The study of the properties of aqueous solutions at low temperatures can be of the utter significance for the investigation of diverse phenomena spanning from the cryopreservation of living cells [32] to cloud formation [33], from globular protein folding [34] to self-assembling [35, 36].

From a more fundamental point view, the investigation of aqueous solutions can help shedding light on the numerous mysteries of bulk water. In fact the presence of solutes in water is known to affect thermodynamic quantities such as the boiling point, the freezing point and the vapour-liquid critical point [37–40]. Solutions of electrolytes are more easily supercooled than bulk water, as the temperature of homogeneous nucleation shifts downward upon increasing the solutes content [41]. Thus the addition of solutes to water may be a method to extend the region where liquid water is experimentally observable and possibly to locate experimentally the LLCP. In order to prevent crystallization, experiments have been conducted on water confined in small pores and they confirmed the LLCP hypothesis, with the finding of a first order phase transition line [42]. We will show with our results that a viable alternative for the measuring of the LLCP in not confined samples can be the investigation of aqueous solutions.

In this Ph. D. thesis, we present the results of three sets of computer simulation studies on bulk water and on aqueous solutions, the PR-TIP4P set [43–48], the JJ-TIP4P [49,50] set and the HS-JRP set [51]. The first two sets are simulated using the standard molecular dynamics (MD) algorithm and they differ by the ionic potential employed. The last one is simulated using the discrete molecular dynamics (DMD) algorithm.

In the PR-TIP4P set are included the MD simulations performed on bulk TIP4P water and on $c = 0.67, 1.36$ and 2.10 mol/kg solutions of sodium chloride, NaCl(aq), in TIP4P water. The ionic potential for this set was

taken from Pettitt and Rossky (PR) [52].

The JJ-TIP4P set consists in the extensive MD simulations performed on bulk TIP4P water and on $c = 0.67$ mol/kg NaCl(aq) with the aim of locating the position of the LLCP in both systems. The ionic potential for this set was taken from Jensen and Jorgensen (JJ) [53].

The HS-JRP set is composed by the DMD simulations performed on mixtures of hard spheres (HS) and Jagla ramp potential (JRP) particles, as models for solutions of hydrophobic solutes in water. The mole fractions investigated are $x_{HS} = 0.10, 0.15, 0.20$ and 0.50. Also this work is focused on the LLCP.

The abstracts of the papers published on these sets of simulations can be found in the section Publications and Presentations (page 135).

In the following we illustrate the structure of the thesis, anticipating the main results obtained from each set of simulations.

In Chap. 2 we describe the general context in which our studies are performed. The main features of the water molecule and of its hydrogen bond network are presented. Then we review the ranges of stability and metastability of liquid water, with particular regard to the supercooled region. After a description of the most striking water anomalies, we discuss the scenarios proposed to explain their appearance. The LLCP scenario is treated in greater detail because it is the one we work in when presenting the results. The properties of solutions of polar and apolar solute, relevant to the discussion of the results, are finally presented.

Chap. 3 treats the main elements of the MD technique, that has been employed for the simulations in the PR-TIP4P and in the JJ-TIP4P sets. After showing the general ideas of MD, we describe in more details the integration algorithm, the application of thermostats and barostats and the Ewald summation method for the treatment of long range interactions.

In Chap. 4 we report the results obtained from the PR-TIP4P set. First, the specific simulation details for this set are given, then the results are presented. A study conducted on the dependence of the thermodynamic results on the size of the system reveals that no large differences exist for sizes $N_{tot} = 256, 512, 1024$, where N_{tot} is the total number of particles contained in the simulation box. The analysis of the isotherms and the isochores of bulk water and of the solutions at different concentrations allowed the determination of important thermodynamic loci such as the temperature of maximum density (TMD) line and the liquid-gas limit of mechanical stability (LG-LMS). The results are also compared with those obtained from TIP4P water confined in a hydrophobic environment of soft spheres [54]. We report here in Fig. 1.1 the comparison of the TMD and LG-LMS lines obtained for bulk water, for $c = 0.67, 1.36$ and 2.10 mol/kg NaCl(aq) and for water in a

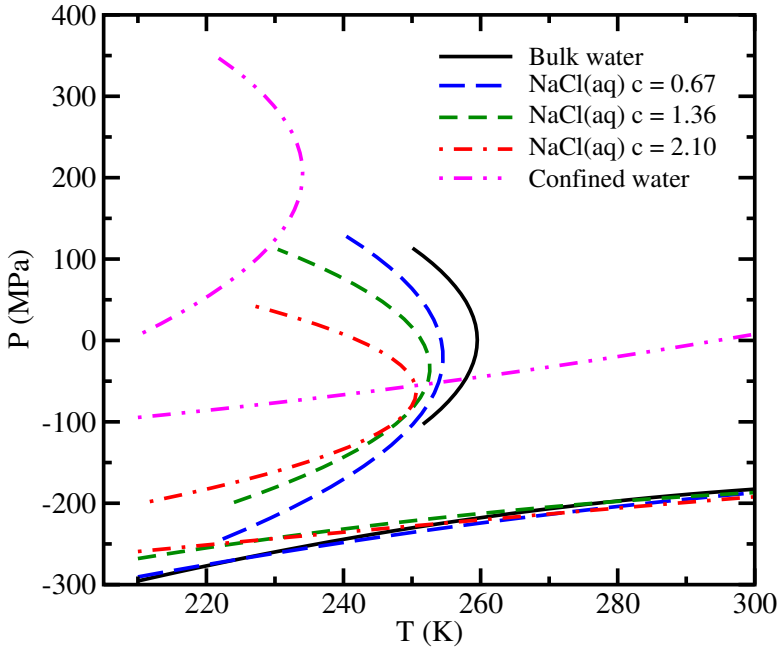

Figure 1.1: PR-TIP4P set: TMD and LG-LMS lines for bulk water, for $c = 0.67, 1.36$ and 2.10 mol/kg NaCl(aq) and for water confined in a hydrophobic environment of soft spheres [54].

hydrophobic environment.

The addition of polar solutes, namely sodium chloride, to water does not lead to a significant modification of the LG-LMS line with respect to bulk water, while the TMD line moves to lower temperatures and pressures with also a narrowing of the amplitude of the curve, upon increasing the concentration of solutes. In the case of water in a hydrophobic environment both the LG-LMS and the TMD line shift to higher pressures due to excluded volume effects, with the TMD also moving to lower temperatures, with respect to bulk water. The thermodynamics of the NaCl(aq) solutions also shows indications of the approach to liquid-liquid coexistence, with inflections in the low temperature isotherms and the appearance of minima in the behaviour of the potential energy as a function of density.

The structural properties of $c = 1.36$ mol/kg NaCl(aq) are then compared to water in the hydrophobic environment of soft spheres [54]. The similarities and the differences in the hydration structure of ions (hydrophilic) and soft spheres (hydrophobic) are analysed as functions of temperature and density.

The results for the JJ-TIP4P set are reported in Chap. 5. After the specific simulation details are provided, a comparison of the thermodynamics

obtained with the use of the PR and of the JJ ion parameters is discussed, showing that the two sets of parameters yield consistent results. The large body of thermodynamic state points simulated for bulk TIP4P water and for $c = 0.67$ mol/kg NaCl(aq) are shown in the isochores planes, together with the estimated positions of the LLCP. The results obtained for TIP4P bulk water are compared with available experimental results and a shift of the simulated phase diagram is proposed to match it to the experimental one. On the basis of the comparison of the simulated and the experimental TMD point at ambient pressure for the NaCl(aq) we hypothesize that the same shift applied to bulk TIP4P water can be applied in the solution. From these considerations we predict the phase diagrams of bulk water and $c = 0.67$ mol/kg NaCl(aq) as they should be measurable in experiments. They are shown in Fig. 1.2.

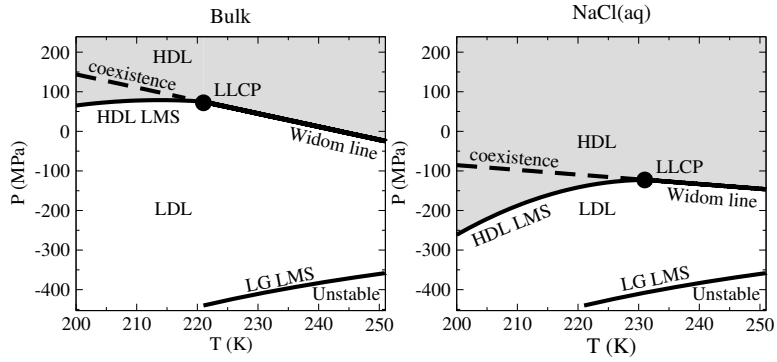

Figure 1.2: JJ-TIP4P set: Schematisation of the HDL-LDL phase diagrams obtained from MD simulations for bulk water (left panel) and $c = 0.67$ mol/kg (right panel) after the application of the shift needed to match experimental values. The position of the LLCP is $T_c \simeq 220$ K and $P \simeq 100$ MPa for bulk water and $T_c \simeq 230$ K and $P \simeq -120$ MPa for NaCl(aq).

The LLCP in NaCl(aq) moves to lower pressures and higher temperatures with respect to bulk water and importantly it should fall above the homogeneous nucleation line of the solution, making an experimental observation of the LLCP in NaCl(aq) feasible. From the comparison of the phase diagrams we can also notice that the LDL phase restricts in the solutions, with respect bulk water.

The structure of the LDL and HDL phases both in bulk water and in NaCl(aq) is also investigated and it is found that the structure of the LDL phase is more affected by the presence of ions with respect to the HDL phase. A possible explanation, in terms of the substitution of the oxygen by the chloride ion in the coordination shells, is proposed.

In Chap. 6 we report the results for the HS-JRP set. The systems studied in this set are more idealized with respect to the PR-TIP4P and the JJ-TIP4P set. Hydrophobic solutes are modeled with hard spheres (HS) while water is modeled with the Jagla ramp potential (JRP) particles [12, 55–57]. The JRP potential is known to be able to reproduce water anomalies [17, 58, 59]. For this set, the DMD technique was used as it is more suitable for dealing with ideal models containing hard cores. The main concepts of DMD are illustrated in the first section of Chap. 6, followed by the specific details for the studied systems. Then the results on the thermodynamics of the $x_{HS} = 0.10, 0.15, 0.20$ and 0.50 mixtures of HS and JRP particles are presented. The analysis of the isochores and isotherms plane permitted the determination of the LLCP in all systems. It is in fact present up to the highest mole fraction of solutes, shifting progressively to higher pressures and lower temperatures. On the basis of a rotation of the phase diagram, performed to match the sign of the slope of the liquid-liquid coexistence line of the bulk JRP particles to that of real water, a prediction for the shift of the LLCP in experimental solutions of hydrophobic solutes is obtained. We expect the LLCP to move to higher pressures and temperatures. This is consistent with the results obtained by Gallo and Rovere on water in a

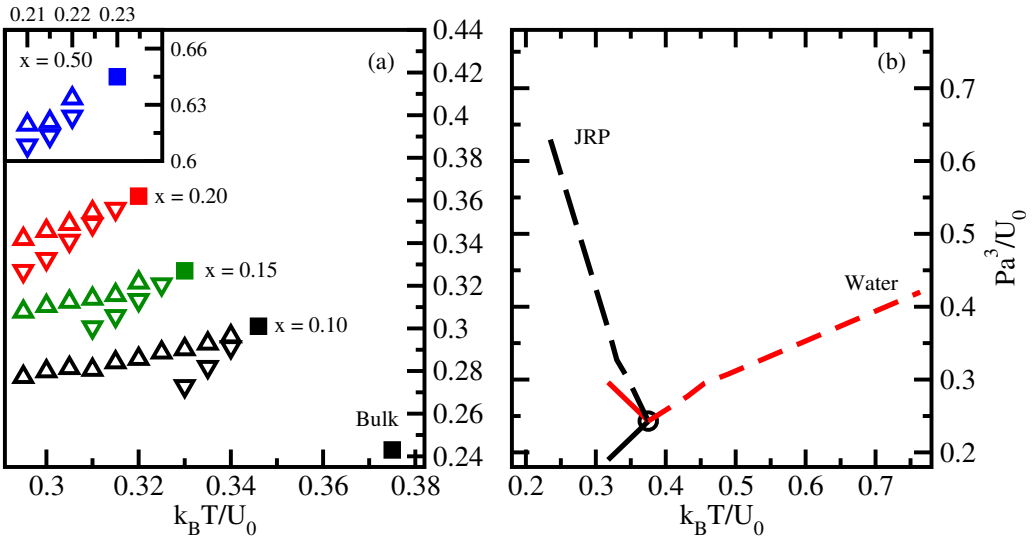

Figure 1.3: HS-JRP set: (a) LLCP (squares), LDL (triangles up) and HDL (triangles down) LMS points for $x_{HS} = 0.10, 0.15, 0.20$. In the inset same quantities for $x_{HS} = 0.50$. (b) LLCP (circle) and LL coexistence line (dark solid line) for bulk water from Ref. [12] and the critical line of the mixtures (dark dashed line), calculated in this work. The rotated coexistence line (light solid line) and mixture critical line (light dashed line) are also shown. Pressures and temperatures are in reduced units.

hydrophobic environment [54], if we hypothesize that, in analogy with the case of NaCl(aq), the TMD line and the LLCP get closer to each other in solutions. In Fig. 1.3(a) the LLCP for bulk JRP and for the $x_{HS} = 0.10, 0.15, 0.20$ and 0.50 mixtures are shown together with the HDL and LDL limit of mechanical stability (LMS) lines. In Fig. 1.3(b) the LLCP of bulk JRP particles, the liquid-liquid coexistence line [12] and the mixture critical line [51] are shown, together with the same quantities after the rotation mentioned above.

The diffusive behaviour of the mixture is also analysed. We find the diffusivity anomaly, with the appearance of extrema in the behaviour of the diffusion coefficient at constant temperature as a function of density, is preserved up to the highest HS mole fraction. For $x_{HS} = 0.10, 0.15, 0.20$ a crossover in the behaviour of the diffusion coefficient at constant pressure, is observed above the LLCP upon crossing the Widom line, in analogy with what found in the bulk JRP system. The solute-solute structure along the critical isochores is also discussed.

In Chap. 7 the conclusions for the three sets studied in this thesis are summarized.

Finally in the separate section Publications and Presentation, a list of the published papers with the respective abstracts is reported along with a list of oral and poster presentations given by myself relative to the systems studied in this thesis. A list of the acronyms and abbreviations used throughout the thesis and the Acknowledgments precede the Bibliography.

Chapter 2

Features of supercooled water and aqueous solutions

The main motivations for the studies presented in this thesis and a general introduction to the open questions on supercooled water and aqueous solutions are given in this chapter. An exhaustive account of all the often surprising aspects of water would probably require many books. Here we shall review those properties relevant to the discussion of the original results obtained, presented in Chap. 4, 5 and 6.

Water has a paramount importance not only in nature but also in virtually every activity of human society, like agriculture, industry, travel, climate, public health and so on [1, 2]. When we think of a liquid, our experience leads us instantaneously to water. Yet from a scientific perspective water is not a common liquid. Indeed water presents many *anomalies* when compared to the behaviour expected for an ordinary liquid.

In Sec. 2.1 the structure and the properties of the single water molecule are described, together with the main characteristics of the hydrogen bond network that water molecules are able to build up.

Stable phases of water include the vapour phase, the liquid phase and twelve different forms of solid phases, of which ordinary hexagonal ice I_h is the most common (at ambient pressure). Beyond stable phases, water can be found in metastable phases. These can be solid phases, both crystalline and amorphous and liquid phases. In Sec. 2.2 a description of the known stable and metastable phases of water is given.

The anomalies of liquid water are discussed in Sec. 2.3. The behaviour of water is anomalous in every respect. In fact thermodynamics, dynamics and structure of water are all characterized by the appearance of unexpected features. Many authors have pointed out that life on Earth strongly depends on the anomalous properties of water (see for example Refs. [1, 2, 6]). In

particular the melting point, the boiling point and the vapour-liquid critical point can be found at temperatures much higher with respect to compounds built with elements close to oxygen in the periodic table, like NH_3, $CHCl_3$ or CH_3CH_3. This allows Earth to be bathed by liquid water. The large heat capacity and high thermal conductivity of water contribute to thermal regulation both in the environment and in living organisms. Importantly the density of water does not increase upon cooling but it has a maximum at 4° C ($T = 277$ K). This causes the freezing of lakes and oceans to proceed from top down, so that the layers of ice formed at the interface with air insulates the bottom body of water, preventing further freezing and allowing the survival of living organisms.

The origin of the appearance of anomalies in stable and metastable water is not yet fully understood. In the past thirty years several *scenarios* have been proposed to explain the striking properties of water. These scenarios are described in Sec. 2.4, with particular regard for the liquid-liquid critical point (LLCP) scenario.

Another well known property of water is that of being an excellent solvent, particularly for polar and ionic compounds of salts. The anomalous properties of water are affected by the presence of solutes and are in general preserved for low and moderate concentrations. The effect of the presence of solutes on the anomalous behaviour of water is described in Sec. 2.5, both for polar and apolar solutes.

2.1 The water molecule and the hydrogen bond

The single water molecule is a small planar v-shaped molecule, with an oxygen atom in the central vertex and two hydrogen atoms in the external vertices. The experimental value in the gas phase for the H-O-H angle is $\theta = 104.474°$ and for the intramolecular O-H distance it is $d_{\text{O-H}} = 0.95718$ Å [60]. The most exact computed values for these quantities with *ab initio* calculations are $\theta = 104.500°$ and $d_{\text{O-H}} = 0.957854$ Å [61]. A single water molecule is shown in Fig. 2.1.

Water molecules are polar because of the large difference in the electronegativity of the two species, $\Delta\chi = \chi_{\text{O}} - \chi_{\text{H}} = 3.44 - 2.20 = 1.24$. The electrons of the two hydrogen atoms are strongly attracted by the oxygen and move towards it, leaving the protons of the hydrogen atoms partially unscreened. Thus the charge distribution is characterized by partial charges. An estimate of the partial charges is $\delta q \simeq +0.7e$ for the oxygen atom and

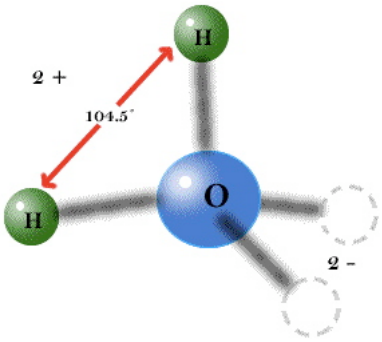

Figure 2.1: A single water molecule. In the gas phase, the H-O-H angle is 104.474° and the intramolecular O-H distance is $d_{\text{O-H}} = 0.95718$ Å [60]. The two hydrogen atoms and the the lone pairs of oxygen form a tetrahedral structure.

$\delta q \simeq +0.35e$ for the hydrogen atoms [62]. The valence electrons of the oxygen atom form two lone pairs. These lone pairs and the two hydrogen atoms form an approximately tetrahedral structure, see Fig. 2.1. The dipole moment of the water molecule in the gas phase is $\mu = 1.85$ D [63]. For a completely ionic O-H bond the value of the dipole moment would be 5.61 D. Hence it has been proposed that the O-H bond can be considered as 1/3 ionic and 2/3 covalent [64].

One of the most important features of the collective behaviour of water molecules is the presence of the hydrogen bond. In general, hydrogen bonding occurs when a hydrogen atom is strongly attracted by two atoms, effectively forming a bond between the two. Typically it happens when a hydrogen atom with a partial positive charge finds itself between two atoms of oxygen or nitrogen with a partial negative charge. Nevertheless hydrogen bonding can be found also in compounds like HF_2^-, between water and halide ions like F^-, Cl^-, Br^-, I^- (the binding energy decreases with increasing ionic radius) or even between water and xenon [65].

Ordinary ice I_h, the stable form of water below $T = 273$ K at ambient pressure, is the best example of the ability of water to form a network of hydrogen bonds. Each molecule has four first-neighbours and it behaves as donor of hydrogen for two of them and as acceptor of hydrogen for the other two. As a result, a space-filling network is formed, with the first four neighbours located at the vertices of a regular tetrahedron surrounding the central oxygen atom. The strong directionality of the bond determines the presence of many voids in the ice structure. For this reason the network formed by the hydrogen bonds is called an *open* network and most importantly when ice melts, at ambient pressure, the loss of long range order allows a closer

packing of water molecules, with a consequent increase in density by about 9%.

The energy associated with the hydrogen bond is circa 20 kJ/mol, roughly $8k_BT$ at ambient temperature. This energy is much bigger than the energy associated with dipole-dipole interactions, circa 1 kJ/mol. Therefore the hydrogen bond is a strong bond for liquid phases, even if it is much weaker than a covalent bond, circa 400 kJ/mol. The fact that the latent heat of fusion is low with respect to the latent heat of sublimation indicates that in the liquid state, most hydrogen bonds are preserved. In fact in the liquid state, close to the melting point, the local tetrahedral symmetry is maintained even if the order is short-ranged. Most of the peculiar properties of liquid water, that will be covered in the following sections, arise as consequences of the hydrogen bonded structure of water.

2.2 Stable and metastable water

At ambient conditions, $T = 298$ K and $P = 1$ atm, water is in the liquid state. The ranges of temperatures and pressures for which it can be found in this state are significantly wider with respect to most substances. Water is in fact one of the few inorganic substances in the liquid state at ambient conditions and it is by far the most abundant substance on Earth [2]. The phase diagram for the stable phases of water is shown in Fig. 2.2.

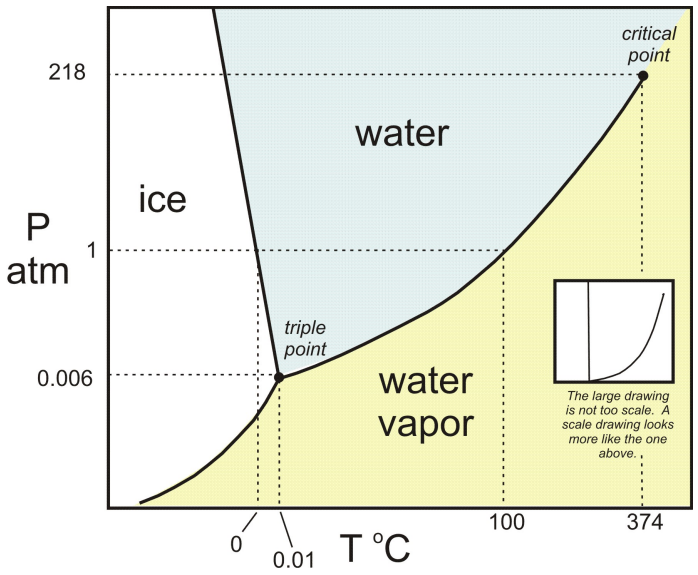

Figure 2.2: Phase diagram of the stable phases of water in the $P - T$ plane.

One peculiar feature of the phase diagram of water is the negative slope of the coexistence line between the liquid and the solid phases. The Clausius-Clapeyron relation

$$\frac{dP}{dT} = \frac{1}{T}\frac{\lambda}{\Delta V} \tag{2.1}$$

where λ is the latent heat of fusion, thus implies that when water freezes, its volume increases, as opposed to most substances for which the solid phase is denser. This characteristic of water is related to the so called *density anomaly*, which will be discussed together with the other anomalies of liquid water in Sec. 2.3.

The hexagonal ice I_h is not the only solid phase of water. Sixteen crystalline phases of water have been identified up to today. Twelve of them, ices II, III, V, VI, VII, VIII, X, XI, XIII, XIV, XV and ordinary hexagonal ice I_h, are stable in well defined intervals of temperatures and pressures. The remaining four, ices IV, IX, XII and cubic ice I_c are metastable [5, 66, 67]. The presence of different forms of ice is known as *polymorphism* of water. In the following we will discuss the metastable states of water, with particular regard to *supercooled water*, liquid water below the freezing point.

2.2.1 Thermodynamic and mechanical stability

Thermodynamics is by definition the study of equilibrium states that possess an indefinite lifetime. However, there exist (meta-)equilibrium states with a finite lifetime, for which the system is trapped in a relative minimum of the appropriate thermodynamic potential. These states are defined *metastable states*. Small thermal fluctuations, the presence of impurities or even roughness of the container (for liquids and gases) are in general sufficient to induce the transition from metastable states to the energetically favored corresponding equilibrium states. In order to be able to investigate a metastable state, its lifetime must be longer than the observation time. In turn this needs to be much longer than the structural relaxation time (towards equilibrium) so that

$$\tau_{\text{rel}} << \tau_{\text{obs}} < \tau_{\text{life}} \quad . \tag{2.2}$$

We do not discuss here the details of the theory of metastability [6] but we recall some concepts useful for our studies.

Starting from the second principle of thermodynamics, the conditions of thermal and mechanical equilibrium can be derived [6]. In order to have mechanical stability the isothermal compressibility $K_T = -(\partial V/\partial P)_T/V$ and the adiabatic compressibility $K_S = -(\partial V/\partial P)_S/V$ must be positive. In order to have thermal equilibrium the isobaric specific heat $C_P = T(\partial S/\partial T)_P/N$

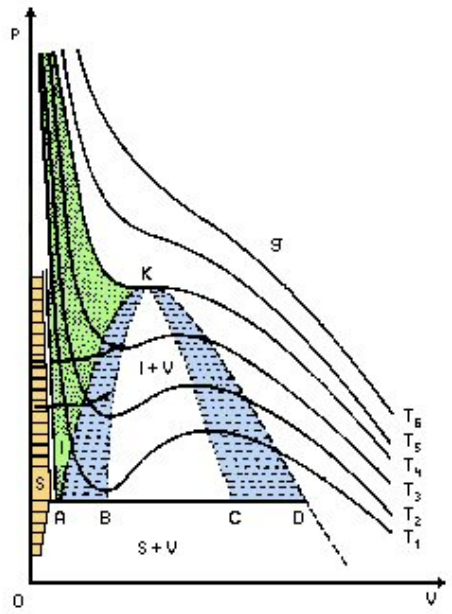

Figure 2.3: Isotherms of a generic system near a phase transition in the van der Waals theory. The Maxwell construction is used to draw the coexistence line AKD. The limit of mechanical stability (LMS) line BKC is also shown.

and the isochoric specific heat $C_V = T(\partial S/\partial T)_V/N$ must be also positive. Let us consider the van der Waals theory of a phase transition. In Fig. 2.3 generic isotherms in the $P - V$ plane are reported. The Maxwell construction is used to draw the coexistence line AKD. However doing so, all the points between the left intersection of the isotherms with the coexistence line and the minimum and the ones between the maximum and the right intersection of the isotherms with the coexistence line are excluded. These points are not thermally stable but are still mechanically stable. In fact for these points K_T and K_S are larger than zero. The compressibility diverges at the extrema of the isotherms and it is negative in the region between the minimum and the maximum. If we now join the minima of the isotherms on the left side and the maxima on the right side we can draw the limit of mechanical stability (LMS) line BKC. Thus the region of metastability can be defined as the region enclosed between the coexistence line and the LMS line. The only point in common between the coexistence line and the LMS line is the critical point K, that is also the only stable point belonging to the LMS line.

In the metastability region, nucleation phenomena of the stable phase

can occur and special techniques must be used in experiments in order to avoid the transition to the stable phase.

2.2.2 Metastable states of liquid and solid water

Under special conditions, such as the extreme purity of the sample, the absence of external mechanical and thermal perturbations, the high degree of smoothness of the walls of the container, the range of existence of liquid water can be significantly extended. At ambient pressure the range of existence of the liquid phase of water goes from $T = 273$ K to $T = 373$ K and under the mentioned conditions it can be extended to the range from $T = 235$ K to $T = 553$ K. Liquid water above the boiling point is defined *superheated water* and liquid water below the freezing point is defined *supercooled water*. A diagram of the range of existence at ambient pressure of these phases is reported in Fig. 2.4.

Metastable liquid phases of water are important in biological, geophysical and industrial processes [6]. In our studies we focus on the supercooled region. From an experimental point of view, it is possible to delay the onset of crystallization decreasing the concentration of impurities, because they are possible centres of nucleation of the solid phase. This can be achieved dividing the sample in small droplets, with dimensions 1-10 μm. On average they will contain less than one impurity each. The limit of this technique is reached when the intrinsic rate of crystallization becomes so fast that the lifetime of the droplets falls below the observation time [68]. For example, the lifetime of a 5 μm droplet is of the order of 10^{-5} s when the rate of crystallization reaches 10^{15} cm^{-3} s^{-1}. This condition defines an experimental limit, which depends on the pressure, known as *homogeneous nucleation temperature*. This temperatures is $T = 235$ K at ambient pressure [68]. It must be noted that the homogeneous nucleation temperature is a kinetic limit and not a thermodynamic one. As thus it can be considered as a practical limit, function of the cooling rate and of the observation time [5].

If the cooling rate is fast enough, the homogeneous nucleation can be bypassed and water can be brought to the *glass transition*. The phase resulting from this kinetic transition is a solid phase that lacks long range order, an amorphous phase or a glass. The glass transition temperature is defined as the temperature at which the viscosity of the system becomes $\eta = 10^{13}$ poise ($= 10^{12}$ Pa·s). The temperature at which the glass transition occurs in water is an open question, although a generally accepted value is $T_g = 136$ K at ambient pressure [5,69]. The glass transition is not a thermodynamic transition but a kinetic one. This implies that different cooling procedures can produce slightly different glass transition temperatures. Above the glass transition

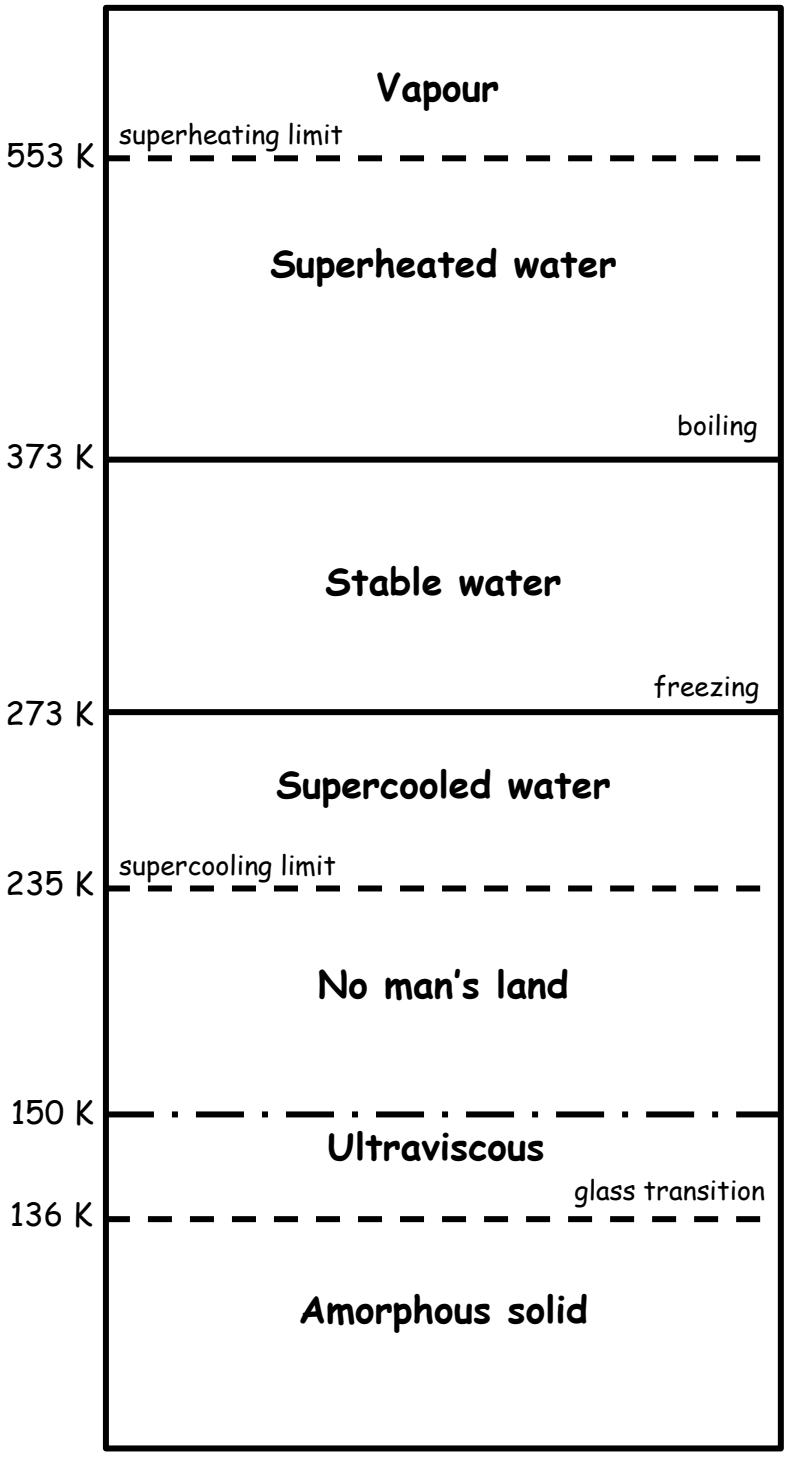

Figure 2.4: Diagram of stable and metastable phases of non-crystalline water at ambient pressure. Thermodynamic boundaries are represented by solid lines, while kinetic boundaries are represented by dashed lines.

temperature, up to $T = 150$ K, the temperature of spontaneous crystallization to ice I_c, water can exist in an extremely viscous liquid state [5]. Water in this small region is defined *ultraviscous*.

The interval between the homogeneous nucleation temperature and $T = 150$ K is often denoted as *no man's land* [11]. In this region liquid water cannot be observed with available experimental techniques because of the tremendous increase of the crystallization rate and the consequent decrease of the lifetime of the liquid state. However the existence of metastable liquid water below the homogeneous nucleation temperature is not in principle forbidden by thermodynamic constraints [5].

Besides having sixteen forms of the crystalline phase, water also has three amorphous phases. This property is know as *polyamorphism* of water. The *high density amorphous* (HDA) and the *low density amorphous* (LDA) are the most known forms of glassy water. Recently also the *very high density amorphous* (VHDA) has been identified [70]. In particular it has been shown that the amorphous states formed starting from the liquid or the vapour, through the hyperquenching of small droplets or the deposition of the vapour on a metal plate at very low temperatures, correspond to the LDA. While the amorphous states formed starting from the solid, through compression, correspond to the HDA [5, 6, 71–73]. Furthermore it has been shown that a first-order-like transition exists between LDA and HDA with a discontinuous jump in the density when the coexistence line is crossed [74]. The existence of two distinct liquid phases in the no man's land, the *low density liquid* (LDL) and the *high density liquid* (HDL), corresponding respectively to their amorphous counterparts LDA and HDA has been hypothesized. We will come back to this matter in Sec. 2.4 where the liquid-liquid critical point (LLCP) hypothesis will be discussed.

2.3 The anomalies of liquid water

Although water is the most common liquid on Earth, it cannot be defined as an ordinary liquid. In fact water behaves in most respects differently from what one would expect for a simple liquid [75]. Up to today 67 anomalies of water have been discovered [4–6, 76]. The molecular structure of the water molecule is apparently very simple but the intra-molecular hydrogen bonding structure determines an highly complex and anomalous behaviour. In the following we will review some of the anomalous properties of water with particular regard to the ones relevant for the discussion of the results presented in Chap. 4, 5 and 6.

Probably the most known anomaly of water is the *density anomaly*. As

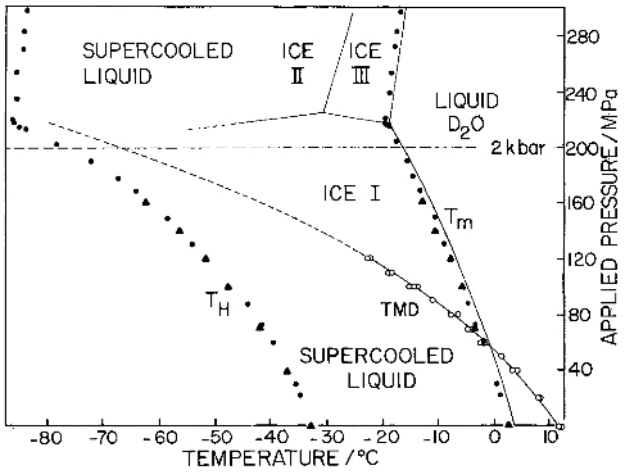

Figure 2.5: TMD line for D_2O in the $P - T$ plane. Circles are from experiments and the line is an extrapolation from Ref. [78]. T_M represents the melting line and T_H the locus of homogeneous nucleation (see Sec. 2.2.2). Figure from Ref. [77].

we anticipated in Sec. 2.2, the density anomaly is connected with the fact that the slope of the liquid-solid coexistence line is negative for water, which is the opposite of what happens in most substances. At ambient pressure, the density of water does not decrease monotonically with increasing temperature, as one would expect, but it shows a maximum at $T = 277$ K. When pressure is varied, the temperature at which the density maximum occurs changes. Thus a line of density maxima can be drawn in the phase diagram: this line is called the temperature of maximum density (TMD) line. In Fig. 2.5 the experimental TMD line is shown for D_2O [77], together with the melting line and the locus of homogeneous nucleation.

Beyond the density maximum, the existence of a density minimum in deep supercooled confined water has been observed experimentally [79, 80]. At temperatures lower than the density minimum temperature, the normal behaviour of the density as a function of temperature is restored. The confinement in small silica pores allowed in this case to avoid the crystallization. These results indicate that also in bulk water a density minimum could be found, as it is also seen in computer simulation studies [22].

Let us now consider the thermodynamic response functions, the isothermal compressibility K_T, the isobaric specific heat C_P and the coefficient of thermal expansion α_P . They are defined by the relations:

$$K_T = -\frac{1}{V}\left(\frac{\partial V}{\partial P}\right)_T \tag{2.3}$$

$$C_P = \frac{T}{N}\left(\frac{\partial S}{\partial T}\right)_P \tag{2.4}$$

$$\alpha_P = \frac{1}{V}\left(\frac{\partial V}{\partial T}\right)_P \tag{2.5}$$

and they are connected to the fluctuations of volume and entropy by the equations:

$$\langle(\delta V)^2\rangle = V k_B T K_T \tag{2.6}$$

$$\langle(\delta S)^2\rangle = N k_B C_P \tag{2.7}$$

$$\langle \delta V \cdot \delta S\rangle = V k_B T \alpha_P \quad . \tag{2.8}$$

These relations link the macroscopic thermodynamic response function with the microscopic behaviour described by statistical mechanics. Thus the isothermal compressibility is a measure of the volume fluctuations, being V in Eq. 2.6 the mean value of the fluctuating volume for a fixed number of particles. The isobaric specific heat is proportional to the entropy fluctuations of N molecules at fixed pressures. It is also connected to the isochoric specific heat, through the relation $C_P - C_V = TV(\alpha_P^2/K_T)/N$. The coefficient of thermal expansion measures the cross-correlations of entropy and volume. Furthermore the TMD line is the thermodynamic locus along which the coefficient of thermal expansion is zero. In fact $\alpha_P = (\partial V/\partial T)_P/V = -(\partial\rho/\partial T)_P/\rho$.

In Fig. 2.6 the experimental behaviour of the isothermal compressibility K_T at several pressures is shown. At ambient pressure the isothermal compressibility decreases at high temperatures, reaches a minimum around $T = 319$ K and then it increases rapidly, especially in the supercooled region. The minimum of K_T moves at lower temperatures, when pressure is increased. In a simple liquid the isothermal compressibility decreases monotonically with decreasing temperature.

In Fig. 2.7 we report the experimental isobaric specific heat C_P. Its trend with temperature is analogous to that of the isothermal compressibility. At ambient temperature C_P has a minimum at $T = 308$ K then it increases steadily. The isobaric specific heat monotonically decreases with decreasing temperature in a simple liquid.

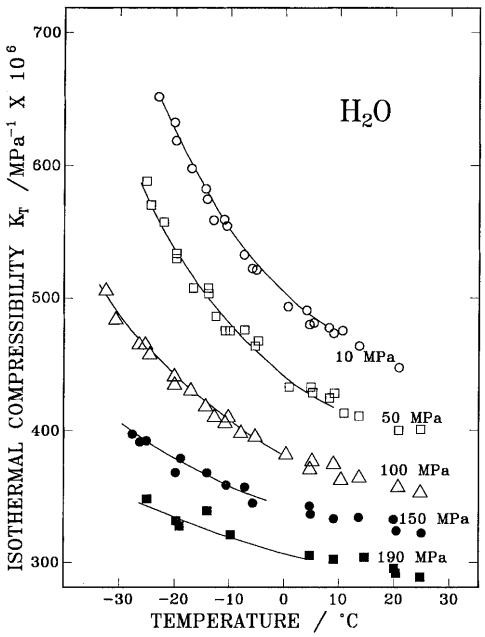

Figure 2.6: Experimental isothermal compressibility K_T for several pressures. Curves are fit of experimental data with power law relations. Data from Ref. [81] and figure from Ref. [6].

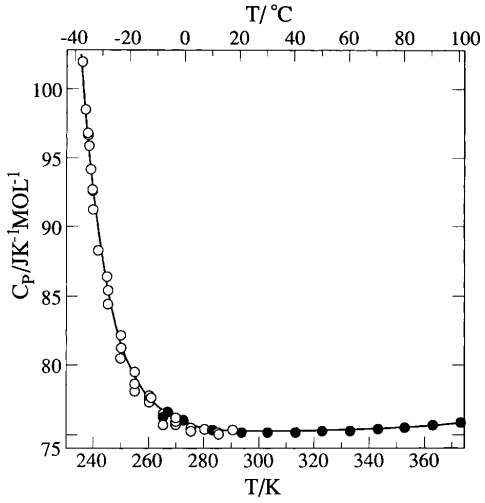

Figure 2.7: Experimental isobaric specific heat C_P at ambient pressure. Data from Ref. [82] and figure from Ref. [6].

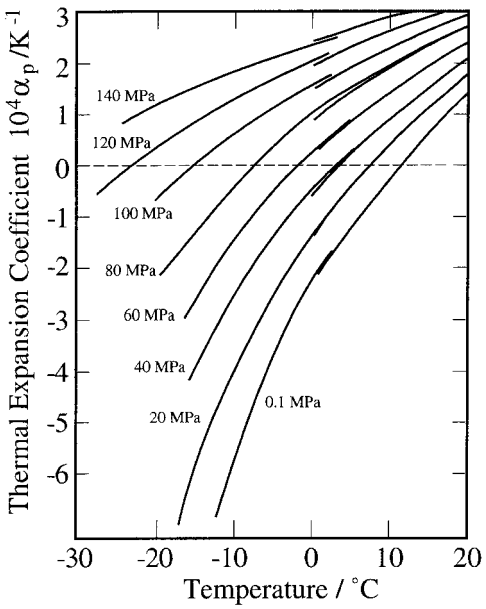

Figure 2.8: Experimental coefficient of thermal expansion α_P at several pressures for D_2O. Data from Ref. [83] and figure from Ref. [6].

The experimental trend of the coefficient of thermal expansion α_P at several pressures is shown in Fig. 2.8. At ambient pressures $\alpha_P = 0$ at $T = 277$ K, the temperature of maximum density (TMD), then upon decreasing temperature it becomes negative and rapidly decreases. At higher pressures the temperature for which $\alpha_P = 0$ decreases, as we have seen also looking at the TMD in Fig. 2.5. In a simple liquid α_P is expected to decrease monotonically with decreasing temperature, remaining greater than zero.

The trends of the density ρ and of the thermodynamic response functions K_T, C_P and α_P as functions of the temperature, at ambient pressure, are reported together with the expected trends for a simple liquid in Fig. 2.9. In simple liquids the volume and entropy fluctuations become smaller decreasing the temperature. In water the volume and entropy fluctuations becomes instead larger at low temperatures, as signaled by the increase of the isothermal compressibility and the isobaric specific heat respectively. Moreover another anomalous behaviour is indicated by the change of sign of the coefficient of thermal expansion below $T = 277$ K (at ambient pressure). In fact this means that volume and entropy fluctuations at low temperatures are anti-correlated, that is to say an increase in volume implies a decrease in entropy. This anti-correlation is caused by the formation of the open network of hydrogen bonds for which a decrease in orientational entropy is

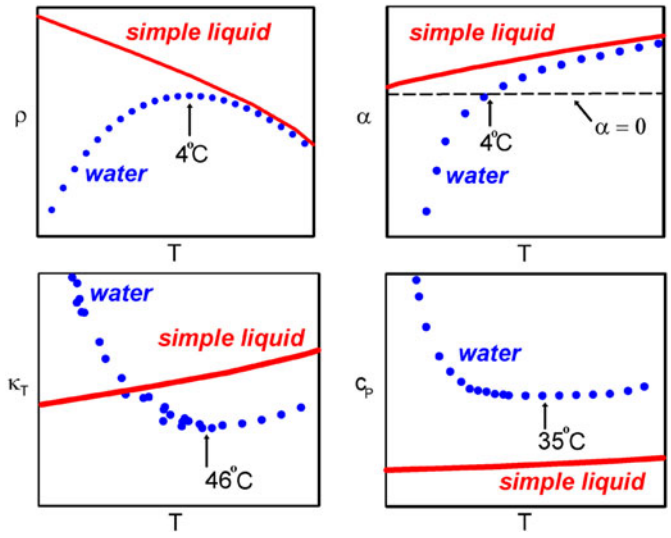

Figure 2.9: Trends of the density ρ (top left panel), the coefficient of thermal expansion α_P (top right panel), the isothermal compressibility K_T (bottom left panel) and the isobaric specific heat (bottom right panel) as functions of temperature for water and for a simple liquid. Figure from Ref. [5].

accompanied by an increase in volume.

We can also note that all the response functions show an (at least) apparent divergent behaviour in the supercooled region. Sometimes their trend is generalized by a power law expression of the kind

$$X = A \left(\frac{T - T_S}{T_S} \right)^{\lambda_X} \tag{2.9}$$

where X is the generic response function, A is an amplitude, λ_X is the exponent associated to the divergence of the quantity X and T_S is the temperature at which the divergence occurs. Speedy and Angell [84] proposed a singular temperature at $T = 228$ K. The origin of these apparent divergences in the behaviour of the response functions is still debated. Several theories have been proposed to explain this phenomenon and the other anomalies of water. We will enter more into details in Sec. 2.4.

The anomalies of water are not only thermodynamic. Also its dynamic behaviour is anomalous. Let us now consider the self-diffusion coefficient (or diffusivity) D. It is connected to the mean square displacement (MSD) of a particle by the relation

$$D = \lim_{t \to \infty} \frac{\langle |\mathbf{r}_j(t' + t) - \mathbf{r}_j(t')|^2 \rangle_{t'}}{6t} \tag{2.10}$$

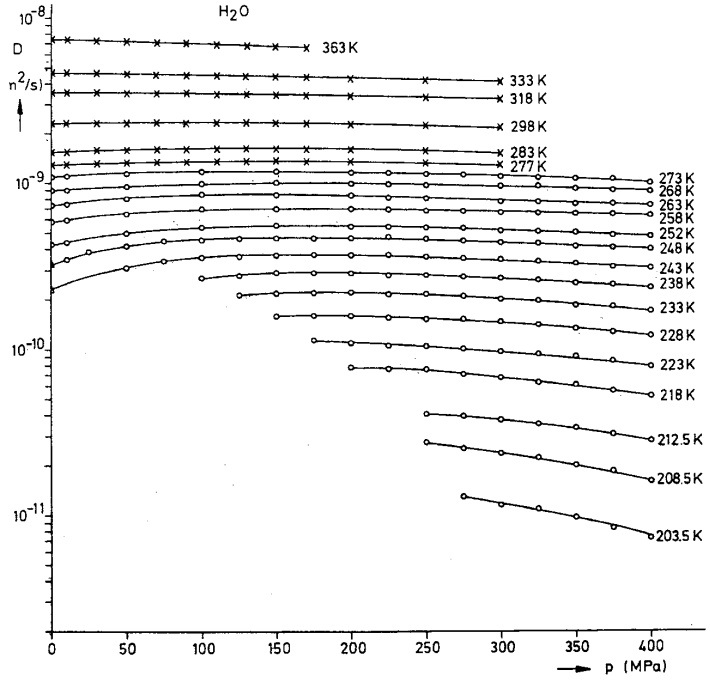

Figure 2.10: Experimental self-diffusion coefficient D of water, at constant temperature, as a function of the pressure. Figure from Ref. [5].

and to the viscosity, through the Stokes-Einstein relation

$$D = \mu k_B T \tag{2.11}$$

where μ is a generic mobility coefficient. For spherical particles in a liquid $\mu = 1/(6\pi\eta r)$, where η is the viscosity and r is the radius of the particles.

In simple liquids the diffusion coefficient is expected to decrease upon compression. On the contrary for water below circa $T = 283$ K the diffusivity increases upon increasing the pressure (or analogously the density) until a maximum is reached ($P \simeq 150$ MPa at $T = 283$ K). This behaviour is known as *diffusivity anomaly*. In Fig. 2.10 the experimental behaviour of the diffusion coefficient for a wide range of temperature and pressures is reported. In computer simulations it has been shown that upon further decreasing the density, the normal behaviour is restored, passing through a minimum in the diffusion coefficient. The maxima and the minima of the diffusivity at constant temperature can be joined to draw a line of diffusivity extrema [12, 85, 86].

Glass forming liquids, such as water, are usually classified in two categories, according to their dynamic behaviour. The liquids for which the

diffusion coefficient is an exponential function of $1/T$

$$D = D_0 \exp\left(-\frac{E_A}{k_B T}\right) \tag{2.12}$$

where E_A is the activation energy, are said to have Arrhenius (or activated) behaviour. The liquids that show a different functional relationship between the diffusion coefficient and $1/T$ are said to have non-Arrhenius behaviour. Following Angell's classification of glass forming liquids, elaborated originally using the viscosity, liquids for which the viscosity is an exponential function of $1/T$ are said *strong* liquids and those that have a different functional relationship are said $fragile$ [9, 87]. The functional form for non-Arrhenius behaviour is often fitted using the empirical Vogel-Fulcher-Tamman (VFT) law

$$D = D_0 \exp\left(-\frac{B}{T - T_0}\right) \tag{2.13}$$

where B and T_0 are the fitting parameters. In alternative the non-Arrhenius behaviour is treated by the more refined *mode coupling theory* (MCT) [88, 89]. This theory describes the particles in a dense liquid as temporary blocked in a *cage* of their neighbours. The MCT predicts the existence of a critical temperature T_C at which the diffusion coefficient, or equivalently the inverse of the relaxation time of the correlation functions, goes to zero with a power law

$$D \propto \tau^{-1} \propto (T - T_C)^{\gamma} \tag{2.14}$$

with γ larger than 1.5. The validity of the MCT theory has been confirmed for several systems [87] and in particular for confined water [90, 91].

Water shows a crossover from a non-Arrhenius behaviour at high temperature to an Arrhenius behaviour at low temperature, also known as *fragile to strong crossover* (FSC) [9]. This crossover has been widely investigated in experiments on confined water [92–96] and in computer simulations both on bulk and confined water [13, 97, 98].

In Fig. 2.11 is shown the logarithm of the relaxation time (proportional to the inverse of the diffusion coefficient) as a function of $1/T$ measured for water confined in MCM-41 silica pores [92]. The crossover from non-Arrhenius behaviour at high temperature, fitted here using the VFT law, to Arrhenius behaviour at low temperature is clearly visible. The experimental investigation of the FSC is hampered in bulk water by the homogeneous nucleation. Computer simulations indicate that it can be found also in bulk water [99]. Recent experimental results suggest also that in low temperature water the Stokes-Einstein relation is violated and consequently the diffusion

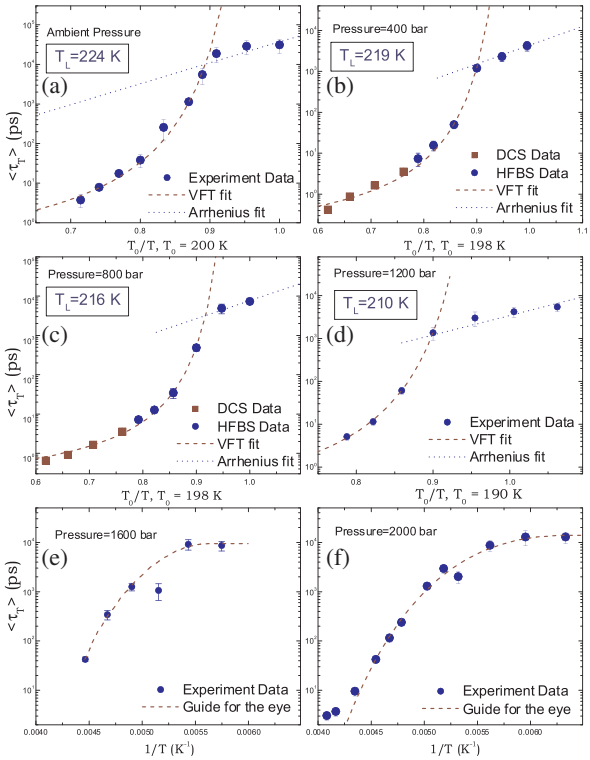

Figure 2.11: Average translational relaxation time τ_T as a function of $1/T$ for water confined in silica MCM-41 pores at several pressures. Data and figure from Ref. [92].

coefficient and the viscosity become decoupled, with $D\tau$ and $D\eta/T$ not temperature independent anymore. [100, 101].

Thermodynamic and dynamic anomalies of water have often been qualitatively described as consequences of the structure of water and its hydrogen bond network. It has been in shown in theory [85] and in computer simulations [85, 102] that the regions of thermodynamic and dynamic anomalies are both encompassed by a wider region of structural anomalies. This region was defined considering a local orientational order parameter q, measuring the degree of tetrahedrality of the arrangement of water molecules in the first shell and a translational order parameter t, which measures the tendency of two water molecules to sit at a preferential separation. These order parameters possess a region of anomalous behavior, where they both decrease upon compression [102]. The line of structural anomalies is then built considering the loci of maximum orientational order, at low densities, and minimum translational order, at high densities. Inside this region of structural anomalies water becomes more disordered upon compression. Therefore it has been

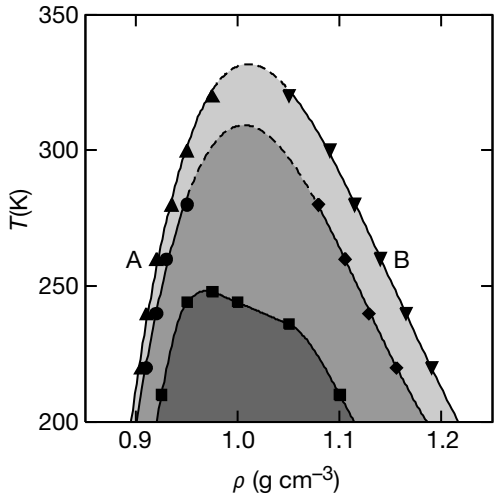

Figure 2.12: Loci of structural, dynamic and thermodynamic anomalies for SPC/E water. The region of structural anomaly is bound by the loci of q maxima (triangles up) and t minima (triangles down). Within this region the degree of order of water decreases upon compression. The diffusivity anomaly region is bound by diffusion coefficient minima (circles) and maxima (diamonds). Inside this region the diffusion coefficient increases upon increasing density. The region of density anomaly is bound by the TMD points (squares). Within this region the density of water increases upon isobaric heating. Data and figure from Ref. [85].

demonstrated that structural, dynamic and thermodynamic anomalies of water occur in a cascade as the degree of order is increased. In Fig. 2.12 the cascade of water anomalies is depicted.

2.4 Scenarios for supercooled water

Several scenarios have been elaborated in the last thirty years to explain the numerous anomalies of water. We shall first describe the scenario in which we will work when we present our results, the *liquid-liquid critical point* (LLCP) scenario.

2.4.1 The LLCP scenario

The LLCP scenario has its origin in the 1992 Poole *et al.* paper [7]. On the basis of computer simulations on ST2 water, Stanley's group at Boston University hypothesized the existence of two distinct phases of water in the deep supercooled region (the no man's land), the low density liquid

(LDL) and the high density liquid (HDL), corresponding respectively to the experimentally observed amorphous phases LDA and HDA (see Sec. 2.2.2). The two phases of supercooled water, in analogy with what happens with their corresponding amorphous phases, would be separated by a first order phase transition line. This line would end in a LLCP, above which the distinction between the two phases disappears. From the LLCP a line of maxima of the thermodynamic response functions is emanated, the so called *Widom line*. This line can be thought as an extension of the coexistence line in the one phase region [13, 14] and it can be observed also for the ordinary liquid-vapour critical point [103].

In Fig. 2.13 the main features of the LLCP scenario are shown in $T - P$ plane. In the LLCP scenario the apparent divergences of the thermodynamic response functions we have seen in Sec. 2.3, are due to the progressive increase of the correlation length upon approaching the critical point. Eventually the correlation length and the trends of thermodynamic response functions are supposed to diverge at the critical point. Even the anomalous behaviour of water at ambient temperature could be framed in this scenario as a consequence of the long range fluctuations induced by the presence of a critical point.

The Poole *et al.* [7] paper inspired a vast amount of experimental [11, 31, 42, 79, 92, 96, 104, 105], theoretical and computer simulation [3, 12–30] works.

The experimental investigation of the LLCP in bulk water is hampered by the fact that the homogeneous nucleation intervenes before being able to reach the temperature of the putative critical point. However experiments sustained the hypothesis that the amorphous phases of water can be connected to the normal liquid through a reversible thermodynamic path [106]. Mishima and Stanley [11, 31] studying the decompression-induced melting lines of different high-pressure phases of ice in small emulsified droplets, found that the ice IV melting line shows a discontinuity at the location proposed for the liquid-liquid transition. From the study of the Gibbs potential surface and the corresponding equation of state, they predicted the occurrence of a LLCP at $T \simeq 220$ K and $P \simeq 100$ MPa. Recently an electron spin resonance experiment [105] found for bulk water results consistent with the coexistence of LDL and HDL phases in the deep supercooled region. One method used to avoid crystallization of water is to confine it in small pores. Chen's group at MIT is one of the most active in this field of research. They performed several neutron scattering experiments on water confined in silica MCM-41 pores [42, 79, 92, 96] and found results consistent with the LLCP scenario. Very recently Zhang *et al.* [42] observed for the first time in confined D_2O the appearance of hysteresis in density, confirming the presence of a first order phase transition line. They also located the

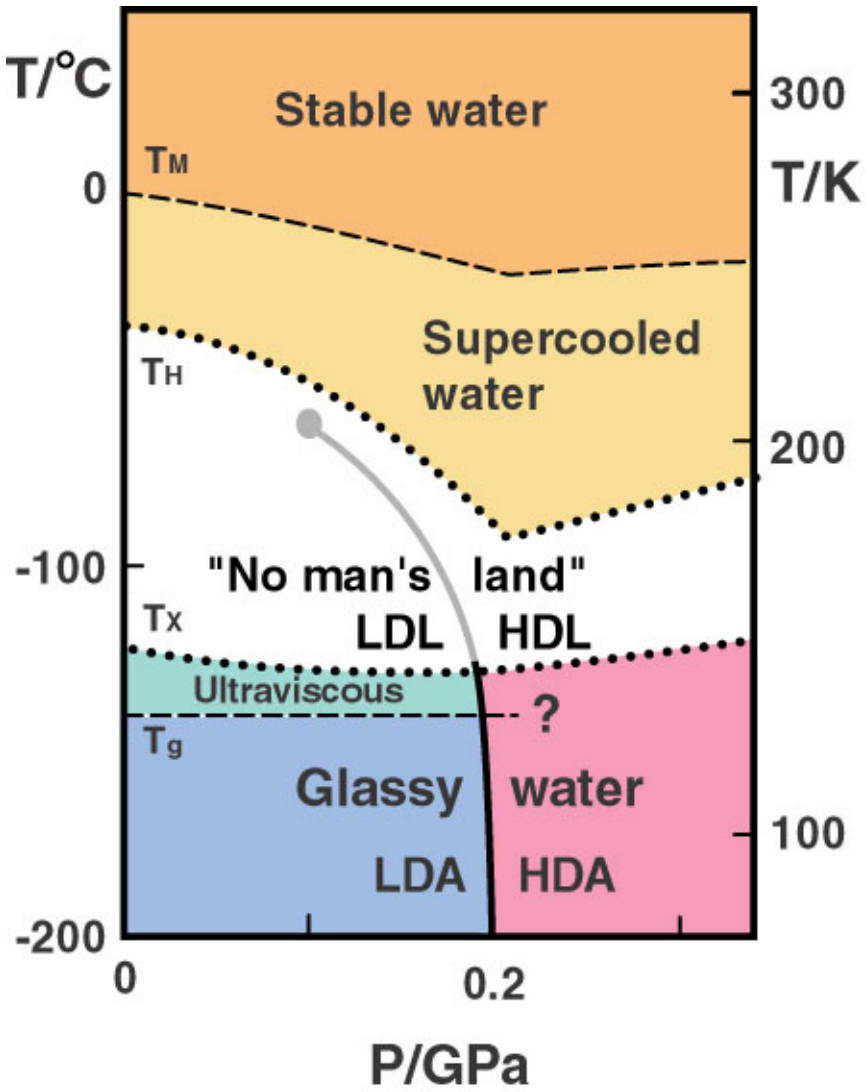

Figure 2.13: Main features of the LLCP scenario. The LDA and HDA are separated by a first order phase transition line. This line extends above the glass transition line in the so called no man's land and separates the two distinct liquid phases LDL and HDL. At the end of the coexistence line is situated the LLCP, above which the distinction between the two liquids disappears. T_H is the line of the homogeneous nucleation and T_M is the melting line. Figure from Ref. [3] by courtesy of O. Mishima.

critical point for confined D_2O at $T = 210 \pm 10$ K and $P = 150 \pm 50$ MPa. The structural properties of the hypothesized LDL and HDL phases were also investigated studying the water radial distribution functions (RDFs) by neutron diffraction scattering experiments. Soper and Ricci [104] found that the second shell of the oxygen-oxygen RDF collapses in HDL with respect to LDL, with a substantive breaking of the hydrogen bonds between the first and the second shell of water. Moreover in HDL, the hydrogen bonds within the first shell become more linear. In Fig. 2.14 the oxygen-oxygen, oxygen-hydrogen and hydrogen-hydrogen RDFs from Ref. [104] are shown.

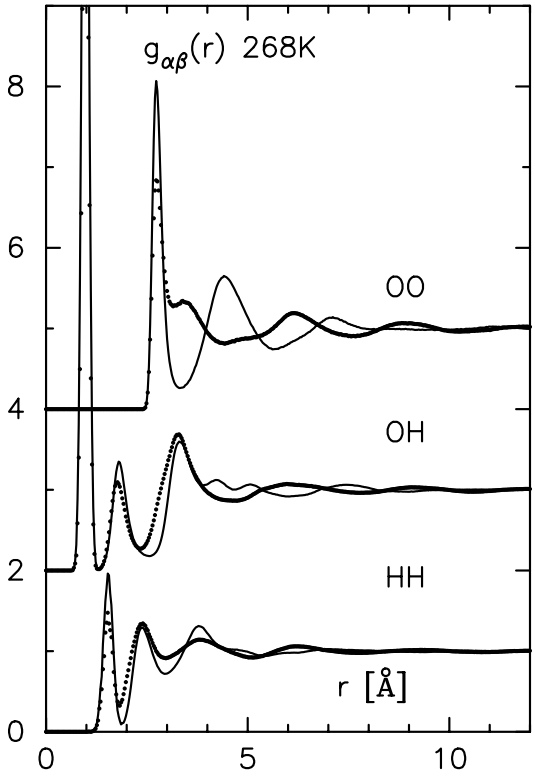

Figure 2.14: Oxygen-oxygen, oxygen-hydrogen and hydrogen-hydrogen RDF at $T = 268$ K, for LDL and HDL as calculated starting from neutron diffraction experimental data. Data and figure from Ref. [104].

Computer simulations play a very important role in the study of the LLCP scenario and of supercooled water in general. In fact the crystallization can be avoided in simulations and thus the study of the no man's land is possible. As we mentioned several times already the LLCP scenario was born from results on the ST2 model of water [7]. Since then, data consistent

with the existence of LDL and HDL phases and the occurrence of the LLCP have been found using the ST2 [18,20,24,25], SPC/E [29], TIP4P [18,24,28], TIP5P [13, 21, 26], TIP5P-E [22], TIP4P-Ew [23] and BSV [27] models for water. The location of the LLCP for TIP4P water proposed by Tanaka [28] was contested by Sciortino *et al.* [24] who determined bounds for the LLCP of TIP4P water, $T < 200$ K and $P > 70$ MPa. Brovchenko *et al.* [107] proposed the occurrence of multiple liquid-liquid transitions and critical points by data from simulations performed with the ST2, SPC/E, TIP4P and TIP5P models. These results have however been cast into doubt by Liu *et al.* [25] who underlined how the inadequate treatment of long range electrostatics or the not fully justified suppression of fluctuations in the restricted ensemble calculations performed in Brovchenko *et al.*'s paper, may have led to the presence of artifacts in the simulation results.

Simplified models have been also important in studying the plausibility of the LLCP scenario. Truskett *et al.* [30] showed the possible emergence of the LLCP scenario in an analytical model for water. Mean field calculations and Monte Carlo simulations have been performed using a two-dimensional cell (lattice) model [14–16, 99]. In particular it was shown that varying the parameters of this model, one is able to recover all the scenarios proposed for supercooled water. The validity of the LLCP hypothesis for real water was predicted on the basis of the mapping of available experimental data for water onto the parameters of the cell model [16]. Three-dimensional spherically symmetric models, such as the Jagla ramp potential (JRP) [55, 56] have been also used to study water anomalies and their possible link to the LLCP [12, 13, 17, 35, 57–59, 102, 108, 109]. This model is characterized by the presence of two length scales, a hard core corresponding to water first coordination shell and a soft core corresponding to water second coordination shell. With the appropriate choice of parameters, the Jagla ramp potential (supplemented by an attractive tail) displays thermodynamic, dynamic and and structural anomalies of water [12]. Also the LDL-HDL coexistence and the LLCP are found in this model [12, 17, 57]. These results demonstrated that tetrahedrality or even orientation dependent interactions are not necessary conditions for the appearance of water anomalies and liquid-liquid transition. Therefore the anomalous phenomenology of water seems to be generated only by the presence of two distinct length scales in the interaction potential [12, 13, 17, 58, 59, 108–113]. Spherically symmetric potential with softened core have been used also as coarse-grained models for a number of substances beyond water, such as metallic and colloidal systems [114–118].

Experimental and computer simulation evidence of the existence of a liquid-liquid phase transition at high temperatures and pressures has been found also for silicon [119], germanium [120], silica SiO_2 [121] and BeF_2 [122].

Indirect experimental evidence has been also found for sulphur [123] and selenium [124].

The dynamic anomalies and in particular the FSC can be also framed in the LLCP scenario. Experiments [92–96, 125] and computer simulations [12, 13, 15, 57, 98] have pointed out how the FSC appears to occur when crossing the Widom line, above the LLCP. The dynamic crossover can be related to the maxima of the specific heat occurring at the Widom line through the Adam-Gibbs theory. More details will be given when discussing the results on the dynamics of the HS-JRP set (see Sec. 6.4). In water, it has been observed that the behaviour of the diffusion coefficient changes from non-Arrhenius (fragile) to Arrhenius (strong) where the structural and thermodynamic properties change from HDL to LDL, suggesting a strong relationship between the thermodynamic and the dynamic transitions.

2.4.2 Other scenarios for supercooled water

In this section we briefly review the other scenarios that have been proposed to explain the appearance of the anomalies in supercooled water.

The first unifying scenario was proposed by Speedy [10] in 1982 and it is known as *stability limit conjecture*. In this scenario the increase in the thermodynamic response functions was attributed to the approach to the LMS line, where the supercooled liquid becomes unstable with respect to the vapour phase. This scenario predicted also the existence of a continuous LMS line bounding the superheated and the supercooled states, reverting to positive pressures for low temperatures. This behaviour of the LMS line would be anomalous, as in simple liquids the LMS line has a positive slope in all the phase diagram [5]. Subtle arguments of thermodynamic consistency basically ruled out this scenario [5]. Furthermore no evidence of a retracing LMS line was found either in experiments or in computer simulations.

The *singularity-free scenario* was first presented by Sastry *et al.* [8] in 1996. In this scenario the increase in the thermodynamic response functions is seen as a consequence of the presence of the density anomaly. K_T, C_P and α_P (absolute value) increase due to the anti-correlation of volume and entropy at low temperatures but they do not eventually diverge. Their values remain instead finite, and no underlying singularity is predicted [126]. Maxima in K_T, C_P and α_P are thus predicted both in the LLCP scenario (above the critical point in this case) and in the singularity-free one. In the LLCP case the maxima of the three response functions are expected to grow upon increasing pressure; in the singularity-free case only K_T and α_P maxima grow while C_P maxima do not change in height. Until recently this was the only difference between the two scenarios above the homogeneous

nucleation temperature. Using the two-dimensional cell model mentioned above, it was shown that the effect of pressure on the dynamics is strikingly different in the two scenarios [15], thus proposing a new criterion to distinguish between them.

In 2008 Angell proposed a new scenario, the *critical point-free scenario* [9]. In this case the liquid-liquid transition is hypothesized to be an order-disorder transition, possibly having a weak first order character. This transition should extend to the region of negative pressures, down to the LMS line. Upon meeting the LMS line the coexistence line terminates and no critical point occurs.

Very recently Zhang *et al.* [42] although supporting the LLCP scenario, argued that the LLCP might have a different nature and phenomenology from the liquid-vapour critical point. In particular they proposed that the LLCP might be a *tricritical* point, joining a line of first order phase transition with a line of second order phase transition. The existence of the second order phase transition was suggested by the appearance of *kinks* in the behavior of the coefficient of thermal expansion for water confined in silica pores.

2.5 Anomalies in aqueous solutions

Besides being a very special liquid, water is also known to be quite an extraordinary solvent [69]. It is generally well known that the presence of solutes in water affect thermodynamic quantities, such as the melting point, the boiling point and viscosity. But the effect of the presence of solutes is not limited to those quantities and the modifications induced by the solutes on the behaviour of water could help in shedding light on the numerous open questions regarding bulk liquid water [127]. In particular the effect of the presence of solutes on the critical behaviour has been widely studied with regard to the liquid-vapour critical point [37–40], while the study of the effect of solutes on the LLCP phenomenon is a relatively new subject [128, 129]. Because of the fundamental functions aqueous solutions play in living systems, the study of the liquid-liquid critical behaviour in aqueous solutions can also be important in biology. In this section we will review some features of the aqueous solutions with polar (hydrophilic) or apolar (hydrophobic) solutes. A complete description of the phenomena related to the presence of solutes in water is beyond the aim of this section and we will limit ourselves to the presentation of the properties relevant for the discussion of the results in the following chapters.

2.5.1 Polar solutes

The prototype of polar solutes is represented by ionic compounds dissolved in water. In particular it is well known that alkali-halides have very high solubility in water. The majority of works in literature concentrated on the properties of ionic aqueous solutions at ambient temperature or on the study of the glass transition (see Ref. [69] and references therein). The thermodynamics of ionic aqueous solutions in the mild supercooled regime, where water anomalies increase, still lacks a thorough investigation. The properties of solutions of ionic compounds in water at low temperatures are relevant in different fields, including cryopreseration of living cells [32], cloud formation [33] and food preservation [130].

The anomalous properties of water have been experimentally analysed in the supercooled NaCl(aq) and $NaNO_3$(aq) [131, 132] with differential scanning calorimetry. It was found the anomalous behaviour of thermodynamic response functions and the appearance of a TMD are preserved in the solutions up to concentrations from low to moderate. The anomalous behaviour progressively weakens upon increasing the concentration of salts [131, 132]. In particular for NaCl(aq) we show in Fig. 2.15 the experimental isobaric specific heat, at ambient pressure, of water and NaCl(aq) at several concentrations. For low concentrations the behaviour of the specific heat remains similar to that of bulk water. Upon increasing concentration differences start to appear but the anomaly, with the presence of a minimum in the trend of C_P as a function of the temperature and a successive increase for lower temperatures is found up to circa $c = 2.00$ mol/kg, even if it progressively weakens as the concentration increases. For higher still concentrations, the anomalous behaviour disappears and the trend expected for simple liquids is recovered. Also the presence of a TMD point at ambient pressure was investigated at it was found that the TMD is still present up to $c = 1.487$ mol/kg and it disappears at a concentration in the range from $c = 1.487$ mol/kg to $c = 2.330$ mol/kg [131].

The study of anomalies in ionic solutions is important because ionic aqueous solutions are more easily supercooled than bulk water as the temperature of homogeneous nucleation shifts to lower temperature upon increasing concentration [41]. In ionic solutions, the position of the liquid-vapour critical point moves to higher temperatures and pressures, following the slope of the liquid-vapour coexistence line (see Ref. [40] and references therein). Up to today very little is known on the effect of the ions on the hypothesized LLCP. Some authors [133, 134] reported that ions seem to be more favorably solvated in the HDL phase. Mishima [134, 135] reported experimental evidences of a possible liquid-liquid transition in LiCl(aq).

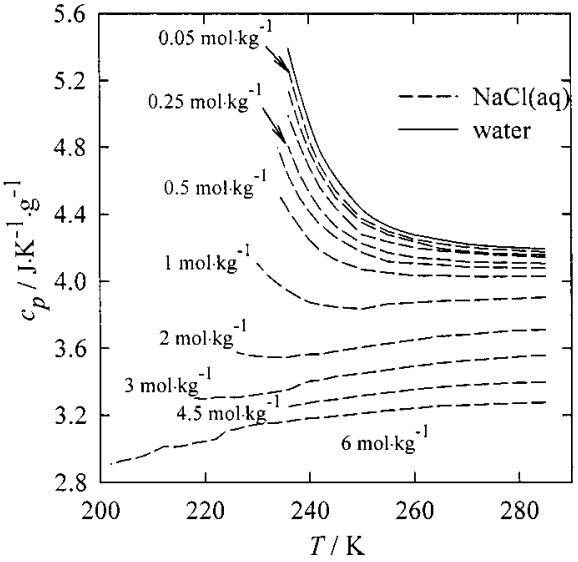

Figure 2.15: Isobaric specific heat for water and for NaCl(aq) at different concentrations obtained by experiments performed with differential scanning calorimetry. Data and figure from Ref. [131].

A large body of experimental [136–145] and computer simulations [146–159] papers exists regarding the structural properties of ionic solutions, especially at ambient temperature. The modifications of water-water structure induced by the ions have been studied in a number of papers [136–141, 146–150]. Depending on the effect that ions have on water structure, they have been in the past classified as *structure-makers* or *structure breakers*. This classification is mainly qualitative [146] and the legitimacy of its usage has been recently challenged [137, 138, 142]. Structure-making ions are supposed to induce a rearrangement of nearby water molecules that results in a ordered hydration structure. This would be attained with actual breaking of bonds between water molecules in order to reorganize them around the ion. Conversely structure-breaking ions are believed only to weaken or distort hydrogen bonds of surrounding water molecules, with no actual breaking of bonds. Works dealing with ion-ion structure [140, 142, 143, 147, 151, 152, 154, 155] are usually mainly concerned with the presence or absence of cluster of ions. The formation of large clusters of ions has been observed both in experiments [143] and in computer simulations [152, 154, 155]. The ion-water (or hydration) structure has been intensely investigated [136, 138, 140–142, 144, 145, 147, 149, 152, 155–159]. So far most of the work has been done at ambient temperature, with few papers focusing on the supercooled region [148, 159].

2.5.2 Apolar solutes

Phenomena related to the solvation of apolar solutes in water are interesting for a variety of problems, such as biological membranes formation, globular protein folding and the stability of mesoscopic assembly [34–36, 160]. In the past a large number of papers have addressed the problem of hydrophobic hydration (see for example Refs. [22, 35, 150, 161–171]). Small apolar solutes, such as alkanes and noble gases are poorly soluble in water but one intriguing anomaly of water in solutions is the very large increase in the solubility of hydrophobic gases upon decreasing temperature [172].

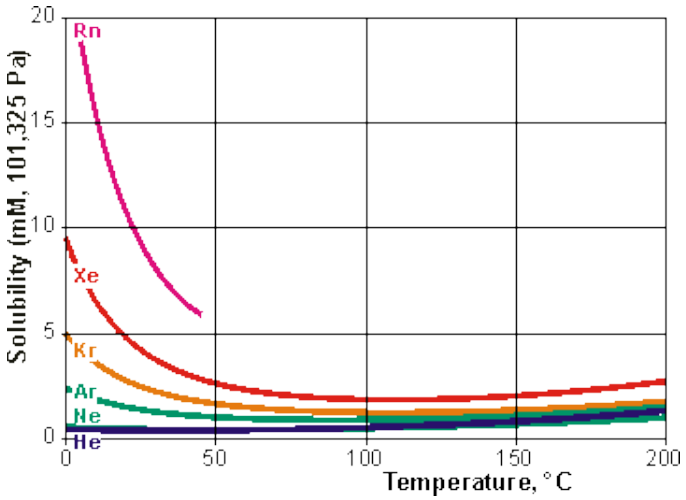

Figure 2.16: Experimental solubilities of noble gases in water at ambient pressure as a function of the temperature. Data from Ref. [173] and figure from Ref. [76].

In Fig. 2.16 the experimental solubilities of noble gases at ambient pressure as a function of the temperature is shown. The solubility of small hydrophobic solutes decreases upon decreasing the temperature until a minimum is reached in the temperature range from $T = \simeq 310$ K to $T \simeq 350$ K. When the temperature is further decreased, the solubility increases monotonically [35, 162]. The solvation free energy of these kinds of solutes is large and positive due to the large entropy contribution but these quantities have a marked temperature dependence that cause the increase of solubility at low temperatures [172]. The solubility of model hydrophobic particles, namely hard spheres (HS) in the JRP particles we mentioned in Sec. 2.4 (see Sec. 6.2 for details) has been recently assessed [35]. It was found that the mixture of HS and JRP particles shows a temperature of minimum solubility, similarly to experimental results for water. Moreover it was observed that HS are

more favorably solvated in low density phases of water, as previously found in computer simulations on TIP5P water [22].

The effect of apolar solutes on the anomalies of water was studied with an analytic model for water [128]. It was found that the anomalies in the thermodynamic response functions and the TMD are still present when small apolar solutes are added to water, at least for low mole fractions of solutes. The thermodynamics and the structure in the supercooled region was studied for water embedded in a matrix of soft hydrophobic spheres [54]. Some of the result of this work will be discussed in comparison to the PR-TIP4P set in Chap. 4.

The effect of the presence of hydrophobic solutes on the vapour-liquid critical points was studied for solutions of hydrocarbons in water [40]. For these systems it was found that the critical line starting from the bulk water critical point shifts to lower temperatures and higher pressures and then it reverts, through a knee to higher temperatures. The effect of weak interacting apolar solute on the LLCP was studied with an analytical model [129] and it was found that the temperature of occurrence of the LLCP can be elevated, using a certain class of apolar solutes.

Chapter 3

Molecular Dynamics

Computer simulations have a dominant role in the study of the physics of liquid matter. After the first pioneering works [174–176], computer simulations techniques have evolved following the progressive increased availability of computing power and nowadays they are the preferred theoretical methods for the investigation of the properties of liquids. This happens partly because the equations describing the statics and the dynamics of liquids cannot often be solved analytically and the approximations used to deal with them do not always work well. In the case of the static properties for example, the *Ornstein-Zernike* equation can only be solved approximately. The two most used approximations are the *Percus-Yevick* and the *hyper-netted chain* approximations but when compared to the experimental results they do not always give encouraging results [177].

This chapter covers the general concepts of the molecular dynamics (MD) technique. The first section, Sec. 3.1, deals with the main steps of this simulation method. In the following sections details about the integration algorithm, Sec. 3.2, thermostats and barostats in MD, Sec. 3.3, and the Ewald summation method, Sec. 3.4, are discussed.

The MD technique was used in this thesis for the investigation of the PR-TIP4P and the JJ-TIP4P sets. The specific simulations details for these two sets will be reported in the respective chapter with the results: chap. 4 for the PR-TIP4P set and chap. 5 for th JJ-TIP4P set. For the study of the HS-JRP set the discrete molecular dynamics (DMD) technique was employed. The key ideas of the DMD and the specific details for the HS-JRP set will be given in Chap. 6 together with the results for the this set.

3.1 The MD technique

Classical MD is a deterministic simulation method that allows the calculation of thermodynamic, static and dynamic properties of a many-body system [178]. The motion of the particles (atoms or molecules) that constitute the system is determined solving Newton's equations. With a fixed number of particles the Hamiltonian of the simulated system is in general given by

$$H = \sum_{i=1}^{N} \frac{\mathbf{p}_i^2}{2m} + U(\mathbf{r}_1, \mathbf{r}_2, \ldots, \mathbf{r}_N) = \sum_{i=1}^{N} \frac{\mathbf{p}_i^2}{2m} + \sum_{i=1}^{N} \sum_{j>1}^{N} u(|\mathbf{r}_i - \mathbf{r}_j|) \tag{3.1}$$

where N is the total number of particles and U is the many-body interaction potential. In the right-hand side of the equation we are assuming that U can be approximated with the sum of the radial potentials u between pairs of particles.

The particles are subject to Newton's laws of motion

$$m_i \ddot{\mathbf{r}}_i = \frac{d\mathbf{p}_i}{dt} = \mathbf{F}_i = -\nabla_{\mathbf{r}_i} U \tag{3.2}$$

$$\mathbf{v}_i = \dot{\mathbf{r}}_i = \frac{\mathbf{p}_i}{m_i} \quad . \tag{3.3}$$

Given the positions and the velocities of the particles at time t, the equations of motion are integrated with discrete time steps δt and the positions and the velocities of the particles at time $t + \delta t$ are computed. The trajectories of the particles are thus determined in a deterministic way. Details about the integration algorithm are given in Sec. 3.2. From the microscopic motion it is possible to evaluate macroscopic quantities using statistical mechanics. In the MD technique the validity of the *ergodic hypothesis* is implied. If we consider a generic thermodynamic quantity A, then under the ergodic hypothesis

$$\langle A \rangle = \int A(\mathbf{r}^N, \mathbf{p}^N) \rho \left[H(\mathbf{r}^N, \mathbf{p}^N) \right] d\mathbf{r}^N d\mathbf{p}^N = \bar{A} = \lim_{t \to \infty} \frac{1}{t} \int_0^t A(\mathbf{r}^N, \mathbf{p}^N) dt' \tag{3.4}$$

the average calculated over the ensemble is identical to the average calculated over time steps. In MD this hypothesis holds when the simulation time exceeds by far the characteristic time of molecular motion. Simulation runs are usually divided into two parts. During the equilibration runs the system

is evolved until equilibrium is reached and the thermodynamic properties and in particular the energy of the system remain constant over time. This can be done by rescaling the velocities, as explained in Sec. 3.3. In the production runs, the trajectories are accumulated and then average quantities are computed.

If we are working in the microcanonical ensemble, the total energy of the system $E = K + U$ is conserved. Methods to deal with MD in different ensembles are discussed in Sec. 3.3. In the NVE ensemble the temperature can be calculated from the equipartition theorem by the relation

$$T = \frac{2}{3}\frac{\langle K \rangle}{k_B} = \frac{1}{3}\frac{\sum_{i=1}^{N} m_i v_i^2}{k_B N} \tag{3.5}$$

while the pressure can be calculated using the virial theorem [178], with P given by

$$P = \frac{N k_B T + \langle \mathcal{V} \rangle}{V} \tag{3.6}$$

where $\mathcal{V} = \frac{1}{3}\sum_{i=1}^{N} \mathbf{r}_i \cdot \mathbf{F}_i$ is the virial.

Let us suppose that our simulation box is cubic and the edge of the box is L (thus $V = L^3$). To avoid introducing artifacts due to the presence of the surfaces of the cube, it is necessary to implement periodic boundary conditions. The central simulation box is replicated in all directions forming an infinite lattice. As a consequence a particle leaving the central box corresponds to its image entering the box from the opposite side. With the *minimal image convention*, a reference particle in the central box interacts only with the particles and the image particles contained in a cube centered on the reference particle and with the same dimensions of the simulation box.

Usually the interaction potential is not calculated for all distances but a truncation is introduced. Only the interaction distances for which $r_{ij} = |\mathbf{r}_i - \mathbf{r}_j| < r_{\text{cut}} \leq L/2$ are retained for the computation of the interactions. With the cut-off, one needs to introduce long range corrections to the interaction potential. For short range potentials, as the Lennard-Jones (LJ) potential, the standard corrections [178,179] for the potential energy and for the virial are given respectively by

$$u_{ij}^{\text{corr}} = 2\pi \frac{N_i N_j}{V} \int_{r_{\text{cut}}}^{\infty} g_{ij}(r) u_{ij}(r) r^2 \, dr \tag{3.7}$$

$$\mathcal{V}_{ij}^{\text{corr}} = -2\pi \frac{N_i N_j}{V} \int_{r_{\text{cut}}}^{\infty} g_{ij}(r) \frac{\partial}{\partial r} u_{ij}(r) r^3 \, dr \tag{3.8}$$

where $g_{ij}(r)$ is the pair radial distribution function (RDF) between particle i and particle j. It is usual to take $g_{ij}(r) = 1$ for $r > r_{\text{cut}}$. For long range potentials, as the electrostatic potential, special care is required. The Ewald summation method for the treatment of the electrostatic interactions is discussed in Sec. 3.4.

3.2 MD integration algorithms

In order to calculate the trajectories of the particles subject to Newtons's laws, Eq. (3.2)-(3.3), we need an integration algorithm. The integration time step must be much less than the time taken by the molecule to cover a distance equal to its own length. Typically $\delta t = 10^{-15}$ s = 1 fs for phenomena that take place at the picoseconds or nanoseconds scale. Let us suppose that, as in the case of water, the particles are rigid molecules. In this case the motion can be separated into translational and rotational motion.

The integration of the translational motion is quite straightforward. The most common algorithm is called *leap-frog* algorithm and it is derived from Verlet's algorithm [178]. The latter considers the Taylor expansion for the position, the velocity and the acceleration of a molecule

$$\mathbf{r}_i(t+\delta t) = \mathbf{r}_i(t) + \mathbf{v}_i(t)\delta t + \frac{1}{2}\mathbf{a}_i\delta t^2 + ... \tag{3.9}$$

$$\mathbf{v}_i(t+\delta t) = \mathbf{v}_i(t) + \mathbf{a}_i(t)\delta t + \frac{1}{2}\mathbf{b}_i\delta t^2 + ... \tag{3.10}$$

$$\mathbf{a}_i(t+\delta t) = \mathbf{a}_i(t) + \mathbf{b}_i(t)\delta t + ... \quad . \tag{3.11}$$

If we now take $\mathbf{r_i}(t-\delta t) = \mathbf{r_i}(t) - \mathbf{v_i}(t)\delta t + \frac{1}{2}\mathbf{a_i}\delta t^2 + ...$ and sum it to Eq. (3.9) we can eliminate the velocity term from the equation for the position, obtaining

$$\mathbf{r}_i(t+\delta t) = -\mathbf{r}_i(t-\delta t) + 2\mathbf{r}_i(t) + \mathbf{a}_i\delta t^2 + \mathcal{O}(\delta t^4) \tag{3.12}$$

making the algorithm faster. In the Verlet procedure the velocity can be recovered calculating

$$\mathbf{v}_i(t) = \frac{\mathbf{r}_i(t+\delta t) - \mathbf{r}_i(t-\delta t)}{2\delta t} \quad . \tag{3.13}$$

Verlet's algorithm is fast and robust but it does not allow an accurate computation of the velocities. This can be amended with the leap-frog algorithm.

Given the quantities $\mathbf{r}_i(t)$, $\mathbf{a}_i(t)$ e $\mathbf{v}_i(t - \frac{1}{2}\delta t)$ a two step iteration is made, in which first the velocities are updated through

$$\mathbf{v}_i(t + \frac{1}{2}\delta t) = \mathbf{v}_i(t - \frac{1}{2}\delta t) + \mathbf{a}_i(t)\delta t \tag{3.14}$$

then the positions of the particles are calculated with

$$\mathbf{r}_i(t + \delta t) = \mathbf{r}_i(t) + \mathbf{v}_i(t + \frac{1}{2}\delta t)\delta t \quad . \tag{3.15}$$

The forces are calculated after the second step and the new accelerations can be put into Eq. (3.14) to begin a new iteration. A diagram of the leap-frog iteration algorithm is depicted in Fig. 3.1.

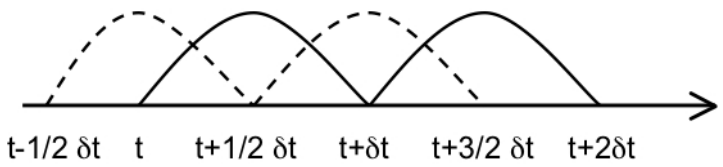

Figure 3.1: Schematic representation of the leap-frog algorithm. Dashed lines represent the first step, Eq. (3.14), with the calculation of the velocities while solid lines represent the second step, Eq. (3.15), with the calculation of the positions.

The leap-frog algorithm yields more accurate positions. They are in fact calculated using a velocity at a time closer to $t + \delta t$. The forces are computed taking the derivative of the potential generated by the distribution of particles ensuing from Eq. (3.15). Velocities at time t can be simply obtained from the relation

$$\mathbf{v}_i(t) = \frac{\mathbf{v}_i(t + \frac{1}{2}\delta t) - \mathbf{v}_i(t - \frac{1}{2}\delta t)}{\delta t} \quad . \tag{3.16}$$

The integration of the rotational motion of molecules requires a more complex treatment. The vector $\boldsymbol{\tau}_i$, the torque with respect to the centre of mass of the molecule positioned at $\mathbf{r}_i$, is defined by

$$\boldsymbol{\tau}_i = \sum_a (\mathbf{r}_{ia} - \mathbf{r}_i) \wedge \mathbf{F}_{ia} = \sum_a \mathbf{d}_{ia} \wedge \mathbf{F}_{ia} \tag{3.17}$$

where $\mathbf{d}_{ia}$ denotes the position of the atom a within the molecule i with respect to its centre of mass. The orientation of a rigid body in the space can be defined by a rotation matrix that consents the transformation from the frame of reference of the laboratory to the one of the centre of mass.

This matrix is usually defined in terms of three independent angular parameters, the *Euler angles* (φ, θ, ψ). A quadri-dimensional vector, with unitary norm, can be defined as a function of the Euler angles. This vector is called *quaternion* and it permits to have convergent equations of motion. Defined $\mathbf{q}$ as

$$\mathbf{q} = (q_0, q_1, q_2, q_3) \quad \text{with} \quad q_0^2 + q_1^2 + q_2^2 + q_3^2 = 1 \tag{3.18}$$

the rotation matrix can be written in terms of $\mathbf{q}$. It reads

$$R = \begin{pmatrix} q_0^2 + q_1^2 - q_2^2 - q_3^2 & 2(q_1 q_2 + q_0 q_3) & 2(q_1 q_3 - q_0 q_2) \\ 2(q_1 q_2 - q_0 q_3) & q_0^2 - q_1^2 + q_2^2 - q_3^2 & 2(q_2 q_3 + q_0 q_1) \\ 2(q_1 q_3 + q_0 q_2) & 2(q_2 q_3 - q_0 q_1) & q_0^2 - q_1^2 - q_2^2 + q_3^2 \end{pmatrix} \quad , \tag{3.19}$$

and if $\hat{\mathbf{d}}_{ia}$ is the position of the atom a in the center of mass frame, its position in the laboratory frame is obtained by $\mathbf{d}_{ia} = R^T \hat{\mathbf{d}}_{ia}$. The quaternion for each molecule satisfies the equations of motion:

$$\begin{pmatrix} \dot{q}_0 \\ \dot{q}_1 \\ \dot{q}_2 \\ \dot{q}_3 \end{pmatrix} = \frac{1}{2} \begin{pmatrix} q_0 & -q_1 & -q_2 & -q_3 \\ q_1 & q_0 & -q_3 & q_2 \\ q_2 & q_3 & q_0 & -q_1 \\ q_3 & -q_2 & q_1 & q_0 \end{pmatrix} \begin{pmatrix} 0 \\ \omega_x \\ \omega_y \\ \omega_z \end{pmatrix} \tag{3.20}$$

where $(0, \omega_x, \omega_y, \omega_z)$ are the components of the angular velocity vector $\boldsymbol{\omega}$ in the centre of mass frame. This system does not possess singularities and it can be solved with a procedure similar to the one applied for the integration of the translational motion. To solve the rotational motion we can use the equation:

$$\frac{d\mathbf{J}}{dt} = \frac{d}{dt}(I\boldsymbol{\omega}) = \boldsymbol{\tau} \tag{3.21}$$

where $\mathbf{J}$ is the total angular momentum of the molecule, I the moment of inertia matrix and $\boldsymbol{\tau}$ the torque of the molecule (for convenience here we drop the subscript i indicating each molecule). This equation is evidently coupled to Eq. (3.20). Having stored $\mathbf{J}(t - \frac{1}{2}\delta t)$, $\mathbf{q}(t)$ and $\boldsymbol{\tau}(t)$ the equations for the rotational motion can be solved iteratively, first updating the angular momentum through:

$$\mathbf{J}(t) = \mathbf{J}(t - \frac{1}{2}\delta t) + \boldsymbol{\tau}(t)\frac{1}{2}\delta t \quad . \tag{3.22}$$

Then the $\dot{\mathbf{q}}$ can be calculated from Eq. (3.20) and a guess for $\mathbf{q}(t + \frac{1}{2}\delta t)$ is given by

$$\mathbf{q}(t+\frac{1}{2}\delta t) = \mathbf{q}(t) + \dot{\mathbf{q}}(t)\frac{1}{2}\delta t \quad . \tag{3.23}$$

The last two are auxiliary equations to estimate $\mathbf{q}(t+\frac{1}{2}\delta t)$ and calculate $\dot{\mathbf{q}}$ at the half-step time. Now the new $\mathbf{J}$ and $\mathbf{q}$ can be calculated through the relations:

$$\mathbf{J}(t+\frac{1}{2}\delta t) = \mathbf{J}(t-\frac{1}{2}\delta t) + \boldsymbol{\tau}(t)\delta t \tag{3.24}$$

$$\mathbf{q}(t+\delta t) = \mathbf{q}(t) + \dot{\mathbf{q}}(t+\frac{1}{2}\delta t)\delta t \quad . \tag{3.25}$$

3.3 Thermostats and barostats in MD

In Sec. 3.1 we have seen that the basic MD algorithm is thought in the micro-canonical NVE ensemble. However it is possible to implement algorithms that simulate the presence of a thermostat and/or a barostat. Therefore MD can be performed in different ensembles such as the canonical NVT ensemble or the isothermal-isobaric NPT ensemble.

For the thermostat, the most common techniques are known as Nosé-Hoover [180], Berendsen [181] and Gaussian constraint [182]. Only the first one reproduces exactly the trajectories in the canonical ensemble. The others give properties that differ from the averages in the canonical ensemble, typically of $\mathcal{O}(1/N)$ [178]. In most cases this accuracy is enough and indeed the Berendsen algorithm is by far the most used in MD simulations. In the Berendsen algorithm the velocities are rescaled through $\dot{\mathbf{r}}_i \to s\dot{\mathbf{r}}_i$ and the change in temperature per time step in terms of the rescaling parameter s is given by:

$$s = \left[1 + \frac{\delta t}{\tau_T}\left(\frac{T_0}{T} - 1\right)\right]^{1/2} \tag{3.26}$$

where τ_T is the time constant of the coupling to the external bath and T_0 is the desired temperature.

In general the coupling of the system to a thermostat and/or a barostat can be effectively obtained also adding terms to the Lagrangian of the system, thus modifying the equations of motions. The general Lagrangian of a system is

$$\mathcal{L} = \frac{1}{2}m\sum_{i=1}^{N}|\dot{\mathbf{r}}_i|^2 - U \quad . \tag{3.27}$$

In the case of a thermostat, we insert a thermal bath and rescale the velocities writing $\dot{\mathbf{r}}_i \to s\dot{\mathbf{r}}_i$. The new Lagrangian in terms of the rescaled quantities is

$$\mathcal{L} = \frac{1}{2}m\sum_{i=1}^{N} s^2 \left|\dot{\mathbf{r}}_i\right|^2 - U + \frac{Q}{2}\dot{s}^2 - (3N+1)k_B T_0 \ln s \tag{3.28}$$

where Q is the "mass" associated with the thermal bath. The modified equations of motions that are obtained are of the kind

$$\ddot{\mathbf{r}}_i = -\frac{1}{m_i s^2}\frac{\partial U}{\partial \mathbf{r}_i} - \frac{2\dot{s}}{s}\dot{\mathbf{r}}_i \tag{3.29}$$

$$Q\ddot{s} = \frac{1}{s}\left[\sum_i m_i s\dot{\mathbf{r}}_i^2 - (3N+1)k_B T_0\right] \tag{3.30}$$

With this method the energy of the system is not conserved but the energy of the total system constituted by the system plus the thermal bath is conserved.

Beyond the canonical ensemble, another common working ensemble is the isothermal-isobaric NPT ensemble. In analogy with what we have seen for the temperature, algorithms can be implemented to fix the pressure, adjusting dynamically the volume and in case the shape of the simulation box. The most common algorithms for the introduction of a barostat are known as Hoover [183] and Berendsen [181].

3.4 Ewald summation

For long range interactions, such as the electrostatic interactions, the cut-off plus corrections method described in Sec. 3.1 is not sufficient to achieve accuracy. In this case, special care is needed in dealing with potential truncation and long range contributions. As a matter of fact the inadequate treatment of electrostatic interactions can lead to severe artifacts in the results of the simulations [25]. There exist several methods for the treatment of the electrostatic interactions. In the following the general ideas of the most used method, the Ewald summation method, are described.

Taking into account the periodic boundary conditions, the electrostatic energy term of the interaction potential can be written as

$$U_E = \frac{1}{2}\sum_{i=1}^{N} q_i \phi_E(\mathbf{r}_i) \tag{3.31}$$

and ϕ_E is given by

$$\phi_E = \sum_{j=1}^{N} \sum_{\mathbf{R}} \frac{q_j}{|\mathbf{r}_{ij} + \mathbf{R}|} \tag{3.32}$$

where $\mathbf{R} = \mathbf{n}L$, $\mathbf{n} = (n_x, n_y, n_z)$, with $n_x, n_y, n_z \in \mathbb{Z}$. The sum is performed with the convention that $i \neq j$ if $\mathbf{R} = \mathbf{0}$.

By adding and subtracting screening charges, we can break the sum into two parts, $U_E = U_{\mathrm{SR}} + U_{\mathrm{LR}}$. The first part contains the original point charges screened by diffuse clouds of opposite charges; this part becomes short ranged and can be evaluated in the real space. The second part compensate for the added screening charges and it is generated by the sum of the screening charge densities (with opposite charge); it is evaluated in the Fourier space. The screening charges are typically taken with a Gaussian distribution:

$$\rho_s(r) = -q_i \left(\frac{\alpha}{\pi}\right)^{3/2} e^{-\alpha r^2} \quad . \tag{3.33}$$

First let us calculate the long range part of the sum. Having taken the screening charges as in Eq. (3.33), the compensating charge distribution can be written as

$$\rho_c(\mathbf{r}) = \sum_{j=1}^{N} \sum_{\mathbf{R}} q_j \left(\frac{\alpha}{\pi}\right)^{3/2} \exp[-\alpha|\mathbf{r} - (\mathbf{r}_j + \mathbf{R})|^2] \tag{3.34}$$

and its Fourier transform is given by

$$\tilde{\rho}_c(\mathbf{k}) = \int_V d\mathbf{r}\, e^{-i\mathbf{k}\cdot\mathbf{r}} \rho_c(\mathbf{r}) = \sum_{j=1}^{N} q_j e^{-i\mathbf{k}\cdot\mathbf{r}_j} e^{-k^2/4\alpha} \quad . \tag{3.35}$$

The field generated by this charge distribution can be calculated using the Poisson's equation in the Fourier space, $k^2\tilde{\phi}(\mathbf{k}) = 4\pi\tilde{\rho}(\mathbf{k})$. Anti-transforming the field thus obtained and plugging it into the long range part of the sum, we obtain

$$U_{\mathrm{LR}} = \frac{1}{2} \sum_{i=1}^{N} q_i \phi_c(\mathbf{r}_i) = \frac{1}{2V} \sum_{\mathbf{k}\neq 0} \frac{4\pi}{k^2} |\tilde{\rho}(\mathbf{k})|^2 e^{-k^2/4\alpha} \tag{3.36}$$

where $\tilde{\rho}(\mathbf{k}) = \sum_{i=1}^{N} q_i e^{-i\mathbf{k}\cdot\mathbf{r}_i}$. This part of the potential contains spurious self-interactions terms as the point charges at $\mathbf{r}_i$ interact with the compensating charges also at $\mathbf{r}_i$. The self interactions terms represent the potential at

center of the Gaussian charge distributions and they are to be subtracted from the final expression to recover the correct Coulombic energy.

Now we calculate the short range part of the sum. Using the Poisson's equation in the real space $-\nabla^2\phi(\mathbf{r}) = 4\pi\rho(\mathbf{r})$ it is possible to demonstrate that the screening potential can be written as

$$\phi_s(r) = \frac{q_i erf(\alpha^{1/2} r)}{r} \tag{3.37}$$

where *erf* is the error function. It is defined by

$$erf(x) = \frac{2}{\pi^{1/2}} \int_0^x e^{-t^2}\, dt \quad . \tag{3.38}$$

The self-interaction terms correspond to $\phi_{\text{self}} = \phi_s(0) = 2\left(\frac{\alpha}{\pi}\right)^{1/2} q_i$ and the total self-interaction energy becomes

$$U_{\text{self}} = \left(\frac{\alpha}{\pi}\right)^{1/2} \sum_{i=1}^{N} q_i^2 \tag{3.39}$$

which must be subtracted from the total electrostatic energy. Using the result (3.37), the short range part of the sum can be rewritten as

$$\begin{aligned} U_{\text{SR}} = \frac{1}{2} \sum_{\mathbf{R}} \sum_{i \neq j}^{N} q_i q_j \left[\frac{1}{|\mathbf{r}_{ij} + \mathbf{R}|} - \frac{erf\left[\alpha^{1/2} |\mathbf{r}_{ij} + \mathbf{R}|\right]}{|\mathbf{r}_{ij} + \mathbf{R}|} \right] = \\ = \frac{1}{2} \sum_{\mathbf{R}} \sum_{i \neq j}^{N} q_i q_j \frac{erfc\left[\alpha^{1/2} |\mathbf{r}_{ij} + \mathbf{R}|\right]}{|\mathbf{r}_{ij} + \mathbf{R}|} \end{aligned} \tag{3.40}$$

with the *erfc* function defined by

$$erfc(x) = \frac{2}{\pi^{1/2}} \int_x^{+\infty} e^{-t^2}\, dt \quad . \tag{3.41}$$

Putting all the terms together we finally obtain:

$$\begin{aligned} U_E = U_{\text{SR}} + U_{\text{LR}} - U_{\text{self}} = \frac{1}{2} \sum_{\mathbf{R}} \sum_{i \neq j}^{N} q_i q_j \frac{erfc\left[\alpha^{1/2} |\mathbf{r}_{ij} + \mathbf{R}|\right]}{|\mathbf{r}_{ij} + \mathbf{R}|} \\ + \frac{1}{2V} \sum_{\mathbf{k} \neq 0} \frac{4\pi}{k^2} |\tilde{\rho}(\mathbf{k})|^2 e^{-k^2/4\alpha} - \left(\frac{\alpha}{\pi}\right)^{1/2} \sum_{i=1}^{N} q_i^2 \end{aligned} \tag{3.42}$$

The original sum has been thus separated into two parts. The short range sum is performed in the real space while the long range sum is performed in the Fourier space. The tuning of the parameter α results particularly important in determining the convergence of the integrals. In order to get fast convergence α should be large in the real space and small in the Fourier space. A balance of these needs is usually considered and typically alpha is set to values of the order of $5/L$ [178], taking a number of wave vectors of the order of ten for the computation of the sums over $\mathbf{k}$.

Chapter 4

Results for the PR-TIP4P set

In this chapter the results obtained for the PR-TIP4P are presented. The set consists in the molecular dynamics (MD) simulations of bulk water and NaCl(aq) with concentrations $c = 0.67, 1.36$ and 2.10 mol/kg [43–48]. This set of simulations was focused on studying the modifications on the properties of water induced by the ions in the supercooled region and the role of concentration. The first section, Sec. 4.1, provides the details of the simulations performed for this set. A study on the effect of the size of the system is presented in Sec. 4.2. In Sec. 4.3 the results concerning the thermodynamics of the systems are shown, while the structural results are discussed in Sec. 4.4.

4.1 Simulation details for the PR-TIP4P set

The PR-TIP4P set consists in the simulation study of four systems: bulk TIP4P water and the solutions of sodium chloride in TIP4P water, NaCl(aq), with concentrations $c = 0.67, 1.36$ and 2.10 mol/kg, performed using the Pettitt-Rossky (PR) ion parameters [52]. The simulations of bulk water and $c = 0.67$ mol/kg NaCl(aq) [43, 45, 47] were partly performed for the Master Degree (*Laurea Magistrale*) thesis and are reported here for comparison. The simulations of the $c = 1.36$ and $c = 2.10$ mol/kg [44, 46–48] were performed during the first year of the Ph. D. program (*Dottorato di Ricerca*).

For water, there exist many models that can be used in computer simulations [184]. The most commonly used are ST2 (Stillinger and Rahaman model) [164], SPC (*simple point charge*) [185], SPC/E (*simple point charge extended*) [186], TIP5P (*transferable intermolecular potential with five points*) [187] and TIP4P (*transferable intermolecular potential with four points*) [188]. The performance of these models in the reproduction of the experimental

properties of liquid water is not uniform throughout the whole phase diagram. Overall the TIP4P model appears to be the best performing model, being able to reproduce the main feature of the phase diagram of water, especially for its numerous solid phases [189]. From this consideration we can expect the TIP4P to work well also for the reproduction of the properties of supercooled liquid water.

In the TIP4P model the Lennard-Jones (LJ) and the electrostatic parts of the potential for the oxygen atom are spatially separated. The two hydrogen atoms and the LJ site of the oxygen atom lie on a plane while the electrostatic site of the oxygen atom, called X, is situated on the bisector of the H-O-H angle (of amplitude $\theta = 104.52°$), tilted of an angle $\phi = 52.56°$ with respect to the O-H axis. The O-H distance is $l_1 = 0.9572$ Å, while the the O-X distance is $l_2 = 0.15$ Å. The partial charges of the sites are $q_1 = +0.52e$ for the hydrogen atoms and $q_2 = -1.04e$ for the oxygen (X site) atom. The LJ interaction parameters for the TIP4P model are $\epsilon_{OO} = 0.648$ kJ/mol and $\sigma_{OO} = 3.154$ Å. No LJ interaction is set on the hydrogen atoms. The geometry of the water TIP4P molecule is represented in Fig. 4.1.

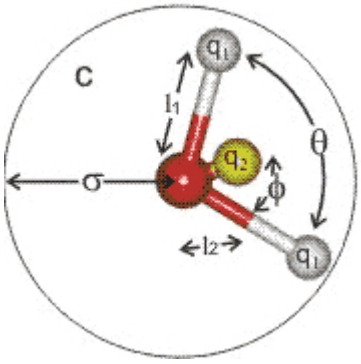

Figure 4.1: Geometry of the TIP4P water model. The values of the parameters are $l_1 = 0.9572$ Å, $l_2 = 0.15$ Å, $\theta = 104.52°$, $\phi = 52.56°$, $q_1 = +0.52e$, $q_2 = -1.04e$, $\sigma = 3.154$ Å.

For the simulations in the PR-TIP4P set, the interaction potential between particles is given by the sum of the LJ potential and the electrostatic potential

$$U_{ij}(r) = \frac{q_i q_j}{r} + 4\epsilon_{ij}\left[\left(\frac{\sigma_{ij}}{r}\right)^{12} - \left(\frac{\sigma_{ij}}{r}\right)^{6}\right] \quad . \tag{4.1}$$

The LJ interaction parameters and the charges of water are those of the TIP4P model.

For the ions the electrostatic charges are $+e$ for the Na^+ ion and $-e$ for the Cl^- ion. The LJ ion parameters were taken from Pettitt and Rossky [52]. The PR parameters were originally derived for the Huggins-Mayer [190] form of the potential

$$U_{ij}(r) = \frac{q_i q_j}{r} + B_{ij} e^{-r/\rho_{ij}} - \frac{C_{ij}}{r^6} \tag{4.2}$$

where B_{ij}, ρ_{ij} and C_{ij} are the potential parameters.

They were calculated using an integral equation approach to yield the interatomic potential of mean force at infinite dilution for a model reproducing alkali halides in water [52]. For the fitting of the parameters the experimental data on molten salts by Fumi and Tosi were used [191].

Koneshan and Rasaiah [147] reparametrised this potential in order to use a LJ form. For this set of parameters, in order to balance Cl-H interactions, LJ interactions between ions and hydrogen atoms were included and taken to be equal to the LJ interactions between ions and oxygen [152]. The PR ion-water and ion-ion parameters for the LJ form of the potential, used in this work, are reported in Table 4.1

Table 4.1: PR ion-water and ion-ion LJ interaction parameters [52, 147].

Atom pair	ϵ_{ij} (kJ/mol)	σ_{ij} (Å)
Na-O	0.560 14	2.720
Na-H	0.560 14	1.310
Cl-O	1.505 75	3.550
Cl-H	1.505 75	2.140
Na-Na	0.119 13	2.443
Cl-Cl	0.979 06	3.487
Na-Cl	0.352 60	2.796

The cut-off radius for all the simulations was set to 9 Å. Usual values of the cut-off radius are between 8 Å and 10 Å [192]. The long range electrostatic interactions were treated using the Ewald summation method (see Sec. 3.4 for theory). The integration time step was set to 1 fs. The temperature was controlled using the Berendsen thermostat [181]. The volume was fixed at the chosen values and pressure was calculated from the virial theorem. The simulations were performed using the DL_POLY 2.18 package [179].

The simulations were carried out in cubic simulation box, with edge length L. Most simulations were performed using 256 particles. In order to

Table 4.2: Composition of the systems with different sizes. Concentrations are in mol/kg.

Number of molecules	Bulk	$c = 0.67$	$c = 1.36$	$c = 2.10$
N_{tot}=256				
H_2O	256	250	244	238
Na^+ Cl^-	-	3	6	9
N_{tot}=512				
H_2O	512	500	488	476
Na^+ Cl^-	-	6	12	18
N_{tot}=1024				
H_2O	1024	1000	976	952
Na^+ Cl^-	-	12	24	36

study the dependence of the simulated quantities on the size of the system some state points were simulated with double and 4-fold number of particles. The detailed composition of each studied system for the different sizes is reported in Table 4.2. The results on the dependence on the size of the system are reported in Sec. 4.2.

Densities were spanned from $\rho = 0.800$ g/cm^3 to $\rho = 1.125$ g/cm^3 while the temperature analyzed were $T = 500$, 400, 350, 300, 280, 260, 250, 240, 230, 220 and 210 K. Only for bulk water, in order to investigate the liquid-gas limit of mechanical stability (LG-LMS) line further, other four temperature were simulated for the $\rho = 0.900$ g/cm^3, namely $T = 195$, 190, 185 and 180 K. Moreover two additional points for $\rho = 0.980$ g/cm^3 at $T = 200$ K and $T = 190$ K for $c = 2.10$ mol/kg NaCl(aq) were simulated to investigate the behaviour of the temperature of maximum density (TMD) line. The densities studied for each system and the corresponding box lengths are reported in Table 4.3, for the systems with $N_{tot} = 256$.

In order to create starting configurations the particles were distributed on a face centered cubic lattice. The crystal thus formed was then melted at $T = 500$ K and the temperature was progressively reduced during the equilibration runs. The final configuration for a given temperature was used as starting configuration for the lower one. Some of the thermodynamic points for bulk water were taken from a previous work of our group [54]. The length of the equilibration and production runs are reported in Table 4.4 for temperatures from $T = 500$ K to $T = 260$ K and in Table 4.5 for temperatures from $T = 250$ K to $T = 210$ K. The equilibration/production times for the additional points for bulk water (only for $\rho = 0.900$ g/cm^3) are

Table 4.3: List of the simulated densities for each system with the corresponding box lengths. The total number of particles is $N_{tot} = 256$. Concentrations are in mol/kg.

	Bulk	$c = 0.67$	$c = 1.36$	$c = 2.10$
ρ (g/cm^3)	L (Å)	L (Å)	L (Å)	L (Å)
1.125	-	-	19.137	19.227
1.100	-	19.190	19.281	19.372
1.050	19.396	19.489	19.582	19.674
1.025	-	19.641	19.740	19.833
1.000	19.714	-	-	-
0.980	19.847	19.943	20.038	20.132
0.950	20.054	20.151	20.247	20.342
0.900	20.418	20.517	20.615	20.712
0.870	20.650	20.750	20.849	20.947
0.850	20.811	20.912	21.011	21.110
0.830	20.977	-	-	-
0.800	21.236	21.339	21.440	21.541

10000/8000 ps for $T = 195$ K, 20000/10000 ps for $T = 190$ K, 10000/10000 ps for $T = 185$ K and 20000/10000 ps for $T = 180$ K. For $c = 2.10$ mol/kg NaCl(aq) (only for $\rho = 0.980$ g/cm^3) equilibration/production times for the additional points are 7000/5000 ps for $T = 200$ K and 10000/10000 ps for $T = 190$ K.

For the simulations in the PR-TIP4P set, each isochore required about 10.5 ns of simulation time. As 38 isochores were simulated for the PR-TIP4P set, the total computational time amounts to about 400 ns. On a Linux machine with an Intel dual-core processor (clock frequency 2.2 GHz) simulation times of 2.2 ns/day can be achieved. Thus the total of all the simulations performed for this set required the equivalent of half a year of continuous single CPU usage. For this set of simulations, the serial version of the DL_POLY 2.18 was employed. The simulations for bulk water and for $c = 0.67$ mol/kg NaCl(aq) [43, 45, 47] were carried out on the research group computers, while the simulations of $c = 1.36$ and $c = 2.10$ mol/kg NaCl(aq) [44, 46–48] were conducted partly also on the INFN-Grid Roma Tre cluster [193] and on the HPC machine [194] of the CNR-IOM *Democritos National Simulation Center* at SISSA, Trieste (Italy).

Table 4.4: Simulation times of the equilibration (t_E) and production (t_P) runs for all systems in the PR-TIP4P set for temperatures from $T = 500$ K to $T = 260$ K. The points denoted with * were taken from Ref. [54]. Densities are in g/cm^3 and concentrations in mol/kg.

System	$T = 500$ K t_E/t_P (ps)	$T = 400$ K t_E/t_P (ps)	$T = 350$ K t_E/t_P (ps)	$T = 300$ K t_E/t_P (ps)	$T = 280$ K t_E/t_P (ps)	$T = 260$ K t_E/t_P (ps)
$\rho = 1.125$						
$c = 1.36$	15/15	30/30	50/50	100/80	200/150	300/300
$c = 2.10$	15/15	30/30	50/50	100/100	400/150	300/250
$\rho = 1.100$						
$c = 0.67$	20/15	30/30	50/50	100/100	200/200	300/300
$c = 1.36$	15/15	30/30	50/50	100/100	400/300	
$c = 2.10$	15/15	30/30	50/50	100/100	200/150	600/300
$\rho = 1.050$						
Bulk	*/10	*/25	30/30	*/*	*/*	*/*
$c = 0.67$	20/15	30/30	50/50	100/100	200/200	300/300
$c = 1.36$	15/15	30/30	50/50	100/80	200/150	200/300
$c = 2.10$	15/15	30/30	60/50	200/100	300/150	300/200
$\rho = 1.025$						
$c = 0.67$	20/15	320/20	30/30	50/50	70/75	150/150
$c = 1.36$	15/15	30/30	40/40	60/60	80/80	250/150
$c = 2.10$	15/15	60/30	80/50	200/150	200/150	300/250
$\rho = 1.000$						
Bulk	*/10	*/25	*/*	*/*	*/*	*/*
$\rho = 0.980$						
Bulk	*/10	*/25	30/30	*/*	*/*	*/*
$c = 0.67$	20/15	30/30	50/50	100/100	130/130	600/200
$c = 1.36$	15/15	30/30	50/50	100/100	150/100	250/200
$c = 2.10$	15/15	30/30	50/50	100/100	200/150	300/200
$\rho = 0.950$						
Bulk	*/10	*/25	30/30	*/*	*/*	*/*
$c = 0.67$	20/15	30/30	50/50	100/100	150/150	200/200
$c = 1.36$	15/15	30/30	50/50	100/80	400/200	400/300
$c = 2.10$	15/15	30/30	50/30	100/100	200/150	500/300
$\rho = 0.900$						
Bulk	10/10	20/20	30/30	75/40	90/45	150/100
$c = 0.67$	20/15	30/30	50/50	200/100	200/200	300/300
$c = 1.36$	15/15	30/30	50/30	100/80	200/150	300/250
$c = 2.10$	15/15	30/30	50/50	200/100	200/150	300/200
$\rho = 0.870$						
Bulk	10/10	30/30	50/50	100/100	200/200	300/300
$c = 0.67$	20/20	30/30	50/50	100/100	200/180	300/300
$c = 1.36$	15/15	30/30	50/50	100/80	200/150	300/250
$c = 2.10$	15/15	30/30	100/50	200/100	400/200	600/300
$\rho = 0.850$						
Bulk	10/10	30/30	50/50	100/100	200/200	300/300
$c = 0.67$	20/15	30/30	50/50	100/100	200/200	300/300
$c = 1.36$	25/15	30/30	50/50	100/80	200/150	300/250
$c = 2.10$	15/15	60/30	50/50	200/150	200/150	300/300
$\rho = 0.830$						
Bulk	10/10	30/30	50/50	100/100	200/200	300/300
$\rho = 0.800$						
Bulk	10/10	30/30	50/50	100/100	200/200	300/300
$c = 0.67$	20/15	30/30	50/50	150/150	400/300	400/400
$c = 1.36$	15/15	30/30	50/50	100/80	200/150	300/250
$c = 2.10$	15/15	30/30	50/50	200/100	400/200	600/300

Table 4.5: Simulation times of the equilibration (t_E) and production (t_P) runs for all systems in the PR-TIP4P set for temperatures from $T = 250$ K to $T = 210$ K. The points denoted with * were taken from Ref. [54]. Densities are in g/cm^3 and concentrations in mol/kg.

System	$T = 250$ K t_E/t_P (ps)	$T = 240$ K t_E/t_P (ps)	$T = 230$ K t_E/t_P (ps)	$T = 220$ K t_E/t_P (ps)	$T = 210$ K t_E/t_P (ps)
$\rho = 1.125$					
$c = 1.36$	500/300	800/600	1000/800	1200/1000	1500/1200
$c = 2.10$	500/400	800/600	1500/1000	1200/1000	1500/1500
$\rho = 1.100$					
$c = 0.67$	500/500	800/800	1000/800	1200/1000	1500/1200
$c = 1.36$	500/350	800/600	1000/800	1200/1000	1500/1200
$c = 2.10$	500/400	800/600	1500/1000	1200/1000	1500/1200
$\rho = 1.050$					
Bulk	*/200	*/*	1000/800	1200/1000	1400/1000
$c = 0.67$	500/500	800/800	1000/800	1200/1000	2300/2000
$c = 1.36$	500/350	800/600	1000/800	1200/1000	1500/1200
$c = 2.10$	500/300	800/600	1000/800	1500/1000	1500/1200
$\rho = 1.025$					
$c = 0.67$	200/200	1200/800	1000/1000	1250/1000	1500/1200
$c = 1.36$	300/200	800/600	800/800	1200/1000	1500/1200
$c = 2.10$	550/400	1200/600	1000/800	1200/1000	1500/1200
$\rho = 1.000$					
Bulk	*/200	*/*	1000/800	*/800	1200/1000
$\rho = 0.980$					
Bulk	*/250	*/*	1000/800	1200/1000	2200/2000
$c = 0.67$	500/500	800/600	1000/1000	1200/1000	1500/1200
$c = 1.36$	400/300	500/500	1000/800	1200/1000	1500/1000
$c = 2.10$	800/400	700/500	1500/800	1200/1000	1500/1200
$\rho = 0.950$					
Bulk	*/200	*/*	1000/800	1200/1000	1200/1000
$c = 0.67$	400/400	800/600	1000/800	1200/1000	1500/1200
$c = 1.36$	500/400	1000/600	1000/800	1200/1000	150/1200
$c = 2.10$	800/500	1200/600	100/800	1500/1000	1800/1200
$\rho = 0.900$					
Bulk	2400/1200	1000/750	1000/750	2000/12000	1500/1500
$c = 0.67$	800/750	1000/800	1200/1000	1200/1000	1500/1200
$c = 1.36$	300/250	800/600	1400/800	1800/1000	1500/1200
$c = 2.10$	500/400	1200/600	2000/1000	1200/1000	3000/1500
$\rho = 0.870$					
Bulk	500/500	800/600	1000/800	1200/1000	1500/1200
$c = 0.67$	500/500	750/750	1000/800	1200/1000	1500/1200
$c = 1.36$	1000/800	800/600	1000/800	1200/1000	1500/1200
$c = 2.10$	500/400	800/600	2000/1000	2400/1500	3000/1500
$\rho = 0.850$					
Bulk	500/500	800/600	1000/800	1200/1000	1500/1200
$c = 0.67$	500/500	1000/700	3000/1500	1200/1000	1500/1200
$c = 1.36$	500/300	800/600	1000/800	1600/1000	1500/1200
$c = 2.10$	500/400	1200/600	2000/1000	2400/1200	2000/1500
$\rho = 0.830$					
Bulk	500/500	800/600	1000/800	1200/1000	1500/1200
$\rho = 0.800$					
Bulk	500/500	800/600	1000/800	1200/1000	1500/1200
$c = 0.67$	500/500	800/800	1500/1000	1800/1200	1500/1200
$c = 1.36$	500/300	800/600	1500/800	1200/1000	1500/1200
$c = 2.10$	500/500	800/600	1000/800	1500/1000	1500/1200

4.2 The size of the systems

MD simulations are carried out using a finite number of particles and a finite volume of the simulation box. Thus the conditions of the *thermodynamic limit*, $N \to \infty$, $V \to \infty$, being their ratio $\rho = N/V$, constant cannot be achieved and the calculated quantities might depend on the size of the system. Hence studying the dependence of the computed properties on the size of the system is useful in order to understand how big a system must be in order to be reliable.

In order to inquire a possible dependence of the calculated quantities on the size of the system, we conducted a study on bulk water and on $c = 0.67, 1.36$ and 2.10 mol/kg NaCl(aq) with PR parameters at three different system sizes, $N_{tot} = 256$, $N_{tot} = 512$ and $N_{tot} = 1024$ [47]. The composition of the systems is reported in Table 4.2 of the previous section.

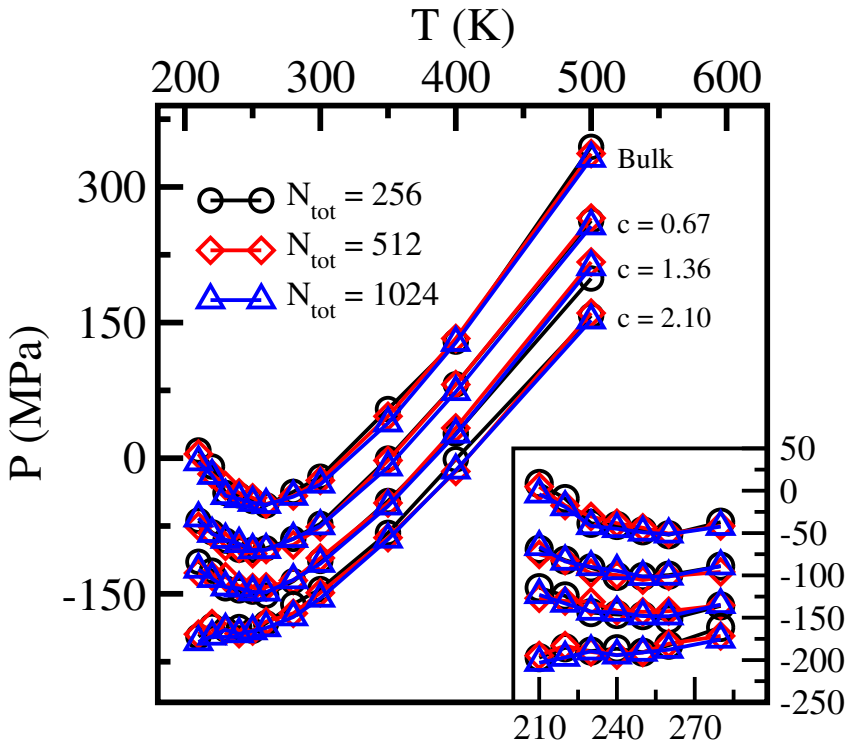

Figure 4.2: Comparison of the $\rho = 0.980$ g/cm^3 isochore for bulk water and for $c = 0.67, 1.36, 2.10$ mol/kg NaCl(aq), simulated with PR parameters and with total number of particles $N_{tot} = 256$ (circles), $N_{tot} = 512$ (diamonds) and $N_{tot} = 1024$ (triangles). In the inset a blow up of the low temperature region is displayed.

Fig. 4.2 shows the $\rho = 0.980$ g/cm^3 isochore simulated for the four sys-

tems, bulk water and $c = 0.67, 1.36, 2.10$ mol/kg NaCl(aq) and at the three sizes. We can note that there are no significant deviations in the curves upon increasing the size of the system. This is true even for the biggest size system, $N_{tot} = 1024$, and even at low temperatures. Therefore it can be concluded that for the systems we are examining, the increase in the size of the systems does not lead to significantly different results, at least for the thermodynamic data. Taking into account also the long simulation times required, especially at low temperatures, the smallest box, $N_{tot} = 256$, was used for most of the simulations as it appears to be big enough to reliably reproduce the thermodynamic properties of the systems.

4.3 Thermodynamic results

The simulated state points have been analysed in the isotherms $(P - \rho)$ plane and in the isochores $(P - T)$ plane. From the study of these thermodynamic planes two important quantities can be calculated. By definition the isothermal compressibility is given by

$$K_T = -\frac{1}{V}\left(\frac{\partial V}{\partial P}\right)_T = \frac{1}{\rho}\left(\frac{\partial \rho}{\partial P}\right)_T \quad . \tag{4.3}$$

As the limit of mechanical stability (LMS) line is defined by the locus of the points for which K_T diverges, the extrema in the isotherms are points of the LMS line. The TMD line is defined by the locus of the points where the coefficient of thermal expansion α_P is zero. As by definition α_P is given by

$$\alpha_P = \frac{1}{V}\left(\frac{\partial V}{\partial T}\right)_P = -\frac{1}{\rho}\left(\frac{\partial \rho}{\partial T}\right)_P = K_T \gamma_V \left(\frac{\partial P}{\partial T}\right)_\rho \tag{4.4}$$

where γ_V is the thermal pressure coefficient, the line that joins the minima of the isochores yields the TMD line.

In Fig. 4.3 the $T = 300$ K, $T = 280$ K, $T = 260$ K, $T = 240$ K, $T = 220$ K and $T = 210$ K isotherms are displayed for the four systems. Minima in the isotherms can be seen for all systems. Following Eq. 4.3, these minima can be identified with points belonging to the LG-LMS line. For high densities the isotherms shift to lower pressures, as the concentration is increased. For low densities, close to the LG-LMS, instead the isotherms slightly rise in pressure and the LG-LMS minimum becomes more shallow. It can be also noted that for all systems, the $T = 220$ K and $T = 210$ K isotherms cross higher temperatures isotherms and inflect, showing also a loop for the two highest concentrations, at $T = 210$ K. It has been previously shown in literature [7,18] that the presence of inflections of the isotherms in this region

of the phase diagram can be seen as signals of the approach to liquid-liquid coexistence. The density region in which the inflections appear reduces in width upon increasing concentration. This may indicate that the width of the coexistence envelope reduces, as the concentration increases, with a possible gradual weakening of the anomalous behaviour. Experimentally, a gradual weakening of the apparent divergence of the isobaric specific heat upon increasing the salt content, has been observed [131].

In Fig. 4.4 we can see the isochores $(P - T)$ plane for the four systems studied in the PR-TIP4P set. The isochores are shown for temperatures from $T = 350$ K to $T = 210$ K. A state point at $T = 190$ K is also reported for $c = 2.10$ mol/kg and $\rho = 0.98$ g/cm^3. We can observe minima in the curves, for densities $\rho \geq 0.95$ g/cm^3 in bulk water, $\rho \geq 0.90$ g/cm^3 for $c = 0.67$ mol/kg NaCl(aq), $\rho \geq 0.95$ g/cm^3 for $c = 1.36$ mol/kg NaCl(aq) and $\rho \geq 0.98$ g/cm^3 for $c = 2.10$ mol/kg NaCl(aq). The minima of the isochores are points belonging to the TMD line, as indicated by Eq. 4.4. The points of the LG-LMS line, calculated looking at the minima of the isotherms (see Fig. 4.3) have been also reported in Fig. 4.4 together with the isochores and the TMD points. In all systems the LG-LMS line is located entirely in the region of negative pressures, and non re-entrant behaviour is observed down to the lowest temperature investigated. The isochores lying below the respective LG-LMS line were not reported in Fig. 4.4.

Reproducing the behaviour that we have seen looking at the isotherms in Fig. 4.3, also the high density isochores shift to lower pressures upon increasing concentration. For low densities instead the isochores of the different systems are found at similar pressures. If we look at corresponding isochores, we can see that the range of pressures spanned decreases by about 50 % when one goes from bulk water to $c = 2.10$ mol/kg. In order to better display this behavior of the isochores, in Fig. 4.5 the $\rho = 1.050$ g/cm^3 and the 0.900 g/cm^3 isochores are reported for all systems. We can see that the increase of salt content has the effect of progressively packing the isochores near the LG-LMS line. It has been previously shown in works performed at constant pressure [136, 141, 150, 195], that the effect of ions on the structure of water is analogous to the application of an external pressure. This picture is consistent with our findings, in fact isochores for bulk water coincide with isochores of the solutions at higher and higher density, as the ion concentration increases.

The behaviour of the potential energy as a function of the density, at low temperature was also studied. Fig. 4.6 shows the potential energy at $T = 220$ K calculated for the four systems as a function of the density. We can observe that one minimum can be seen for bulk water and for $c = 0.67$ mol/kg NaCl(aq). Two minima are present for the two highest

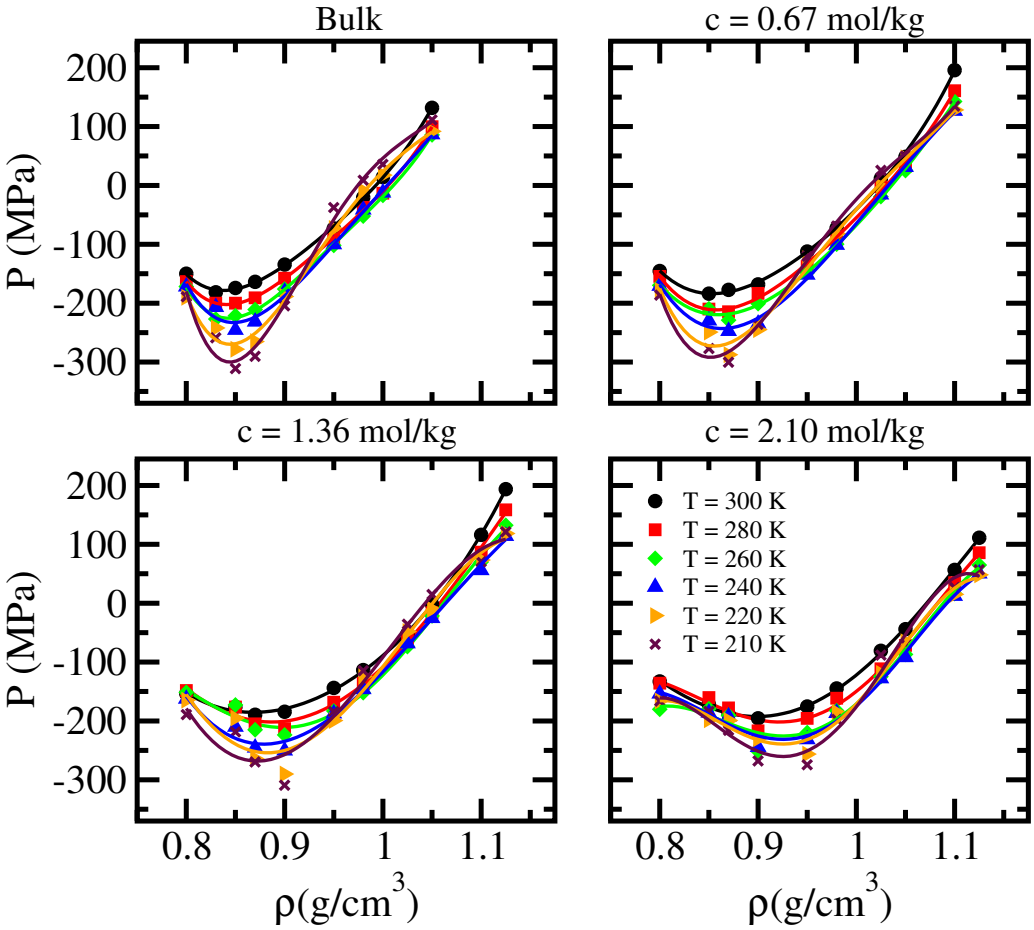

Figure 4.3: Isotherms ($P - \rho$) plane for all the systems in the PR-TIP4P set. The isotherms are reported for temperatures $T = 300, 280, 260, 240, 220, 210$ K. The lines joining the simulated state points have been obtained by polynomial fitting. The lowest density is $\rho = 0.800$ g/cm^3 for all systems while the highest density is $\rho = 1.050$ g/cm^3 for bulk water (top left panel), $\rho = 1.100$ g/cm^3 for $c = 0.67$ mol/kg NaCl(aq) (top right panel), $\rho = 1.125$ g/cm^3 for $c = 1.36$ and 2.10 mol/kg NaCl(aq) (bottom left and bottom right panel respectively).

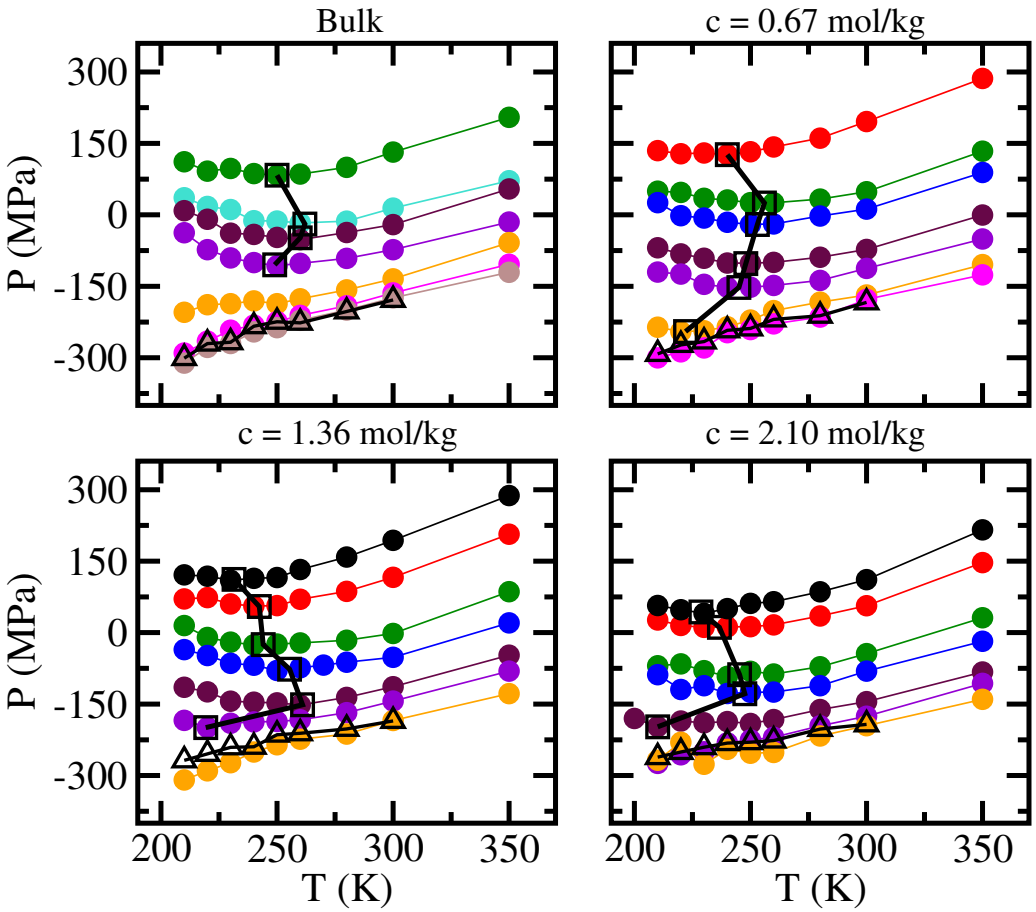

Figure 4.4: Isochores ($P-T$) plane for all the simulated systems in the PR-TIP4P set. Besides isochores, the TMD points (squares) and the LG-LMS points (triangles) are shown. The range of temperatures goes from $T = 210$ K to $T = 350$ K. The values of the densities reported are: $\rho = 1.050, 1.000, 0.980, 0.950, 0.900, 0.870, 0.850$ g/cm^3 for bulk water (top left panel); $\rho = 1.100, 1.050, 1.025, 0.980, 0.950, 0.900, 0.870$ g/cm^3 for $c = 0.67$ mol/kg (top right panel); $\rho = 1.125, 1.100, 1.050, 1.025, 0.980, 0.950, 0.900$ g/cm^3, for $c = 1.36$ mol/kg (bottom left panel) and $c = 2.10$ mol/kg (bottom right panel).

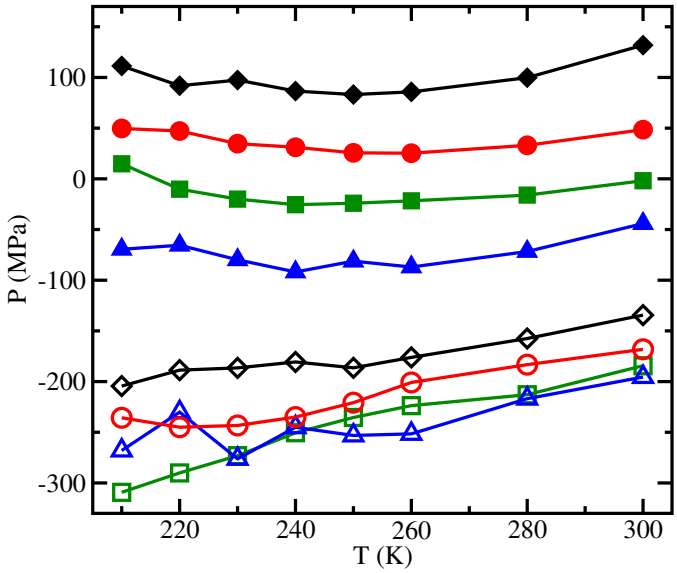

Figure 4.5: Isochores in the temperature range from $T = 210$ K to $T = 300$ K, for bulk water (diamonds), $c = 0.67$ mol/kg (circles), $c = 1.36$ mol/kg (squares) and $c = 2.10$ mol/kg (triangles) NaCl(aq) at densities $\rho = 1.050$ g/cm^3 (filled symbols) and 0.900 g/cm^3 (open symbols).

concentrations, $c = 1.36$ mol/kg NaCl(aq) and $c = 2.10$ mol/kg NaCl(aq). It has been shown by Kumar *et al.* [21] that two minima in the behaviour of the potential energy at $T = 220$ K can be found for water confined between hydrophobic plates.

Now we consider the free energy $F = K + U - TS$, where K is the kinetic energy, U is the potential energy and S is the entropy. At low temperatures the kinetic and the entropic contributions become small and the potential energy can be taken as an estimator of the behaviour of F [21,24]. Therefore in our case the appearance of two minima in the behaviour of the potential energy for the solution at the two highest concentration suggests the possible presence of two stable liquid phases. In bulk water and in $c = 0.67$ g/cm^3 NaCl(aq) only one minimum is present in the spanned range of simulated density, with the other one possibly located at higher density. It can be also noted that upon increasing concentration the the low density minimum moves towards higher densities and the minima become closer to each other. This could indicate that, as the concentration is increased, the difference between the two liquids becomes less relevant and the width of the coexistence envelope becomes smaller.

In Fig. 4.7 the results obtained for the TMD line and the LG-LMS line of bulk water and $c = 0.67, 1.36$ and 2.10 mol/kg NaCl(aq) are shown together.

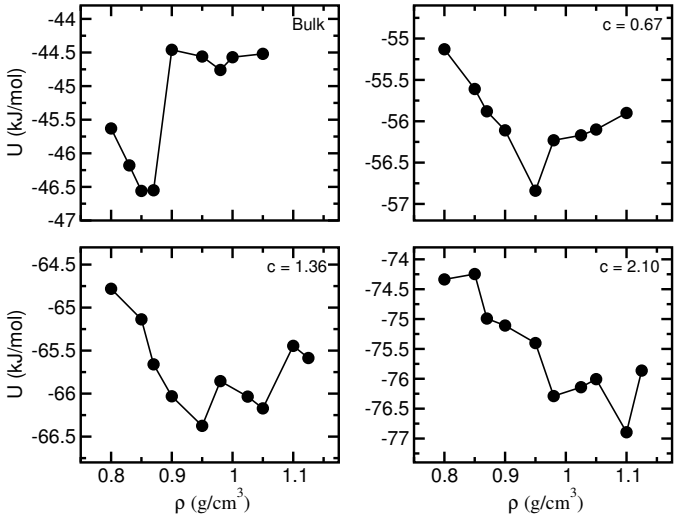

Figure 4.6: Potential energy per molecule as a function of the density of the system, at constant temperature $T = 220$ K, for bulk water (top left panel), $c = 0.67$ mol/kg (top right panel), $c = 1.36$ mol/kg (bottom left panel) and $c = 2.10$ mol/kg (bottom right panel) NaCl(aq).

They are also compared with data for TIP4P water confined in a hydrophobic environment of soft spheres [54]. Further details on this system are given in Sec. 4.4. The lines are schematised from the data presented in Fig. 4.4 and are reported in the range of temperatures from $T = 210$ K to $T = 300$ K.

It can be noted that the LG-LMS line is practically unaltered by the addition of ions. The position and the shape of the LG-LMS line remain quite similar to the case of bulk water, with only a small increase in pressure, at low temperatures for the two highest concentrations. For the hydrophobic confinement, the LG-LMS line is shifted to higher pressures, by circa 200 MPa. This system can be thought as behaving like a solution of small apolar solutes [54] and the shift of the LG-LMS line can be due to large excluded volume effects caused by strong solute-solvent repulsion. Thus in the case of polar solutes, excluded volume effects seem to be less relevant and the LG-LMS line lies at similar pressures with respect to the one of bulk water.

On the TMD line the effect of the ions is more marked. Upon increasing concentration in fact, the TMD line moves to lower temperatures and the upper branch moves also to lower pressures. The amplitude of the TMD curves reduces as the concentration is increased. This seems to indicate that in the solutions, the width of the region in which anomalies are present progressively reduces. In the case of hydrophobic confinement the TMD

moves to lower temperatures but to higher pressures. From this, we can hypothesize that the addition of solutes always shift the TMD line to lower temperatures, while the direction of the pressure shift is determined by the polar or apolar nature of the solute.

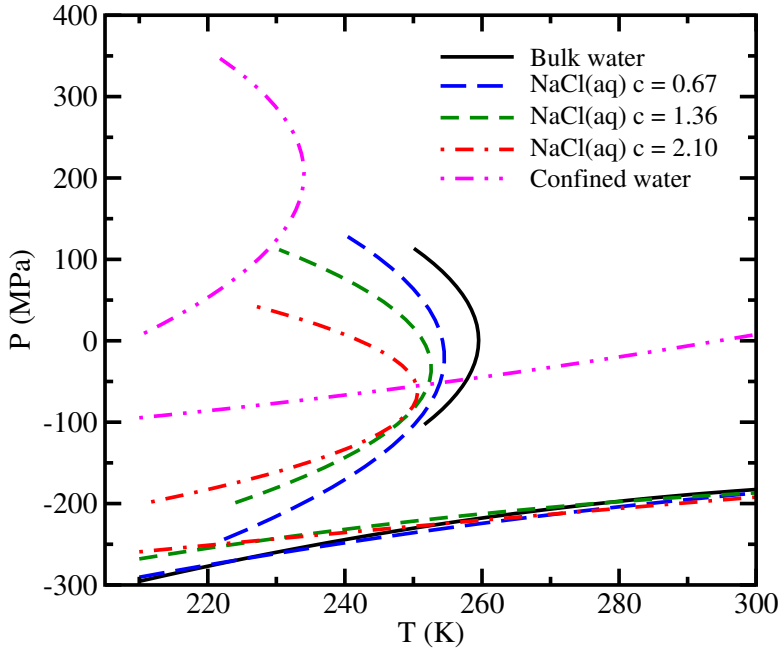

Figure 4.7: TMD and LG-LMS lines for bulk water, for $c = 0.67, 1.36$ and 2.10 mol/kg NaCl(aq) and for water confined in a hydrophobic environment of soft spheres [54].

Summarizing the results obtained in the study of the thermodynamics of the PR-TIP4P set, we can state that indications of the the presence of liquid-liquid coexistence were found in bulk water and in NaCl(aq) up to the highest concentration investigated. In fact looking at the isotherms (Fig. 4.3) we saw that low temperature isotherms show inflections, crossing higher temperature isotherms, in all systems. A progressive reduction in density of the region where these inflections occurs, as the concentration increases is also evident. The apparent reduction of the width of the anomalous region was also found in the potential energy behavior (Fig. 4.6). The minima found in the behaviour of the potential energy as a function of the density, in fact become closer to each other upon increasing the salt content. These minima have been related to the possible coexistence of a high density liquid (HDL) phase and a low density liquid (LDL) phase. Observing the behavior of the isochores (Fig. 4.4) we saw that they pack near the LG-LMS line with

a downward shift in pressure upon increasing concentration. This shift in pressure was also connected to the equivalence of the presence of ions to the application of an external pressure. From the analysis of the isotherms and isochores planes, the LG-LMS and TMD lines were calculated and shown together with the same quantities for water in a hydrophobic confinement (Fig. 4.7). While the LG-LMS line was found to be only very mildly affected by the presence of polar solutes, the TMD line showed a shift to lower temperatures and pressures, with also a narrowing of the amplitude of the curve upon increasing concentration. In the case of the apolar solutes instead the LG-LMS line moves to higher pressures because of excluded volume effects, while the TMD line shifts to higher pressures and lower temperatures.

4.4 Structural results

In this section the structural properties of $c = 1.36$ mol/kg NaCl(aq), as obtained from simulations in the PR-TIP4P set [48], are discussed and compared with structural properties of water in a hydrophobic environment [54]. The intermediate concentration of NaCl was chosen for this study as representative of the behavior of NaCl(aq) solutions, as in the $c = 0.67$ mol/kg and $c = 2.10$ mol/kg the results do not differ significantly. The simulation details for $c = 1.36$ mol/kg NaCl(aq) were given previously (see Sec. 4.1). Let us describe here briefly the system to which we compare, water in a hydrophobic environment, that in the following will be named Hphob. In this system TIP4P water was simulated in a matrix of six soft spheres. The spheres (S) are maintained frozen. The interaction potential between water and spheres is given by

$$V_{OS} = 4\epsilon_{OS}\left(\frac{\sigma_{OS}}{r}\right)^{12} \tag{4.5}$$

where ϵ_{OS} and σ_{OS} were calculated considering the Lorentz-Berthelot mixing rules $\epsilon_{ij} = \sqrt{\epsilon_{ii}\epsilon_{jj}}$ and $\sigma_{ij} = (\sigma_{ii}+\sigma_{jj})/2$. In this case ϵ_{OO} and σ_{OO} are those of TIP4P model (see Sec. 4.1), while $\epsilon_{SS} = 0.1\epsilon_{OO}$ $\sigma_{SS} = 2\sigma_{OO}$. The average distance between two soft spheres is 10.5 Å. The interaction potential was truncated at 9 Å also in this case and long range electrostatic interactions were dealt with the Ewald summation method. For this system, the density of water is calculated assuming that the excluded volume introduced by the confining spheres is approximately $V_{\text{excl}} = \pi N_S \sigma_{OS}^3/6$ so that

$$\rho_w = \frac{N_w}{L^3 - V_{\text{excl}}}\frac{W_w}{N_A} \tag{4.6}$$

where N_w is the number of water molecules, W_w is the molecular weight of water, L is the box length and N_A is the Avogadro number. The range of densities from $\rho = 0.75$ g/cm^3 to $\rho = 1.02$ g/cm^3 was spanned for the Hphob system and temperatures were studied from $T = 210$ K to $T = 350$ K. Further details on the Hphob system are given in Ref. [54].

First let us compare the oxygen-oxygen radial distribution functions (RDFs) in bulk water, NaCl(aq) and Hphob. In order to compare similar densities we consider the $\rho = 1.10$ g/cm^3 for the ionic solution that corresponds to $\rho_w \simeq 1.04$ g/cm^3, to be compared with $\rho_w = 1.00$ g/cm^3 for the Hphob. In Fig. 4.8 the O-O RDFs at $T = 300$ K for the three systems are reported together.

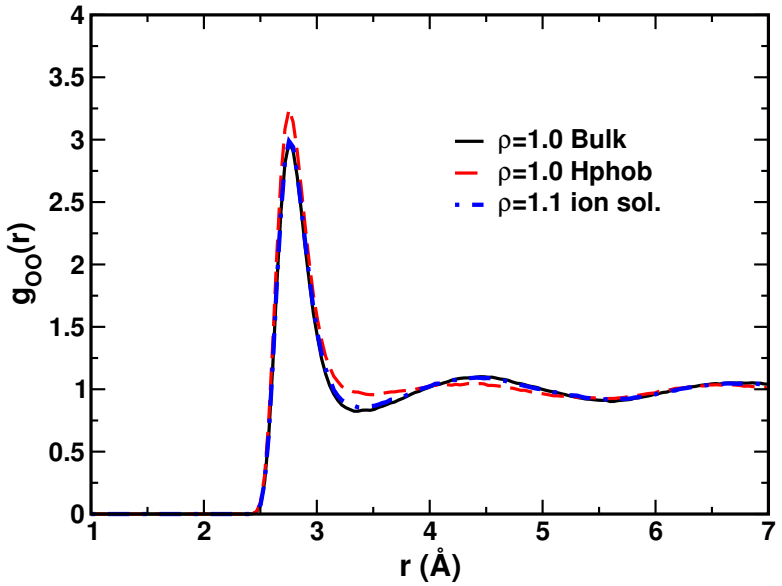

Figure 4.8: Oxygen-oxygen RDFs at $T = 300$ K for bulk water, Hphob and $c = 1.36$ mol/kg NaCl(aq).

It can be observed that in the Hphob the O-O first peak increases. The presence of hydrophobic spheres creates an excluded volume effect that reduces the available volume for the water molecules. Nonetheless water is able to maintain its hydrogen bond network. In the case of NaCl(aq) the effect of the O-O structure is rather negligible, at least for this temperature and density.

We can now compare the water-solute RDFs, $g_{\rm OX}$, where X=Na, X=Cl or X=S. Here with solute we indicate a generic object in water in fact soft spheres are not true solutes because they are immobile. In Fig. 4.9 the $g_{\rm OX}$ at $T = 300$ K are shown alongside with the same quantities rescaled by the

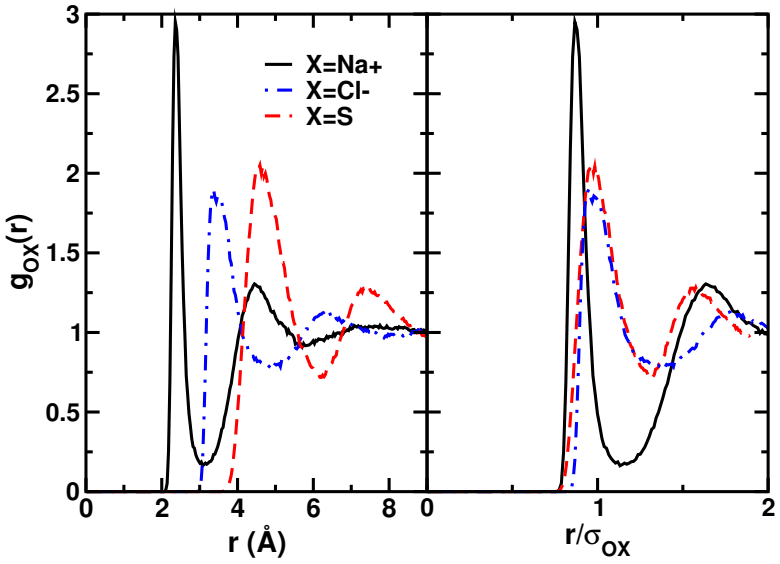

Figure 4.9: (Left panel) Comparison between the g_{ONa} (solid line), g_{OCl} (dot-dashed), g_{OS} (dashed) at $T = 300$ K and at an equivalent water density (see text). (Right panel) Same quantities of left panel rescaled to their respective LJ parameter σ_{OX}.

respective Lennard-Jones (LJ) parameter σ_{OX}. This was done to take into account the fact that the position of the peaks are mostly determined by the interaction length scale. In the case of sodium a well defined shell of oxygen atoms forms around the ion. This is indicated by the sharp first peak and the deep first minimum. The first shell for the chloride is located between the first and second shell of sodium, indicating charge ordering around the oxygen atoms. Water is also able to form hydration cages around soft spheres. In this case the first peak looks broader than in the case of sodium ion and the first minimum is shallow indicating a large exchange between first and second shell. This features are also similar to the case of Cl. However in the region of the second shell the O-Na and the O-S structures look similar. This seems to indicate that the first shell of oxygen atoms around sodium has the effect of screening water-ion electrostatic interactions so that the O-Na second shell is mainly determined by water-water interaction and excluded volume effects. The O-Cl structure is also partially affected by the screening effect, since the shape of the first peak of the g_{OCl} is similar to the hydrophobic case.

In Fig. 4.10 the hydrogen-solute RDFs are shown. We can observe that the interaction between hydrogen and chloride is weaker with respect to oxygen-sodium attraction. The charge ordering of shells is still present but

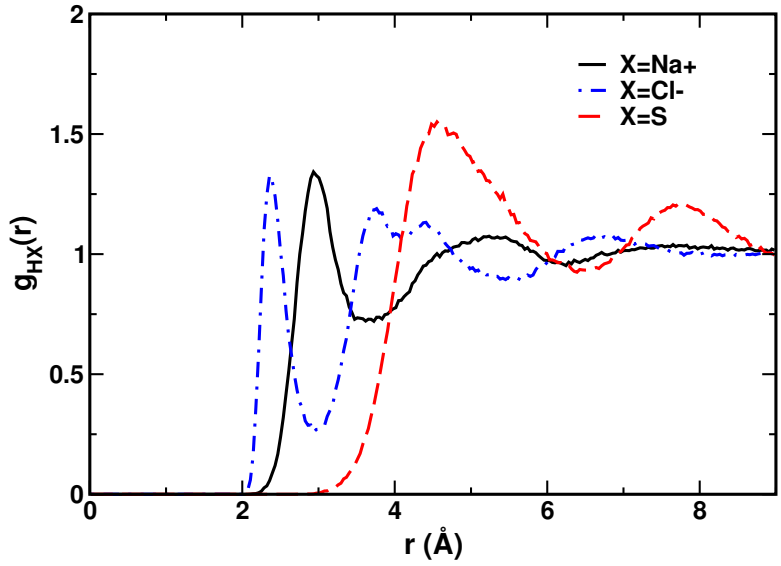

Figure 4.10: Comparison between the g_{HNa} (solid line), g_{HCl} (dot-dashed), g_{HS} (dashed) at the same thermodynamic conditions as in Fig. 4.9.

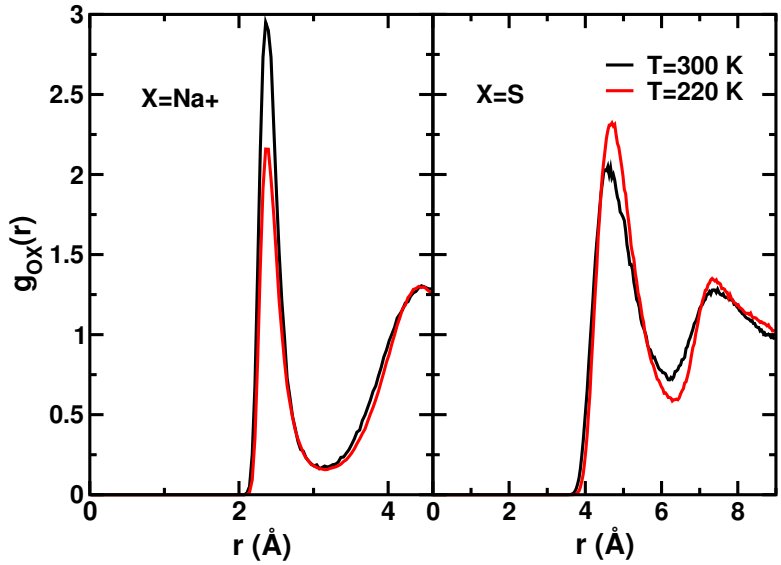

Figure 4.11: (Left panel) g_{ONa} at $T = 300$ K and $T = 220$ K. (Right panel) g_{OS} at $T = 300$ K and $T = 220$ K.

no screening effect takes place since the H-Na shell is sharper than the H-S one. The first H-S peak is located in the same position of the O-S peak and this indicates that the soft spheres are preferentially interstitial in the hydrogen bond network and equidistant between hydrogen and oxygen atoms.

The effect of temperature on the hydration structure is studied in Fig. 4.11 looking at the g_{ONa} and g_{OS} at $T = 300$ K and $T = 220$ K. We can see that the decrease of temperature has a different effect for the two kinds of solutes. In the case of the sodium ion the hydration shell results weakened while in the case of the hydrophobic objects the cages of water molecules seems to become more ordered. These effects might be connected to an increased tendency of water molecules to bond between themselves at low temperatures.

In Fig. 4.12 and 4.13 we investigate the effect of density on the hydration structure at ambient temperature, $T = 300$ K.

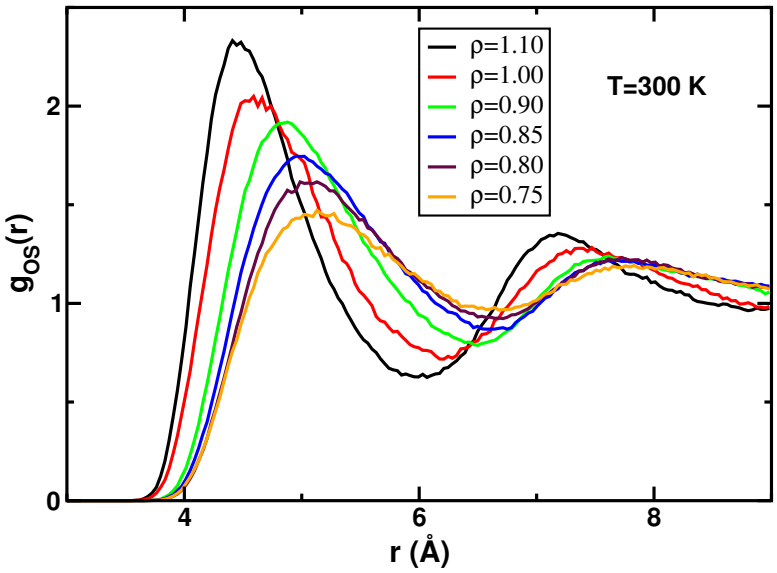

Figure 4.12: g_{OS} at $T = 300$ K, for decreasing densities.

In the Hphob system (Fig. 4.12) the first peak decreases monotonically with decreasing density. This happens consequently to the relaxation of water cages around the spheres when density is decreased and finally approaches the LG-LMS of the system.

For the ionic solution (Fig. 4.13) instead the effect of decreasing density is quite small and qualitatively similar to the decrease of temperature. A minimum in the intensity of the first peak can be seen at $\rho = 0.87$ g/cm^3, close to the LG-LMS line.

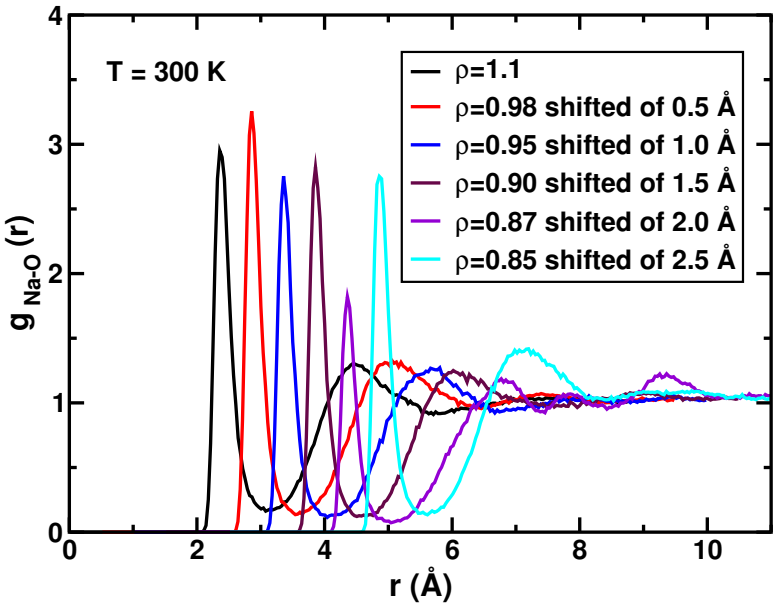

Figure 4.13: g_{ONa} at $T = 300$ K, for decreasing densities. As indicated the g_{ONa} are shifted along r for the sake of clarity.

Now let us investigate if there is a relation between the region of density anomaly and the structural properties of the systems. The TMD lines for the systems taken into account in this context was shown in Fig. 4.7. The TMD line is the locus of the point for which the coefficient of thermal expansion α_P is zero, therefore it separates the region of normal behaviour, where at constant pressure, the density increases upon decreasing temperature, $(\partial V/\partial T)_P > 0$, from the region of density anomaly, where density increases upon heating, $(\partial V/\partial T)_P < 0$. The coefficient of thermal expansion is also related to the fluctuations of volume and entropy by the relation

$$V k_B T \alpha_P = \langle \delta V \cdot \delta S \rangle \quad . \tag{4.7}$$

In bulk water α_P can become negative because at low enough temperatures, the network of tetrahedrally coordinated molecules stabilize, reducing the entropy and at the same time leaving more free volume. In the mixtures we are considering here, we can assume that the behaviour of α_P is mainly due to the solvent component and that δV is the fluctuation of the available volume for water.

In the case of Hphob system, we have seen that water at contact with soft spheres retains its main structural features (see Fig. 4.8). Nonetheless the TMD is shifted by circa 40 K to lower temperatures and by circa 200 MPa to

higher pressures (see Fig. 4.7), being the shape of the line similar to that of bulk water. Thus the hydrophobic interaction does not alter the form of the TMD line but induces a shift to higher pressures and lower temperatures of the region where ordering of water molecules in associated with an increase of free volume.

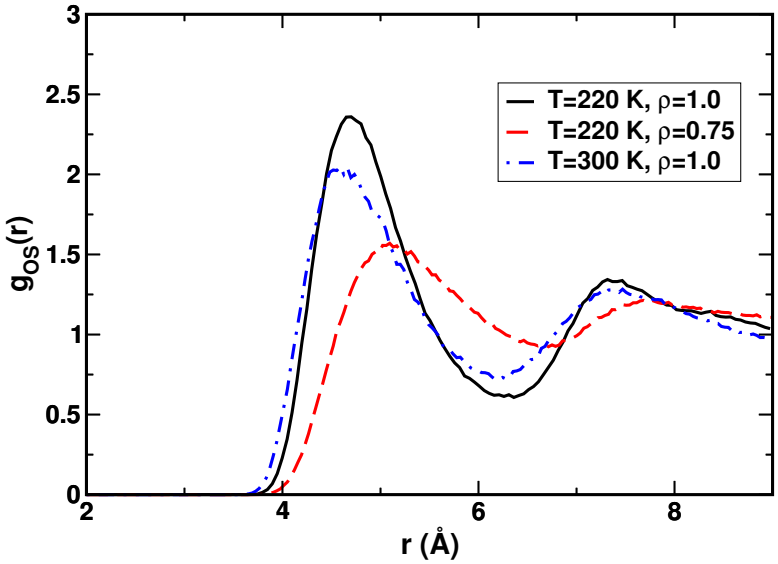

Figure 4.14: g_{OS} for density $\rho_w = 1.00$ g/cm^3 at $T = 300$ K (normal region) and $T = 220$ K (anomalous region). The g_{OS} for $\rho_w = 0.75$ g/cm^3 at $T = 220$ K (normal region) is also reported.

In Fig. 4.14 the g_{OS} for points corresponding to the region of normal and anomalous behaviour are shown. We can observe that in the anomalous region the first shell is more rigid and is well separated from the second shell, with a deeper first minimum. This makes the arrangement of water molecules around spheres more rigid, preserving the open network of water, at least for high enough pressures.

In the case of NaCl(aq), the TMD narrows, thus the presence of ions induces a restriction of the region where ordering is associated with an increase of free volume. Moreover the TMD is also shifted to slightly lower temperatures with respect to bulk water (see Fig. 4.7). Thus it seems that in ionic solutions, the long range electrostatic interactions between ions make more difficult the realization of the ordered open network of water molecules.

In Fig. 4.15 the g_{ONa} for points inside and outside the region of density anomaly are shown. The change in structure is opposite with respect to what we have seen in Fig 4.11, where both the g_{ONa} were in the normal

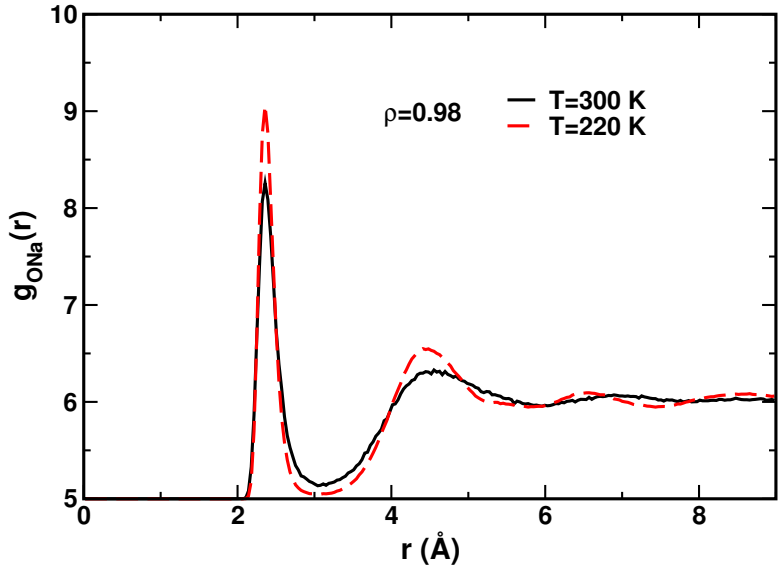

Figure 4.15: g_{ONa} for density $\rho = 0.98$ g/cm^3, at $T = 300$ K (normal region) and $T = 220$ K (anomalous region).

region. Here we see that in the anomalous region the hydration structure becomes more ordered. In this way water is more effective in localizing the ion and screening its charge, so that more free space becomes available for water, at least at low enough temperatures.

In this section we have presented the results of the study of the structural features of $c = 1.36$ mol/kg NaCl(aq) (PR parameters set) compared to those of bulk water and of water confined by soft spheres [54]. We have seen that the polar or apolar nature of the objects modify the structural properties, in particular the hydration structure and its dependence on temperature and density. The presence of solutes and their polar or apolar nature also influences the position and width of the region of density anomaly, where entropy and volume fluctuations are anti-correlated due to the formation of an open hydrogen bonded tetrahedrally coordinated network of water molecules.

Chapter 5

Results for the JJ-TIP4P set

This chapter deals with the results obtained for the simulations in the JJ-TIP4P set. This set consists in the extensive molecular dynamics (MD) simulations performed on TIP4P bulk water and on $c = 0.67$ mol/kg NaCl(aq) [49, 50] with the use of the Jensen-Jorgensen (JJ) parameters. The details of the simulations performed in this set are given in Sec. 5.1. A comparison of the thermodynamic results on NaCl(aq) obtained with the use of the Pettit-Rossky (PR) and JJ parameters is reported in Sec. 5.2. In Sec. 5.3 the thermodynamic results for this set are shown, with particular regard for the finding of the LLCP both in bulk water and in NaCl(aq). Structural results are presented and discussed in Sec. 5.4.

5.1 Simulation details for the JJ-TIP4P set

The JJ-TIP4P set of simulations includes the study of TIP4P bulk water and of $c = 0.67$ mol/kg NaCl(aq) [49,50], performed for an extensive range of thermodynamic points and using the JJ parameters for the ionic potential. The large body of simulated state points was required to fulfill the task of this set of simulations, namely the localization of the liquid-liquid critical point (LLCP) in both bulk TIP4P water and $c = 0.67$ mol/kg NaCl(aq). This project spanned all the three years of the Ph. D. program. During the first one the new set of parameters was checked against the results for PR-TIP4P set and the proposals for the use of large parallel computing machines were conceived. The simulation data were mostly collected during the second year and data analysis was performed between the second and the third year.

The interaction potential between particles is the sum of electrostatic and LJ potential as in Eq. (4.1). The TIP4P model used for solvent molecules

was described in Sec. 4.1. The ionic potential for this set of parameters was taken from Jensen and Jorgensen [53]. This potential was particularly tailored for use with the TIP4P model for solvent molecules. The ion-water parameters were obtained using geometric mixing rules

$$\sigma_{ij} = \sqrt{\sigma_{ii}\sigma_{jj}} \tag{5.1}$$

$$\epsilon_{ij} = \sqrt{\epsilon_{ii}\epsilon_{jj}} \quad . \tag{5.2}$$

The JJ parameters were obtained by Monte Carlo simulation with TIP4P water, reproducing the experimental free energies of hydration and the position of the first peak of the ion-oxygen radial distribution functions (RDFs). No LJ interactions between ions and hydrogen atoms are included in this potential. The JJ ion-water and ion-ion parameters are reported in Table 5.1. The results obtained using PR and JJ parameters are compared in Sec. 5.2.

Table 5.1: JJ ion-water and ion-ion LJ interaction parameters [53].

Atom pair	ϵ_{ij} (kJ/mol)	σ_{ij} (Å)
Na-O	0.036 86	3.583
Cl-O	1.389 57	3.561
Na-Na	0.002 09	4.070
Cl-Cl	2.970 64	4.020
Na-Cl	0.078 79	4.045

The cut-off radius was set to 9 Å and the Ewald summation method was applied to deal with long range electrostatic interactions. The integration time step employed was 1 fs. Temperature was controlled with the Berendsen thermostat [181]. The simulations were performed using the parallel version of the simulation package DL_POLY 2.19 [179].

The total number of particles contained in the simulation box is 256. In the case of the solution $N_{tot} = N_{wat} + N_{Na^+} + N_{Cl^-}$ with $N_{wat} = 250$ and $N_{Na^+} = N_{Cl^-} = 3$. The range of spanned densities goes from $\rho = 0.83$ g/cm^3 to $\rho = 1.10$ g/cm^3, each 0.01 g/cm^3. The densities studied together with the box lengths both for bulk water and for $c = 0.67$ mol/kg NaCl(aq) are shown in Table 5.2. Simulation data were collected each 5 K for temperatures from $T = 350$ K to $T = 190$ K. Initial configurations for each densities were also simulated for $T = 500$ K and $T = 400$ K. The total number of simulated state points, not considering the $T = 500$ K and $T = 400$ K runs, is 1848.

Table 5.2: List of the simulated densities for bulk water and for $c = 0.67$ mol/kg NaCl(aq) in the JJ-TIP4P set with the corresponding box lengths.

	Bulk	NaCl(aq)
ρ (g/cm^3)	L (Å)	L (Å)
1.10	19.097	19.190
1.09	19.155	19.248
1.08	19.214	19.307
1.07	19.274	19.367
1.06	19.334	19.428
1.05	19.396	19.489
1.04	19.458	19.552
1.03	19.520	19.615
1.02	19.584	19.679
1.01	19.648	19.743
1.00	19.714	19.809
0.99	19.780	19.875
0.98	19.847	19.943
0.97	19.915	20.011
0.96	19.984	20.080
0.95	20.054	20.151
0.94	20.124	20.222
0.93	20.196	20.294
0.92	20.270	20.367
0.91	20.343	20.442
0.90	20.418	20.517
0.89	20.494	20.594
0.88	20.572	20.671
0.87	20.650	20.750
0.86	20.730	20.830
0.85	20.811	20.912
0.84	20.893	20.994
0.83	20.977	21.078

As in the case of the PR-TIP4P set the initial configurations were obtained putting the particles on a face centered cubic lattice and melting the crystal at $T = 500$ K. For this set the $T = 500$ K and $T = 400$ K state points were considered equilibration runs and were not retained for data analysis. The final configuration at a given temperature was used as initial configuration for the next (lower) temperature. The length of the equilibration and production times was progressively increased as the temperature was lowered. They vary from values of 0.15 ns at high temperatures to 30 ns for the lowest temperature, considering the sum of equilibration and production times. The equilibration/production times are equal for bulk water and $c = 0.67$ mol/kg NaCl(aq) and for all densities. They are reported in Table 5.3.

The JJ-TIP4P set was demanding in terms of computational effort. In Fig. 5.1 the total simulation time (equilibration run plus production run) is displayed as a function of temperature. It can be noted that 50 ns of simulation time are needed for the two lowest temperatures, $T = 195$ K and $T = 190$ K. This is more than half of the total simulation time for one whole isochore that is about 90 ns. In fact the simulation of low temperatures in MD is extremely demanding in terms of computational time because of the tremendous increase of the relaxation time as supercooling progresses. As 56 isochores (28 for each system) were simulated, the total simulation time amounts to circa 5040 ns. On a single CPU it would take about 55000 hours, more than 6 years of single CPU time. Because of the very long simulation times needed the DL_POLY 2.19 was run in its parallel version. This allowed to reduce the 6 single CPU years to about 1 year of real time, for the execution of the simulations. The simulations of the JJ-TIP4P set were mostly carried out on the CINECA BCX cluster [196] (replaced in the late 2009 by the SP6 cluster [197]), thanks to the grant *Progetto Calcolo 891* that was requested by our group for the execution of these simulations. The remaining simulations were performed on the INFN-Grid Roma Tre cluster [193] and on the HPC cluster [194] of the CNR-IOM *Democritos National Simulation Center* at SISSA, Trieste (Italy), always using the parallel version of DL_POLY 2.19. To assess the parallel scalability of the software, test run were performed on the three clusters. Fig. 5.2 shows the simulation times per day achieved as a function of the number of processors employed, for the three clusters.

We can see that gain in simulation time performed per day, as the number of processors increases, is obtained only up to a certain number of processors, after which an actual loss in simulation time occurs. This is mainly due to the specific architecture of the clusters [193,194,196] and to the MPI libraries for communication between CPUs (in all clusters the OpenMPI [198] libraries

Table 5.3: Simulation times for equilibration (t_E) and production (t_P) runs for bulk water and for $c = 0.67$ mol/kg NaCl(aq) in the JJ-TIP4P set.

T (K)	t_E (ps)	t_P (ps)
350	50	100
345	50	100
340	50	100
335	50	100
330	50	100
325	70	200
320	70	200
315	70	200
310	70	200
305	100	300
300	100	300
295	100	300
290	100	300
285	200	400
280	200	400
275	200	400
270	200	400
265	300	400
260	300	500
255	300	500
250	500	500
245	600	800
240	800	1000
235	1000	1500
230	1000	1500
225	1000	1500
220	1200	2000
215	1200	2000
210	1500	3000
205	2000	4000
200	4000	5000
195	10000	10000
190	15000	15000

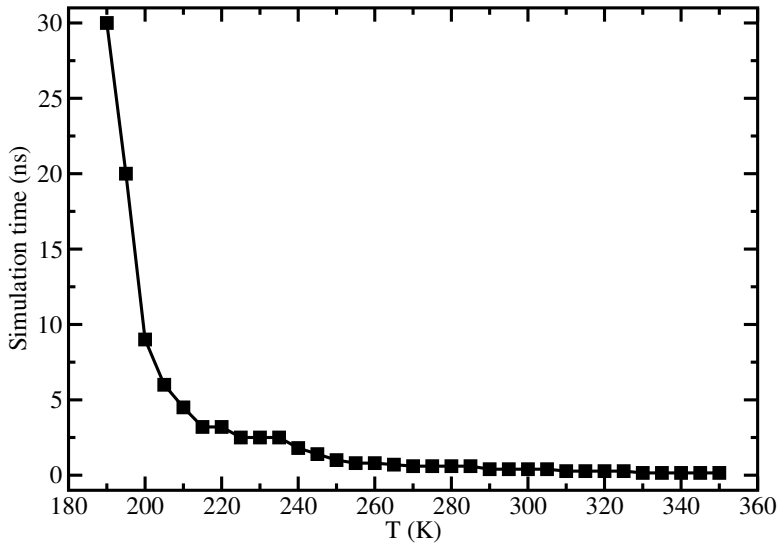

Figure 5.1: Simulation time (equilibration run plus production run) for one isochore in the JJ-TIP4P set as a function of temperature.

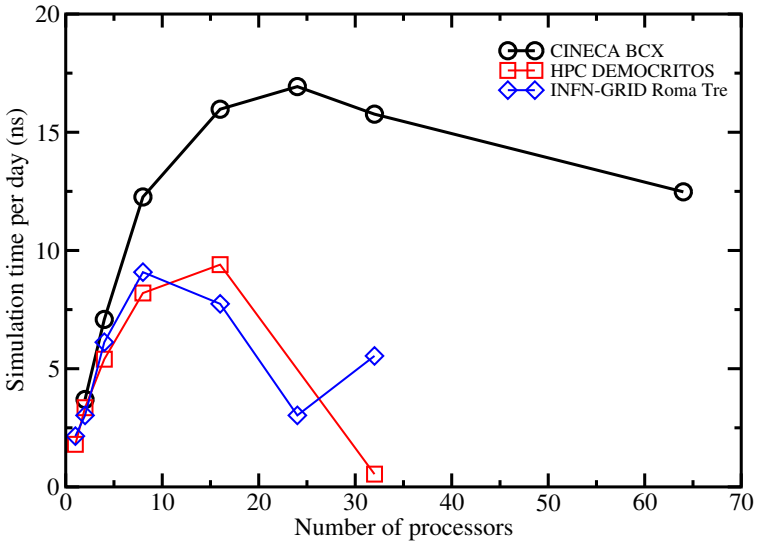

Figure 5.2: Parallel DL_POLY 2.19 simulation times per day as a function of the number of processors used, on the CINECA BCX cluster [196], the DEMOCRITOS HPC cluster [194] and the INFN-GRID Roma Tre cluster [193].

were used). As a consequence, in order to maximize the gain in simulation time and at the same time comply to the queue times allowed by the clusters, 4 or 8 processors were used for all simulations.

5.2 Comparison between the PR and the JJ ion parameters

For the simulations aimed to locate the LLCP, the JJ-TIP4P set, we decided to change the ionic potential, with respect to the PR-TIP4P set. This choice was made because in the PR-TIP4P set a tendency of the ions to cluster together was noted. This effect has already been noted previously in the literature for several ionic potentials [152, 154–156]. The JJ parameters are more balanced in this respect and no clustering was observed. Furthermore the JJ parameters have been originally calculated using the TIP4P model for the solvent molecules [53].

To assess the robustness of thermodynamic data calculated with the two different potentials a comparative study was performed for NaCl(aq) at concentrations $c = 0.67, 1.36$ and 2.10 mol/kg, simulated with the Pettitt-Rossky (PR) and the Jensen-Jorgensen (JJ) parameters. In particular the $\rho = 1.025$ g/cm^3 was simulated using total 256 particles. The PR and JJ ion-water and ion-ion LJ interaction parameters are reported respectively in Table 4.1 and 5.1. It has to be stressed that these two sets of parameters not only differ greatly in their absolute numerical values, but they were also derived with very different approaches. The PR parameters [52] were calculated using an integral equation theory to produce the interatomic potential of mean force at infinite dilution. The JJ parameters [53] were computed through Monte Carlo simulations performed in order to reproduce the experimental values of the free energies of hydration and of the positions of the first peak of the ion-oxygen RDFs. Furthermore, in the PR parameters the interaction between ions and the hydrogen atoms is included in order to balance Cl-H interactions [152], while in the JJ parameters this interaction does not take place.

In Fig. 5.3 the results for the $\rho = 1.025$ g/cm^3 isochore for $c = 0.67, 1.36$ and 2.10 mol/kg, simulated with the PR and JJ parameters are shown. At $c = 0.67$ mol/kg the two isochores remain very similar for all temperatures. As the concentration of ions is increased only minor differences appear. At $c = 1.36$ mol/kg, the $T = 220$ K and the $T = 210$ K points lie at slightly lower pressures for the JJ parameters. At $c = 2.10$ mol/kg, the minimum of the isochore simulated with JJ parameters results deeper than the one

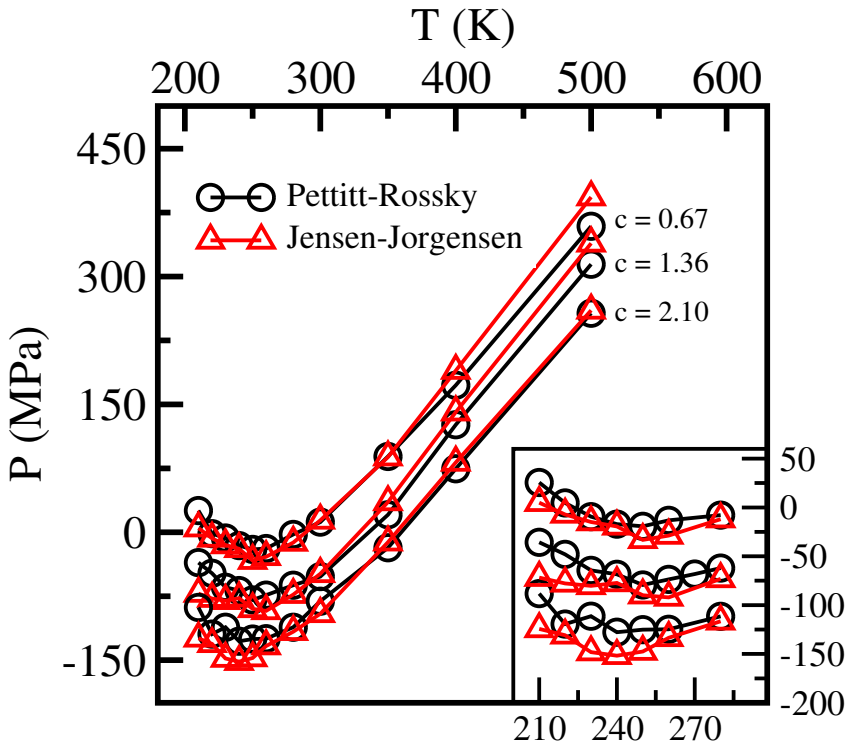

Figure 5.3: Comparison of the $\rho = 1.025$ g/cm^3 isochore of the NaCl(aq) system at concentrations $c = 0.67, 1.36$ and 2.10 mol/kg, simulated employing the PR [52] and the JJ [53] parameters. In the inset a blow up of the low temperature region is shown.

simulated with PR parameters, with low temperatures points also falling to slightly lower pressures. Although some small differences are present, it can be noted that the overall shape and position of the curves remain fairly similar in both cases. Therefore we see that thermodynamics seems to be not much affected by the details of the LJ ionic potential. This could be due to the fact that thermodynamics is mainly determined by long range electrostatic interactions, while structural properties such as ion clustering depend on the details of the short range LJ potential in a stronger way. From the comparison of the $\rho = 1.025$ g/cm^3 isochores calculated with the PR and with the JJ parameters, we can conclude that as far as thermodynamics is concerned, both PR and JJ produce consistent results.

5.3 Thermodynamic results

The main aim of the study of the JJ-TIP4P set was the determination of the location of the LLCP both in bulk water and in $c = 0.67$ mol/kg NaCl(aq). Furthermore the comparison with available experimental data allowed the discussion of the possibility of detecting the LLCP in the aqueous solution. This particular concentration of salt was chosen because it is high enough to show deviations from pure water behaviour but not so high to destroy the anomalous behaviour of water [43, 45, 47, 131]. To have an idea of salt concentrations in the natural environment, sea water concentration is $c \sim 0.55$ mol/kg, while physiological concentration is $c \sim 0.15$ mol/kg. As we mentioned in Sec. 4.1, the TIP4P water potential has been in the past extensively used for the study of water at low temperature and it can reproduce successfully the phase diagrams of all the stable ice phases of water [189]. Previously, for the position of the LLCP in TIP4P bulk water, limits were estimated by MD simulations, namely $T < 200$ K and $P > 70$ MPa [24]. However, no clear determination of its position was available so far.

In the analysis of the simulation data, the points of the temperature of maximum density (TMD) line have been determined from the minima of the isochores. The points of the liquid-gas limit of mechanical stability (LG-LMS) and the liquid-liquid limit of mechanical stability (LL-LMS) have been determined looking at the points where $(\partial P/\partial \rho)_T = 0$. The highest temperature point of convergence of the isochores in the $P - T$ plane was considered to estimate the position of the LLCP [12, 20]. This point is also the upper bound of the LL-LMS line. Other indications signaling the position of the LLCP were the development of a flat region in the isotherms plane and the convergence of the lines of maxima of the isothermal compressibility K_T and the constant volume specific heat C_V. In fact, the presence of a critical point induces large fluctuation in the thermodynamic quantities in the region around it. Consequently above the critical temperature the thermodynamic response functions show loci of extrema, all converging onto the Widom line at the critical temperature [14].

Fig. 5.4 shows the isochores for bulk TIP4P water, from $\rho = 0.90$ g/cm^3 to $\rho = 1.10$ g/cm^3, for temperatures from $T = 210$ K to $T = 350$ K. Along with isochores in the same figure are presented the position of the LLCP, the TMD line, the points of the LG-LMS line and the lines of extrema of the isothermal compressibility K_T and of the constant volume specific heat C_V. The position of the LLCP for TIP4P bulk water has been located at $T = 190$ K, $P = 150$ MPa and $\rho = 1.06$ g/cm^3.

Potentials for water often display phase diagrams similar to that of ex-

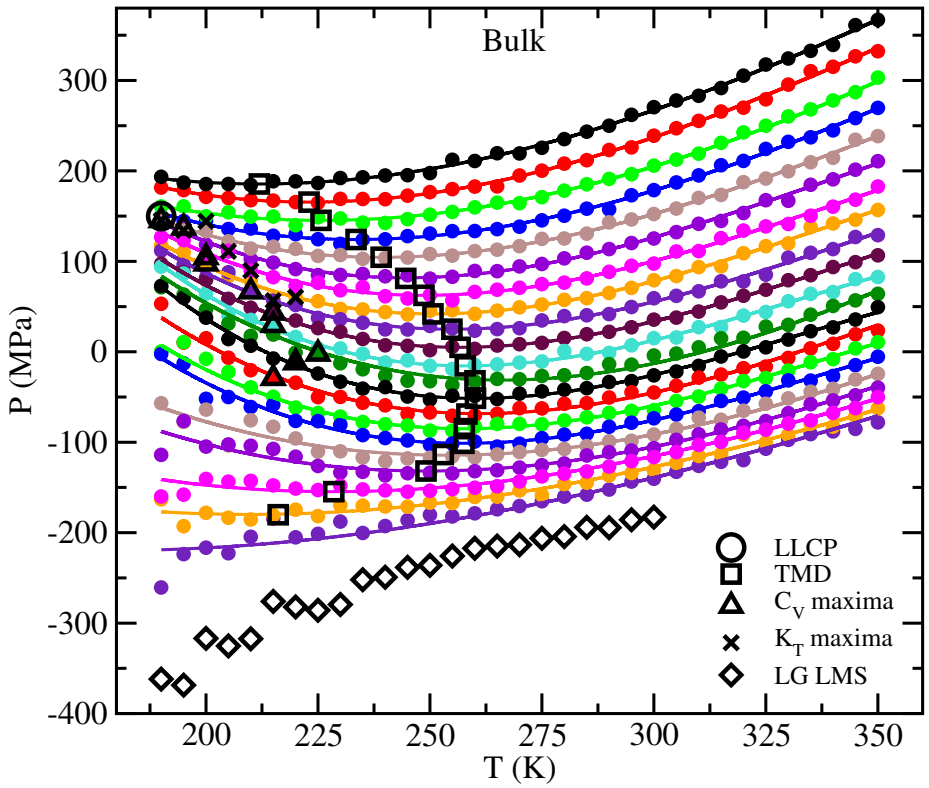

Figure 5.4: Isochores in the $P-T$ plane of bulk TIP4P water, as obtained from MD simulations. The maxima of K_T (crosses) and C_V (triangles) converge to the LLCP. The points of the TMD line (squares) and of the LG-LMS (diamonds) are also shown. Densities are plotted from $\rho = 1.10$ g/cm^3 to $\rho = 0.90$ g/cm^3, with $\Delta\rho = 0.01$ g/cm^3 (from top to bottom) . The lines are polynomial fits to the simulated state points.

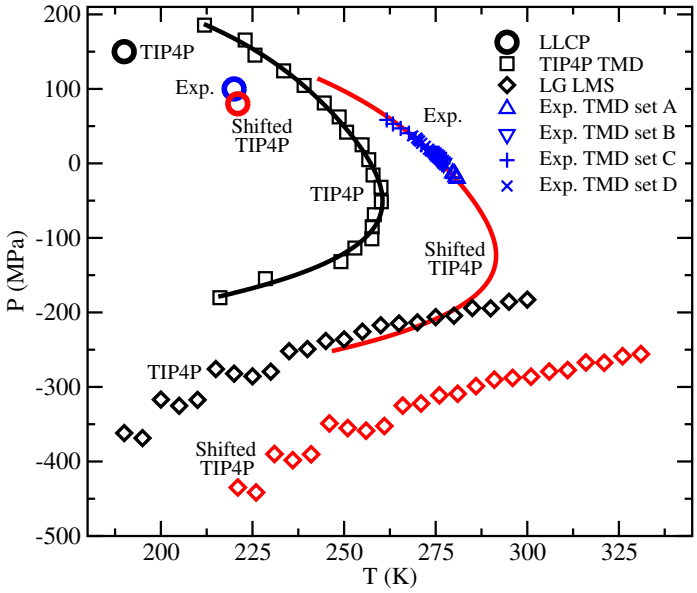

Figure 5.5: LLCP, TMD and LG-LMS line for bulk TIP4P water, as obtained from MD simulations and the same quantities shifted to match experimental values. The match is obtained with a shift of $\Delta T = +31$ K and $\Delta P = -73$ MPa. Sources of experimental values are: for the LLCP Ref. [31] for the TMD line, set A Ref. [199], set B Ref. [200], set C Ref. [29], set D Ref. [201].

perimental water but shifted in temperature and/or pressure. The phase diagram shown in Fig. 5.4 has been compared with available experimental data in order to estimate the magnitude of the shift of the computed quantities, with respect to the experimental water, due to the use of the TIP4P model, in this region. Experimental data for the LLCP were taken from Mishima and Stanley [31], while data for the TMD points were taken from several sources [29, 199–201]. In Fig. 5.5 we present the LLCP, the TMD and the LG-LMS as obtained from MD simulations together with the experimental values for the TMD line and the LLCP. Comparing the bulk TIP4P TMD with the experimental one, we can note that if we apply a shift of $\Delta T = +31$ K and $\Delta P = -73$ MPa the TIP4P TMD exactly superimposes to the experimental values and the LLCP falls very close to the position hypothesized experimentally. This shift needed to superpose the TIP4P data to the experimental is consistent with what found for ice phases

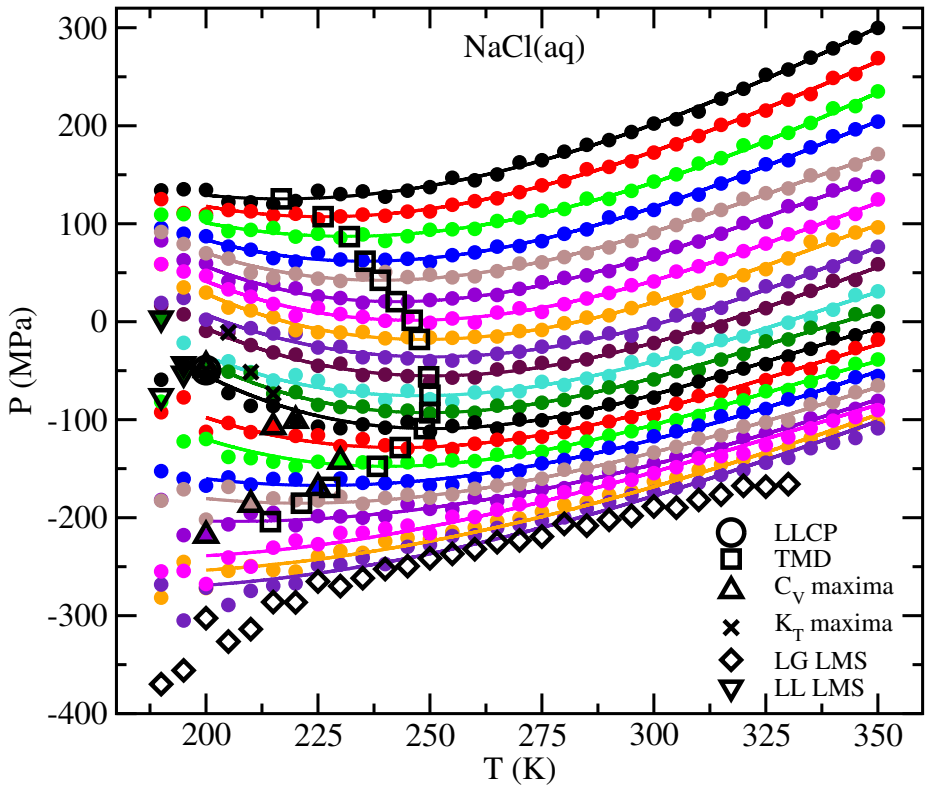

Figure 5.6: Isochores in the $P-T$ plane of $c = 0.67$ mol/kg NaCl(aq), as obtained from MD simulations. The maxima of K_T (crosses) and C_V (triangles up) converge to the LLCP. The points of the TMD line (squares) and of the LG-LMS (diamonds) and LL-LMS (triangles down) are also shown. Densities are plotted from $\rho = 1.10$ g/cm^3 to $\rho = 0.90$ g/cm^3, with $\Delta\rho = 0.01$ g/cm^3 (from top to bottom). The lines are polynomial fits to the simulated state points.

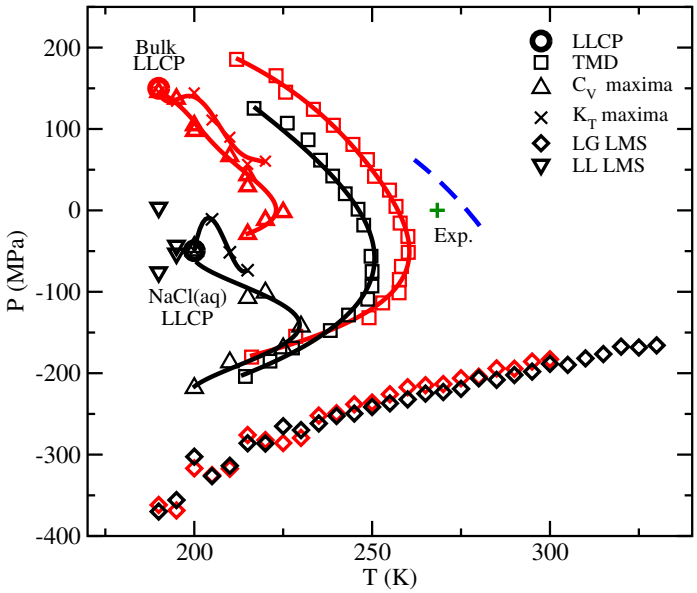

Figure 5.7: LLCP and thermodynamic loci for bulk water (light lines and symbols) and for $c = 0.67$ mol/kg NaCl(aq) (dark lines and symbols) as obtained from MD simulations. The lines are intended as guides for the eye. In this figure are also reported the experimental TMD of bulk water, fitted from data shown in Fig. 5.5, and an extrapolated TMD point at $P = 0.1$ MPa of the solution [131].

of TIP4P [189].

It can be also noted that the turning point of the shifted TMD line is located at about $T = 290$ K and $P = -120$ MPa. As experiments on stretched bulk water have reached very high negative pressures $P = -200$ MPa, the turning point would be in an experimental accessible region, above the melting temperature line [202].

Fig. 5.6 is the analogous of Fig. 5.4 for $c = 0.67$ mol/kg NaCl(aq). Together with the isochores, the estimated position of the LLCP, the TMD points, the lines of extrema of thermodynamic response functions and the LL and LG-LMS points are reported. We can observe that for the same set of densities, the isochores of the solution globally shift to lower pressures with respect to bulk water and they tend to pack near the LG-LMS line, as it has been already pointed out studying the PR-TIP4P set (see Sec. 4.3).

The position of the LLCP in NaCl(aq) was estimated to be $T = 200$ K,

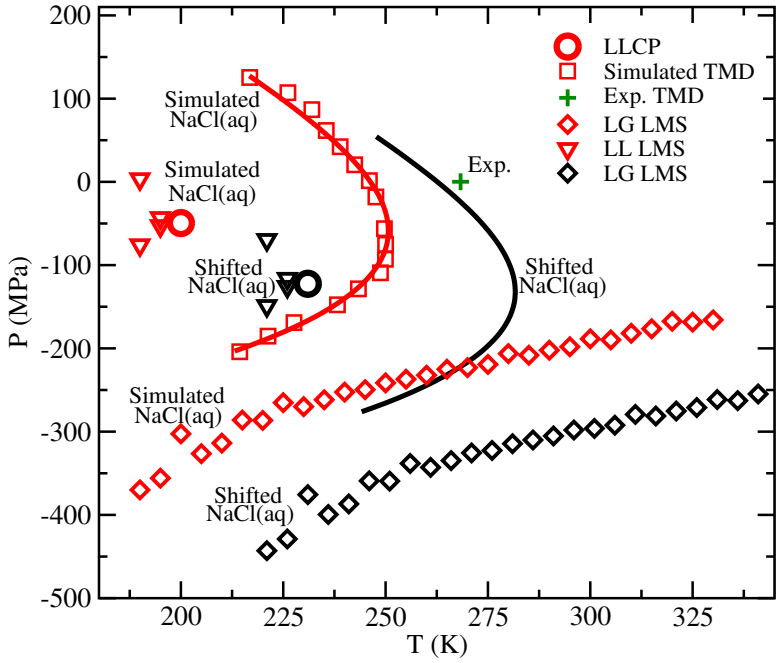

Figure 5.8: LLCP, TMD, LG-LMS and LL-LMS lines for $c = 0.67$ mol/kg NaCl(aq), as obtained from MD simulations and the same quantities shifted of the same amount proposed for bulk TIP4P water (see Fig. 5.5), $\Delta T = +31$ K and $\Delta P = -73$ MPa. The experimental TMD point at ambient temperature is extrapolated from Ref. [131].

$P = -50$ MPa and $\rho = 0.99$ g/cm^3. In the solution it was also possible to reach equilibrium for temperature low enough to determine part of the two branches of the LL-LMS line.

The results obtained directly from MD simulations, for bulk water and for NaCl(aq) are compared in Fig. 5.7. In the same figure, the data are compared with the experimental TMD line of bulk water, determined fitting the data shown in Fig. 5.5 and a TMD point of the solution, extrapolated for our concentration at $P = 0.1$ MPa from available experimental data [131]. We can notice that the lines of extrema of K_T and C_V both in the bulk and in NaCl(aq) merge onto the Widom line very close to the the critical point. The position of the LG-LMS is not altered in the solution with respect to bulk water. The TMD line of the solution instead is shifted by 10 K to lower temperatures and by circa 20 MPa to lower pressures. The same temperature shift is found between the experimental TMD of bulk water and the TMD point of the solution, at ambient pressure.

This result is important because it shows that TIP4P water model is not only able to capture the direction but also the magnitude of the shift found in

experiments. Furthermore we can infer that the experimental shift between bulk water and the solution will be the same found between bulk TIP4P water and TIP4P water in solution. In the solution the LLCP moves of 10 K to higher temperatures and of 200 MPa to lower pressures. This indicates the ions stabilize the high density liquid (HDL) phase, shrinking the region of existence of low density liquid (LDL) phase. This fact is consistent with the observation that ions are more favorably solvated in the HDL phase [133, 134]. As a consequence the region of existence of the phase possessing a local structure with less empty spaces [11] is extended.

Looking at Fig. 5.5 we observed that TIP4P phase diagram results shifted by about $\Delta T \simeq -30$ K and $\Delta P \simeq +70$ MPa with respect to experimental data. From the considerations we did above for the comparison with the experimental TMD line, we can hypothesize that the same shift is preserved in the solution. The LLCP, the TMD and the LG-LMS and LL-LMS points for $c = 0.67$ mol/kg NaCl(aq) obtained directly from MD simulations are reported in Fig. 5.8, along with the same quantities shifted of the same amount of bulk water. We can notice that the experimental TMD point is positioned very close to the TMD line shifted from MD simulation data. The predicted values for the experimental value of the LLCP for $c = 0.67$ mol/kg NaCl(aq) are $T_c \simeq 230$ K and $P_c = -120$ MPa. This large negative pressure can be reached in experiments. In fact it has been found that in $c = 1.00$ mol/kg NaCl(aq) rupture occurs at $P = -140$ MPa [203].

To summarize the results of the investigation of the LL phase diagrams of bulk water and $c = 0.67$ mol/kg NaCl(aq) we report in Fig. 5.9 a schemati-

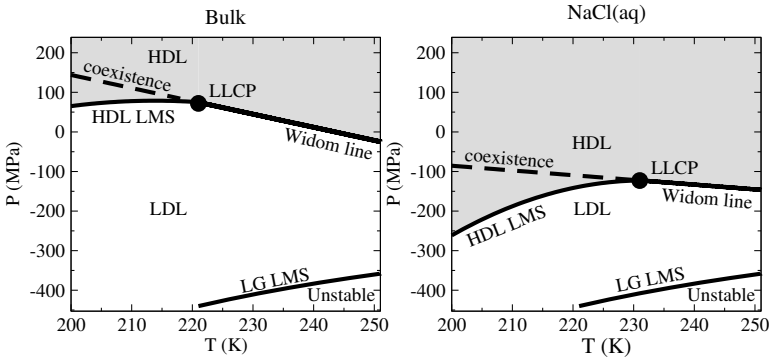

Figure 5.9: Schematisation of the HDL-LDL phase diagrams obtained from MD simulations for bulk water (left panel) and $c = 0.67$ mol/kg NaCl(aq) (right panel) after the application of the shift needed to match experimental values. The position of the LLCP is $T_c \simeq 220$ K and $P \simeq 100$ MPa for bulk water and $T_c \simeq 230$ K and $P \simeq -120$ MPa for NaCl(aq).

sation of the phase diagrams obtained applying the shift proposed to match available experimental data. We propose that these should be the phase diagrams of bulk water and $c = 0.67$ mol/kg NaCl(aq) as measurable in experiments. In this figure it is also evident the magnitude of the restriction of the LDL region in the aqueous solution. Extrapolating the available data at ambient pressure for different concentrations of NaCl [41] it can be estimated that the homogeneous nucleation line for our concentration should be shifted by circa 5 K towards lower temperatures with respect to bulk water (for comparison see Fig. 1 in Ref. [68]). Therefore in the NaCl(aq) the LLCP should fall within the experimentally accessible region. Hence we propose as a viable method to give a definitive experimental answer to the matter of the existence of the LLCP, the study of aqueous solutions of salts.

In a recent experiment on LiCl(aq) solution, the supercooled temperature of $T = 200$ K was reached and the existence of a dynamic transition from fragile to strong behavior was found [204]. This dynamic transition is typical of glass formers and in water it seems to be connected to the Widom line [13, 92, 98] and thus to the possible existence of a LLCP.

Let us recall here the main results obtained from the study of the JJ-TIP4P set aimed to the determination of the LLCP in bulk water and in the NaCl(aq). TIP4P bulk water and a $c = 0.67$ mol/kg solution of NaCl in TIP4P water were simulated in an extensive range of densities and temperatures that allowed the determination of the LLCP of both systems. The TIP4P phase diagram was compared to available experimental data and it was found that upon applying a rigid shift in temperature and pressure the phase diagram calculated in MD can be superimposed to available experimental data. The LLCP of bulk water in the shifted phase diagram falls at $T = 221$ K and $P = 77$ MPa, close to the values hypothesized by Mishima and Stanley [31], $T \simeq 220$ K and $P \simeq 100$ MPa.

The same shift, applied to the phase diagram of NaCl(aq), led to the prediction of an experimentally measurable LLCP in the solution located at $T \simeq 230$ K and $P \simeq -120$ MPa. Upon comparing the phase diagrams for bulk water and NaCl(aq) it can be noted that the ions seems to stabilize the HDL phase with a consequent reduction of the region of existence of the LDL in the solution.

It has been proposed the the existence of the LLCP is connected to a double well effective potential between water molecules [11]. For low enough temperatures the system is driven to condense in the LDL phase by the outer and deep subwell while the transition to the HDL phase is forced by the inner subwell at high enough pressures. In this framework our results indicate that the effect of the ions is to shift the inner subwell to higher distances so that the HDL becomes stable at lower pressures, with respect

to bulk water. Consequently also the TMD line moves closer to the LLCP. As the LG-LMS line is not affected in the solution, the outer subwell seems not to be affected by the ions. In conclusion, with this study we propose the investigation of aqueous solution of salts as a viable and valuable route the inquire experimentally the LLCP of water.

5.4 Structural results

In this section we present the results obtained from the study of the structure of HDL and LDL liquids both in bulk water and in $c = 0.67$ mol/kg NaCl(aq), simulated in the JJ-TIP4P set [50]. We show here again for convenience, in Fig. 5.10, a graph that summarizes the main results we obtained studying the thermodynamics, already reported in Sec. 5.3. In this figure we can see the values obtained from the MD simulations relative to the position of the LLCP, the Widom line, the TMD line and the LG-LMS line both for bulk water and for $c = 0.67$ mol/kg NaCl(aq).

We have seen from the comparison of the phase diagrams for the two systems that the main effect of the presence of the ions seems to be the shrinkage of the region of existence of the LDL phase. This result is consistent with an observed apparent increased solubility of ions in the HDL phase [133, 134].

A thermodynamic quantity directly related to the structural arrangement of the particles is the potential (or configurational) energy. In particular as previously pointed out [24, 29] one can look at the curvature of the configurational part of the Helmholtz free energy $F = U - TS$, where U is the potential energy and S is the configurational entropy. The second derivative of the Helmholtz free energy with respect to the volume is

$$\left(\frac{\partial^2 F}{\partial V^2}\right)_T = \left(\frac{\partial^2 U}{\partial V^2}\right)_T - T\left(\frac{\partial^2 S}{\partial V^2}\right)_T \quad . \tag{5.3}$$

Since the pressure is given by $P = -(\partial F/\partial V)_T$, the curvature of the free energy is related to the isothermal compressibility by the relation

$$\frac{1}{K_T} = V\left[\left(\frac{\partial^2 U}{\partial V^2}\right)_T - T\left(\frac{\partial^2 S}{\partial V^2}\right)_T\right] = V\left(\frac{\partial^2 F}{\partial V^2}\right)_T \tag{5.4}$$

Therefore the curvature of F must be positive in the region of existence of a homogeneous phase. When the curvature of U is negative, the system can be stable for the contribution of a dominant entropic term in Eq.(5.3). However at low temperatures, the stabilization induced by the entropic term can be less effective as the factor T in front of the second derivative of the

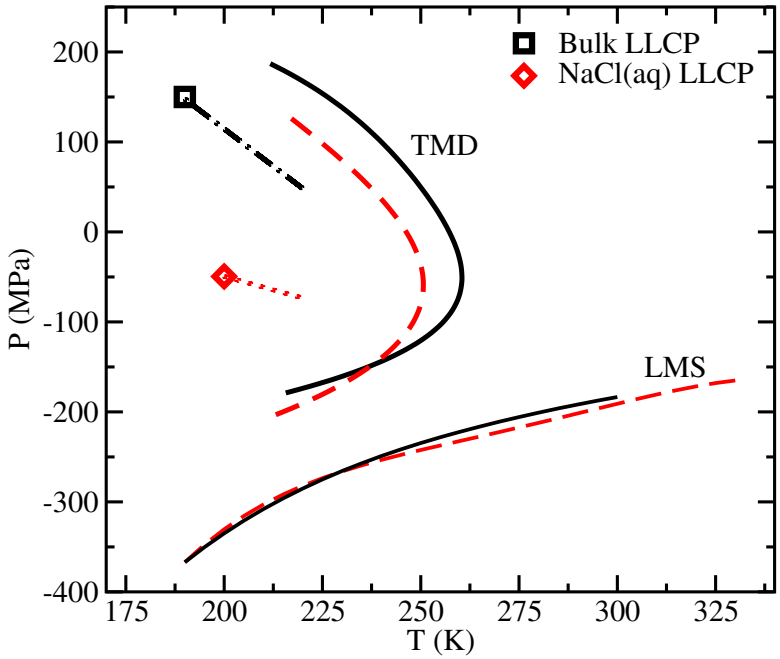

Figure 5.10: Comparison of the main thermodynamic features of bulk water and $c = 0.67$ mol/kg NaCl(aq), as obtained from simulations in the JJ-TIP4P set. The lines are a schematisation of the results shown in Sec. 5.3. In this figure are shown the position of the LLCP in the two systems, the Widom line for bulk water (dot-dashed line) and for NaCl(aq) (dotted line), the TMD and the LG-LMS lines for bulk water (solid lines) and for NaCl(aq) (dashed lines).

entropy in Eq. (5.3) becomes smaller. Thus at low temperatures, the range of volume for which $(\partial^2 U/\partial V^2)_T < 0$ corresponds to a region of reduced stability for the homogeneous phase and eventually the separation in two distinct phases can occur [24].

For bulk water, we calculated the curvature of F from the isothermal compressibility, through Eq. (5.4). This has to be considered a rough estimate because the data on the isothermal compressibility are affected by large fluctuations especially in the region close to the LLCP. We also calculated directly the curvature of the potential energy $(\partial^2 U/\partial V^2)_T$ from our simulation data. Thus by difference we obtained the entropic term $-T(\partial^2 S/\partial V^2)_T$ in Eq. (5.3). We show in Fig. 5.11(a) the potential term $(\partial^2 U/\partial V^2)_T$ and the entropic term $-T(\partial^2 S/\partial V^2)_T$ for bulk water at three temperatures $T = 300$ K, $T = 245$ K and $T = 190$ K. At the same three temperatures, we show in Fig. 5.11(b), the curvature of F obtained considering the inverse compressibility, in Eq. (5.4). We can see that the interplay of the potential energy term and of the entropic term is such that the stability

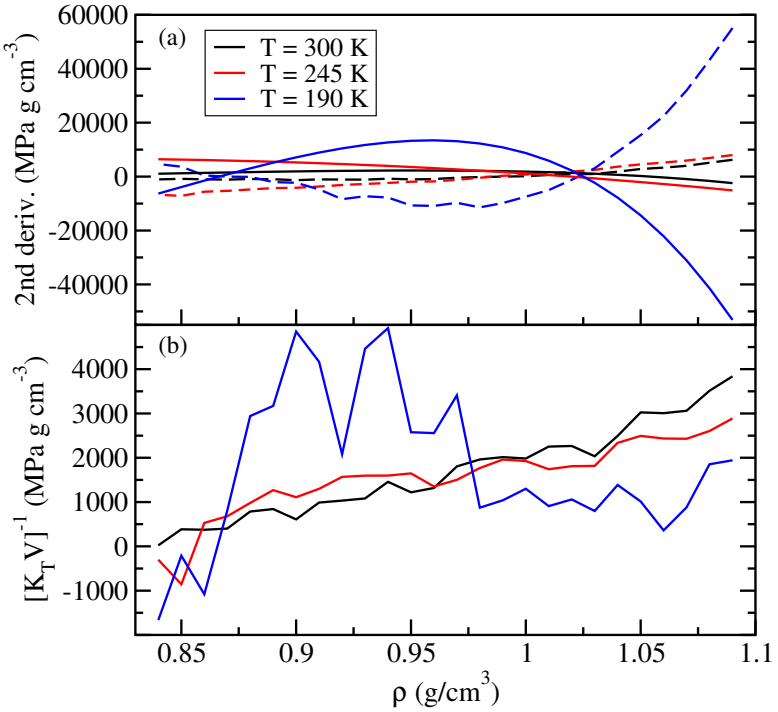

Figure 5.11: (a) Potential energy term $(\partial^2 U/\partial V^2)_T$ (solid lines) and entropic term $-T(\partial^2 S/\partial V^2)_T$ (dashed lines) of the second derivative of the free energy with respect to volume, see Eq. (5.3), for bulk water at temperatures $T = 300$ K, $T = 245$ K and $T = 190$ K. (b) Curvature of the free energy for bulk water at temperatures $T = 300$ K, $T = 245$ K and $T = 190$ K, as obtained considering $(K_T V)^{-1} = (\partial^2 F/\partial V^2)_T$.

of the system, measured through the isothermal compressibility, increases upon decreasing temperature for densities in the range that goes from the LG-LMS density up to $0.96 - 0.98$ g/cm^3. Conversely at higher densities, the stability of the system reduces upon decreasing temperature and consistently it approaches zero (thus infinite compressibility) at $T = 190$ K, for the density corresponding to the LLCP, $\rho = 1.06$ g/cm^3. We can also see that for densities higher than the LG-LMS, the temperature behaviour of the inverse compressibility qualitatively follows the one of the potential term and that at high densities, the curvature of the potential energy drives the system to the reduced stability, since it becomes more and more negative upon decreasing temperature, making the entropic term progressively less effective in stabilizing the system. The same analysis performed on NaCl(aq) (not shown) produces similar results.

We now look at the behaviour of the potential energy of bulk water and $c = 0.67$ mol/kg NaCl(aq) in the JJ-TIP4P at different temperatures.

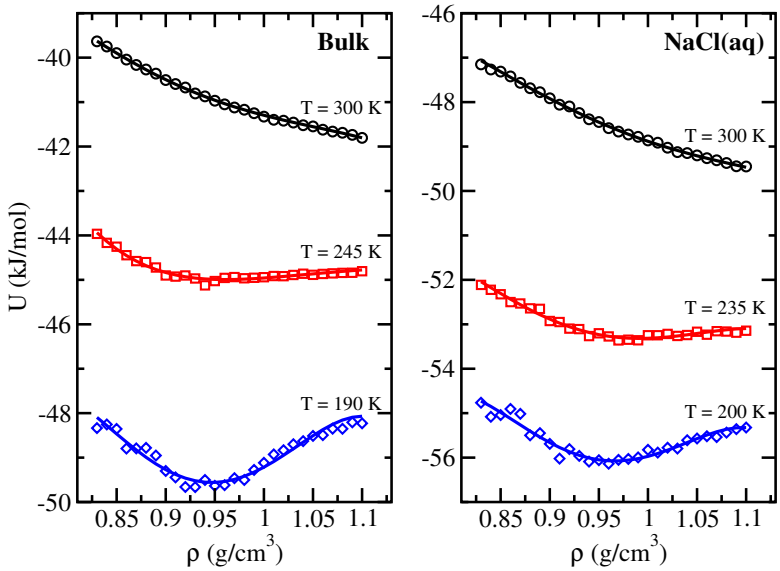

Figure 5.12: Potential energy per molecule as a function of the density, at constant temperature. (Left panel) isotherms of the potential energy of bulk water for temperatures $T = 300$ K, $T = 245$ K and $T = 190$ K. (Right panel) isotherms of the potential energy of NaCl(aq) for temperatures $T = 300$ K, $T = 235$ K and $T = 200$ K.

The results are shown in Fig. 5.12. The behavior of the potential energy is reported for three temperatures, namely ambient temperature, $T = 300$ K, the first temperature showing a negative curvature of U, $T = 245$ K for bulk water and $T = 235$ K for NaCl(aq) and for the temperature corresponding to the LLCP, $T = 190$ K for bulk water and $T = 200$ K for NaCl(aq). For both systems, at ambient temperature, U is a positively curved function of density and it decreases monotonically (becomes more negative) as density is increased. Upon decreasing temperature a minimum in the behaviour of U begins to form and a negative curvature at high densities appear. As we have seen in Fig. 5.11, the stability of the system tends to be reduced in the region where the potential energy shows a negative curvature.

The presence of the minimum in the potential energy has been previously connected to the presence of a tetrahedrally order liquid, possessing an energetically favorable configuration [24]. At the temperature corresponding to the LLCP, in both systems, the minimum becomes very deep and a maximum is reached at high densities. This indicates a possible occurrence of a second minimum at higher densities. At very low temperatures, when the entropic contribution to $F = U - TS$ becomes less important, the behaviour of F can be approximated with the behaviour of U, thus minima in the behaviour of potential energy can be seen as indications of the appearance

of stable liquid phases (i.e. LDL and HDL). If we compare the the potential energy of bulk water and of NaCl(aq) we can notice, that apart from a shift in the absolute value, due to the presence of the ions, the behaviour is quite similar in the two systems. However the minimum at low density is more shallow in the solution. This is consistent with the fact the the LDL phase is made less stable in the aqueous solution.

In the following we will study the structural differences between the HDL and LDL phases, both for the water-water structure and for ion-water (hydration) structure. Let us begin with water-water structure.

5.4.1 Water-water structure

First of all let us see how the oxygen-oxygen RDF changes with density in bulk water, at the LLCP temperature, $T = 190$ K. The $g_{OO}(r)$ of bulk water are reported in Fig. 5.13 for decreasing densities, from $\rho = 1.10$ g/cm^3 to $\rho = 0.86$ g/cm^3 (at this temperature the density corresponding to the LG-LMS). It can be noted that as a general trend we have an increase of the first peak, with decreasing density. The second peak is similar for densities from $\rho = 0.86$ g/cm^3 to $\rho = 0.98$ g/cm^3, while its position starts to shift to lower distances from $\rho = 1.02$ g/cm^3. According to the phase diagram of Fig. 5.10 the LLCP is located at $\rho = 1.06$ g/cm^3 for bulk water and at

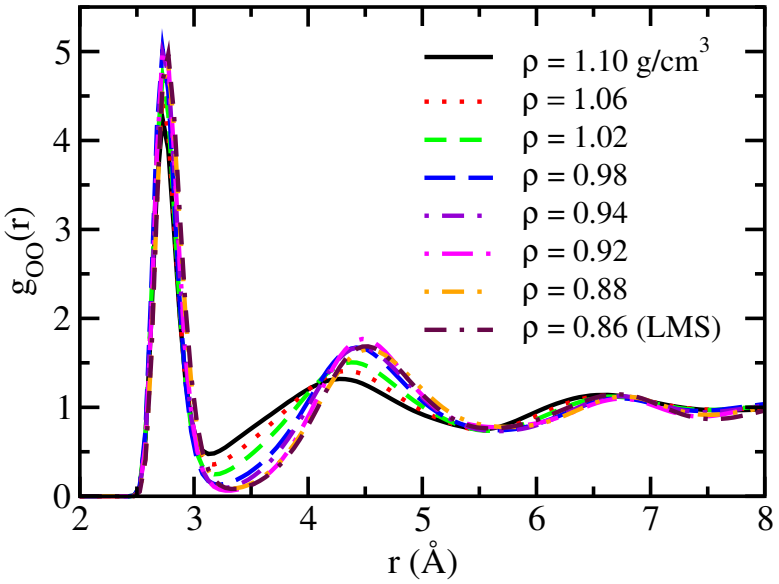

Figure 5.13: Oxygen-oxygen RDF of bulk water at $T = 190$ K for densities from $\rho = 1.10$ g/cm^3 to $\rho = 0.86$ g/cm^3 (LG-LMS).

$\rho = 0.99$ g/cm^3 for NaCl(aq). In the following we will take into account the RDFs for densities values well above and well below the estimated critical densities, $\rho = 1.10$ g/cm^3 for the HDL phase and $\rho = 0.92$ g/cm^3 for the LDL phase. We will also consider the RDFs at the LLCP temperature. Although the two phase region is rigorously below the LLCP, the structural properties of the two phases are maintained at the LLCP temperature, for densities well above and well below the LLCP.

The features of water-water structure in the HDL ($\rho = 1.10$ g/cm^3) and LDL ($\rho = 0.92$ g/cm^3) phases of bulk water are shown in Fig. 5.14. The RDFs are plotted at the critical temperature $T = 190$ K. For comparison in the same figure the RDFs corresponding to the density of the LG-LMS line, $\rho = 0.86$ g/cm^3 are also reported. The position of the first peak of the O-O RDF is the same in HDL and LDL, while its height is lower in the HDL phase. The second peak structure is very different in the two cases. In the HDL case its position shifts to lower distances, with a decrease of the height and a broadening of the shape with respect to LDL. The O-H RDF first peak is lower in the HDL and positioned at slightly lower distances with respect to LDL. This slightly shift is conserved between the first and second shell, while the position and the shape of the second shell are quite similar in HDL and LDL apart from the appearance of a shoulder in HDL. Moreover, while in LDL is present a well defined third shell, it disappears in HDL. Also the H-H RDF first peak of HDL is lower and slightly shifted to lower distances with respect to LDL. In this case the second shell is wider in the HDL with more exchange within the first and second shell. The overall trend of water-water RDFs and in particular the difference is the structure of the second shell of the O-O RDF clearly shows the disruption of hydrogen bonds between the first and second shell of water molecules that occurs in HDL, causing the collapse of the second shell with respect to the tetrahedrally coordinated LDL, as previously observed experimentally [104]. The results shown here are in fact in good agreement with the ones obtained in neutron diffraction experiments by Soper and Ricci [104]. We have said before that TIP4P model is a reliable potential for the study of thermodynamics of supercooled water. These results confirm the validity of the model also for the study of the structural properties in the supercooled region.

In Fig. 5.15 the HDL and LDL water-water RDFs for bulk water and for NaCl(aq) are compared together. As a general trend the water-water RDFs for NaCl(aq) remain fairly similar to those for bulk water. However some differences appear for the LDL phase. The height of the first peak of $g_{\mathrm{OO}}(r)$, $g_{\mathrm{OH}}(r)$ and $g_{\mathrm{HH}}(r)$ is slightly lower in the NaCl(aq) LDL with respect to the corresponding phase of bulk water. Moreover in the LDL $g_{\mathrm{OO}}(r)$ the first minimum moves to lower distances and the height of the second peak reduces

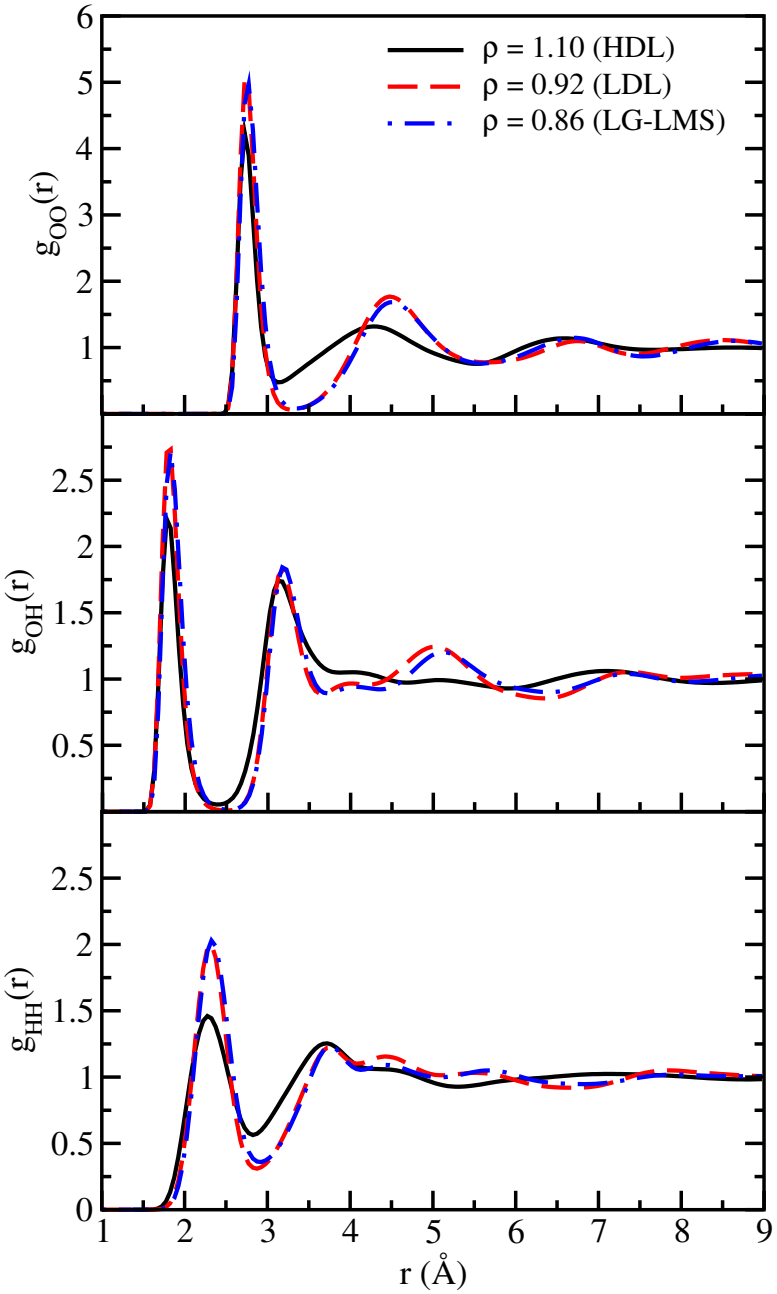

Figure 5.14: Oxygen-oxygen (top panel), oxygen-hydrogen (central panel) and hydrogen-hydrogen (bottom panel) RDFs for bulk water at $T = 190$ K. Solid lines: $\rho = 1.10$ g/cm^3 (HDL); dashed lines: $\rho = 0.92$ g/cm^3 (LDL); dot-dashed lines: $\rho = 0.86$ g/cm^3 (LG-LMS).

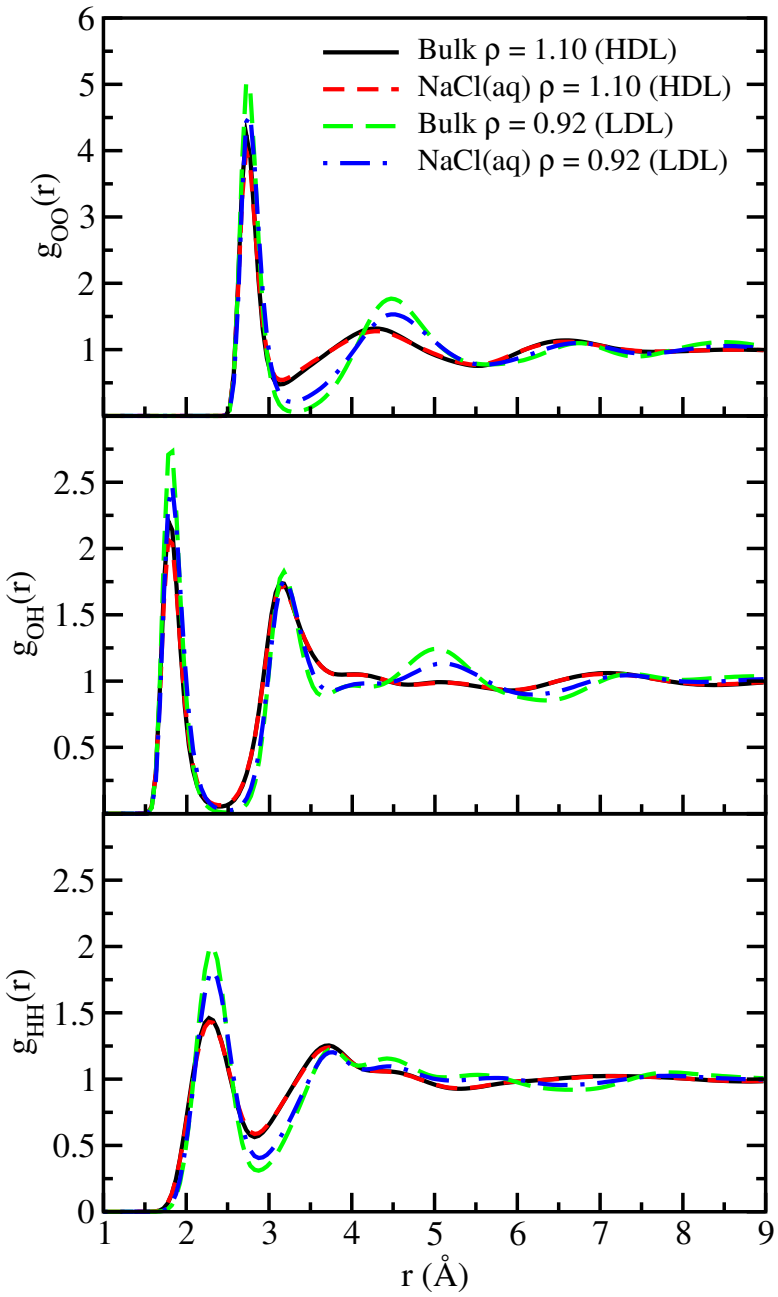

Figure 5.15: Oxygen-oxygen (top panel), oxygen-hydrogen (central panel) and hydrogen-hydrogen (bottom panel) RDFs for bulk water at $T = 190$ K and for NaCl(aq) at $T = 200$ K. Solid lines: bulk $\rho = 1.10$ g/cm^3 (HDL); dashed lines: NaCl(aq) $\rho = 1.10$ g/cm^3 (HDL); long dashed lines: bulk $\rho = 0.92$ g/cm^3 (LDL); dot-dashed lines: NaCl(aq) $\rho = 0.92$ g/cm^3 (LDL).

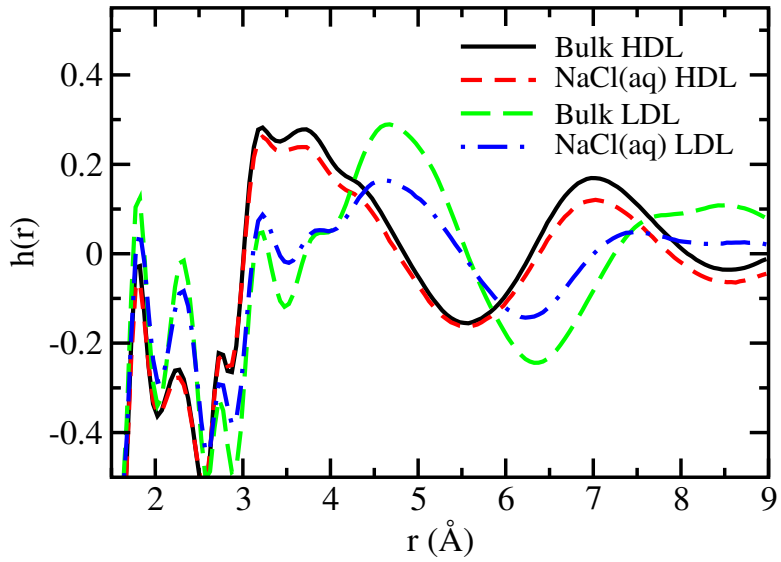

Figure 5.16: Correlation function $h(r)$, see text for definition, for bulk HDL (solid line), NaCl(aq) HDL (dashed line), bulk LDL (long dashed line) and NaCl(aq) LDL (dot-dashed line).

in NaCl(aq). In the $g_{\mathrm{OH}}(r)$ the first and second shell are not affected while the third shell is damped for NaCl(aq). At this concentration, the effect of the ions on water-water structure is not strong and the main features of bulk water are preserved in the aqueous solution. Nonetheless the LDL phase is more affected by the presence of ions than HDL. This could be explained by a certain degree of disruption of hydrogen bonds induced by the ions. In fact the overall effect of ions seems to be the reduction of the LDL character of the structure, making it more similar to the HDL one. This is again in agreement with what we observed studying the thermodynamics, namely the restriction of the region of existence of the LDL phase in the aqueous solution.

We can now complete the comparison between HDL and LDL in bulk water and NaCl(aq), considering the correlation function

$$h(r) = 4\pi\rho r[0.092 g_{\mathrm{OO}}(r) + 0.422 g_{\mathrm{OH}}(r) + 0.486 g_{\mathrm{HH}}(r) - 1] \quad . \qquad (5.5)$$

This correlation function can be obtained in neutron diffraction experiments, performing the Fourier transform of the intermolecular part of the structure factor $S(Q)$. Details about its derivation are given in Ref. [205]. In particular $h(r)$ was measured in neutron diffraction experiments aimed

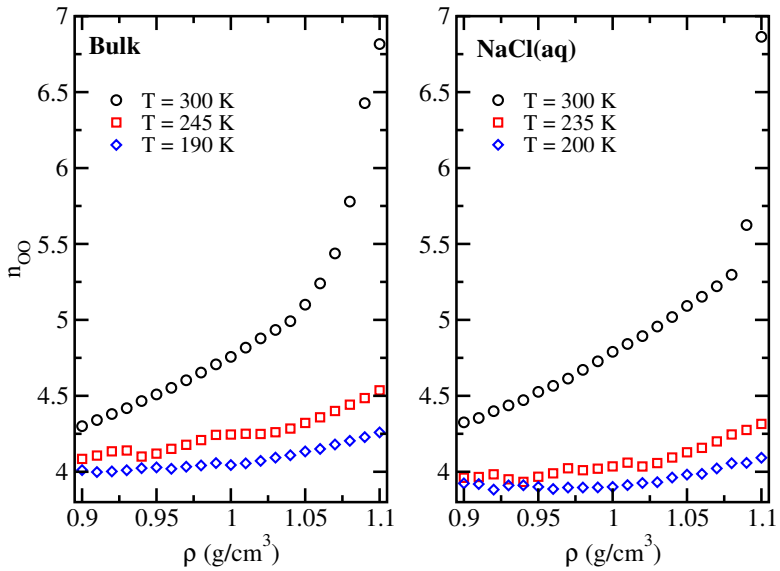

Figure 5.17: Oxygen-oxygen first shell coordination numbers at constant temperature, as a function of density, for bulk water (left panel) and NaCl(aq) (right panel). The temperatures are $T = 300$ K, $T = 245$ K and $T = 190$ K for bulk water and $T = 300$ K, $T = 235$ K and $T = 200$ K for NaCl(aq).

to the study of the high density amorphous (HDA) and low density amorphous (LDA) phases of water [206, 207] that are supposed to be the solid counterparts of HDL and LDL. In Fig. 5.16 the $h(r)$ correlation function is shown for HDL and LDL, both for bulk water and NaCl(aq). The shape of this correlation function is in qualitative agreement with the ones found for HDA and LDA amorphous phases, as previously found in simulations of bulk water performed with the ST2 potential [24]. Also in this case it can be observed that the main modifications take place in the LDL phase. There are in fact a significant reduction of the peak at about 4.6 Å and the disappearance of the peak at about 7.5 Å. This is consistent with the behavior of the LDL we have seen looking at the water-water RDFs.

To conclude the analysis of water-water structure we now look at the behavior of the oxygen-oxygen first shell coordination numbers, calculated at constant temperature as a function of density. The first shell coordination numbers can be obtained integrating the $g_{OO}(r)$ up to the distance corresponding to the first minimum

$$n_{OO}(r) = 4\pi\rho_O \int_0^{r_{min}} g_{OO}(r) r^2 \, dr \quad . \tag{5.6}$$

Therefore they represent the average number of first-neighbours around

an oxygen atom. The O-O first shell coordination numbers are reported in Fig. 5.17 for the same temperatures reported in Fig.5.12 for the study of the potential energy: $T = 300$ K, $T = 245$ K and $T = 190$ K for bulk water and $T = 300$ K, $T = 235$ K and $T = 200$ K for NaCl(aq). At ambient temperature, both in bulk water and in NaCl(aq), the coordination numbers decrease monotonically with the density and they do not reach the value of 4, typical of LDL [24], in the range of densities spanned by the simulations. When temperature is decreased the coordination numbers begin to approach the asymptotic value of 4, upon decreasing density. At the lowest temperature the value of 4 is reached already at quite high densities. In this case we can notice that HDL and LDL seem to be affected in a similar way by the presence of ions. In NaCl(aq) the average number of first-neighbour is slightly lower than in bulk water. However the weakening of the tetrahedral configuration of the LDL first shell might allow for a reorganization of bonds that leads to the more compact second shell structure of HDL, as we have seen looking at the RDFs.

5.4.2 Ion-water structure

Until now we have focused on the differences in water-water structure for HDL and LDL. We now want to investigate the features of the ion-water (hydration) structure in the two liquids. The hydration structure in NaCl(aq) at ambient temperature and in the moderately supercooled region has been the subject of several experimental [136,142,145] and simulation works [147, 148,152,155,158,159]. The hydration structure close to the LLCP has never been investigated before.

First let us consider the general features of the hydration shells. In Fig. 5.18 are shown the Na-water and Cl-water RDFs, for $\rho = 1.00$ g/cm^3, at ambient temperature, $T = 300$ K and in the deep supercooled region, $T = 200$ K, corresponding to the LLCP temperature of the solutions. Let us also state, with regard to the results shown in Sec. 4.4 that here in this case the RDFs at $T = 300$ K are in the normal region, while the ones at $T = 200$ K are within the region of density anomaly. For all the four couples we can observe that two well defined hydration shells are present. The height of both the first and second shell of the RDFs increases when the system is supercooled. For the Na-O and Cl-O also a slight shift of the position of the second peak to lower distances can be noted upon supercooling. These results indicate that upon supercooling, within the region of density anomaly, the hydration shells tend to stabilize and become more compact. For the Cl-O and Cl-H couples the first and the second peak of the RDF are very well separated, by roughly 1.0 Å. In the case of sodium this distance reduces to circa 0.6 Å and

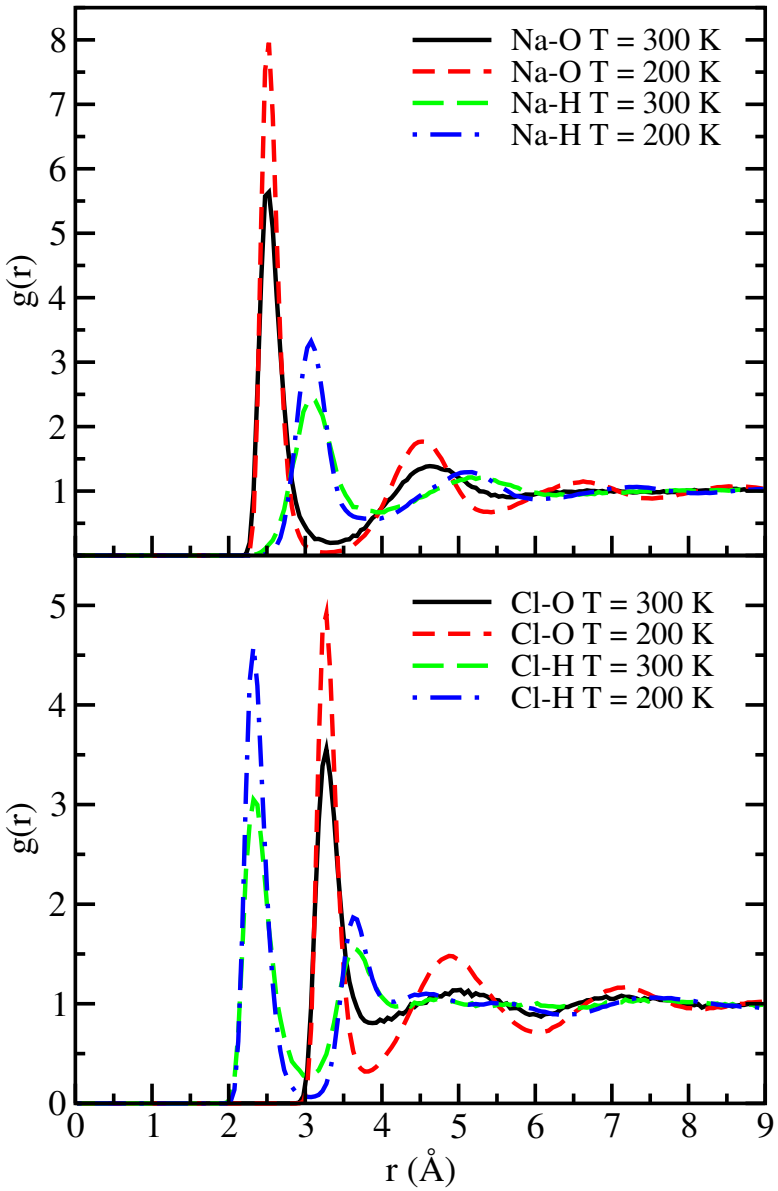

Figure 5.18: (Top panel) Na-O RDFs at $T = 300$ K (solid line) and at $T = 200$ K (dashed line), Na-H RDFs at $T = 300$ K (long dashed line) and at $T = 200$ K (dot-dashed line), all for density $\rho = 1.00$ g/cm^3. (Bottom panel) Cl-O RDFs at $T = 300$ K (solid line) and at $T = 200$ K (dashed line), Cl-H RDFs at $T = 300$ K (long dashed line) and at $T = 200$ K (dot-dashed line), all for density $\rho = 1.00$ g/cm^3.

an overlap of the Na-O and Na-H hydration shells is also present. We can notice that in the case of the chloride ion the structure and the shape of the shells are similar to the case of the O-O and O-H structures, see Fig. 5.14 and Fig. 5.15. From this consideration we can argue that the chloride ion can substitute an oxygen atom in the hydration shell, forming linear hydrogen bonds with oxygen atoms, as indicated by the sharp Cl-H first peak. This substitution cannot take place in the case of the Na ion. In fact its positive charge induces a major rearrangement of the bonds that produces a more packed structure. The results obtained for the Na and Cl hydration structure is in good agreement with what found experimentally, with the neutron diffraction technique [136, 142].

In Fig. 5.19 we present the hydration structure of Na and Cl ions in the HDL, $\rho = 1.10$ g/cm^3 and in the LDL, $\rho = 0.92$ g/cm^3, at $T = 200$ K. In the case of Na ion, the RDFs are not very different in the HDL or LDL. The first and second peak of the Na-O RFDs and the first peak of the Na-H increase in the LDL, with respect to HDL. The position of the peaks remain similar apart from a slight shift to higher distances of the second shell of Na-O in the LDL. In the case of the Cl ion, the Cl-H RDFs are unaltered either in the LDL or HDL environment, but some differences appear in the Cl-O couple. The first peak is in fact higher in LDL and the second peak is higher and shifted to longer distances. Generally speaking, there seem to be few differences in the hydration structure of the ions in the HDL or LDL solvent, at least at this concentration. The only significant difference is in the second shell of the Cl-O RDF.

We have said before the the hydration structure of the chloride resembles the O-O and O-H structure with the possibility of chloride ion substituting the central oxygen atom. We want now to further inquire this possibility. To do so, we plot in Fig. 5.20, the O-O and Cl-O RDFs for HDL and LDL with distances rescaled by the Lennard-Jones (LJ) interaction distance parameter σ. For the O-O pair $\sigma = 3.154$ Å, as given in the TIP4P model [188], for the Cl-O pair, $\sigma = 3.561$ Å, as reported in Table 5.1. Both in LDL and in HDL the chloride ion has the effect of pulling inward the second shell if compared with the corresponding O-O RDF. We can make a quantitative comparison considering the rescaled distance between the first and the second shell ΔR. In the HDL case, $\Delta R = 0.49$ for the O-O pair and $\Delta R = 0.42$ for the Cl-O pair. In the LDL case, $\Delta R = 0.55$ for the O-O pair and $\Delta R = 0.44$ for the Cl-O pair. Thus we can see that in the LDL the chloride ion has the effect of pulling inward the second shell of oxygen atoms.

Looking at Fig. 5.14 and Fig. 5.15, we have seen that for the O-O RDF the main difference in the LDL or HDL case is the shift of the second shell toward lower distances in the HDL. We have now a possible explanation of

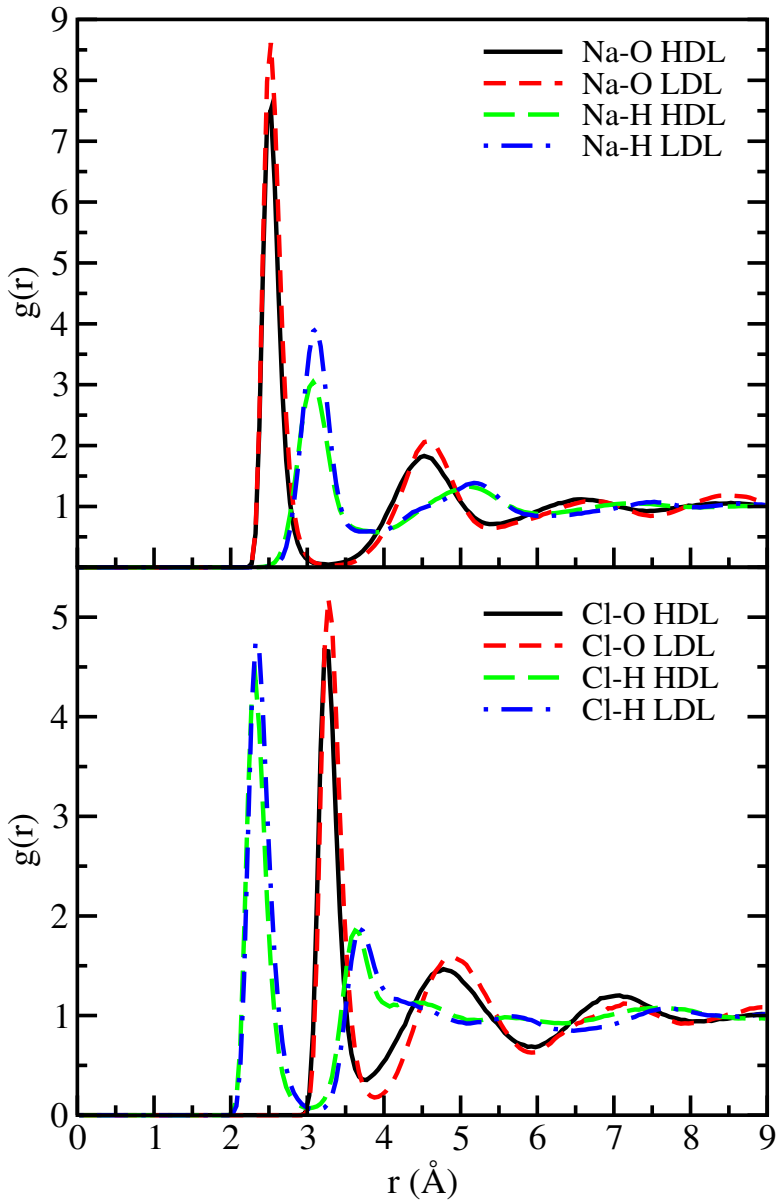

Figure 5.19: (Top panel) Na-O RDFs for HDL (solid line) and for LDL (dashed line), Na-H RDFs for HDL (long dashed line) and for (dot-dashed line), all at $T = 200$ K. (Bottom panel) Cl-O RDFs for HDL (solid line) and for LDL (dashed line), Cl-H RDFs for HDL (long dashed line) and for LDL (dot-dashed line), all for $T = 200$ K.

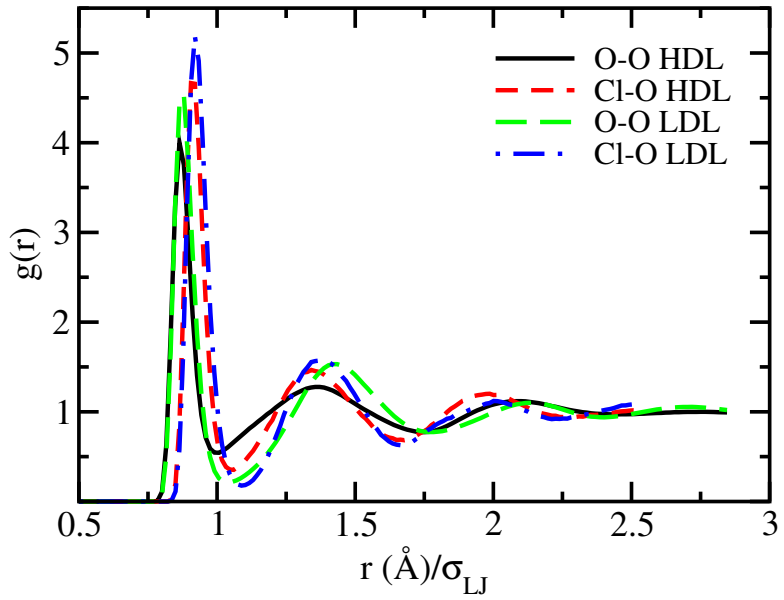

Figure 5.20: Comparison of the O-O (solid line: HDL; long dashed line: LDL) and Cl-O (dashed line: HDL; dot-dashed line: LDL) RDFs, rescaled by their respective LJ interaction distance parameter σ

the fact that ions seem to affect LDL more than HDL. From the picture we described, the chloride ion can take the place of the central oxygen atom at the cost of bending hydrogen bonds and pulling inward the second shell of oxygen atoms. This can be easily tolerated in HDL, where the structure of the second shell is already collapsed but the LDL structure is instead strained. In this way the substitution operated by the chloride ion causes the LDL structure to become more HDL-like. As a consequence the region of existence of the LDL phase is shrunk in the NaCl(aq) if compared to that of bulk water, as we have seen studying the thermodynamics in Sec. 5.3.

We can summarize the results obtained from the study of the structural properties of the JJ-TIP4P set stating the following points. We found that the TIP4P model is able to reproduce the structure of the two phases of supercooled liquid water, beyond being a very good potential for the study of liquid an solid water thermodynamics. As already observed in the study of the thermodynamics of NaCl(aq), we observed that also in the case of the structural properties, the LDL phase is more affected than the HDL phase by the presence of ions. The comparison of the hydration structures revealed that a possible mechanism of disturbance of the LDL structure is the substitution of the oxygen by the chloride ion. The ion pulls inward the second shell of oxygen disrupting the LDL structure. As a consequence, the LDL is

less stable in NaCl(aq) and its a region of existence in the thermodynamic plane is reduced, with a consequent shift of the whole phase diagram, LLCP included, to lower pressures.

Chapter 6

Results for the HS-JRP set

At variance with the PR-TIP4P and the JJ-TIP4P sets, the HS-JRP set was not simulated using standard molecular dynamics (MD) but the discrete molecular dynamics (DMD) technique. The systems in the HS-JRP set are coarse-grained models for hydrophobic solutes in water, that are composed by hard spheres (HS) and Jagla ramp potential (JRP) particles [51]. The hard cores contained in these potentials are more readily dealt with the DMD method.

The results presented in this chapter are focused on the effect of hydrophobic solutes and the role of concentration in modifying the liquid-liquid phase diagram of water. The first section of this chapter, Sec. 6.1, is devoted to explain the main features of the DMD method. The specific details and the simulation protocol for the HS-JRP set are provided in Sec. 6.2.

In Sec. 6.3 the results on the thermodynamics of the systems are presented and discussed, while in Sec. 6.4 the results on the diffusive behaviour of the systems and on the structure along the critical isochore are analysed.

6.1 Discrete Molecular Dynamics

DMD is a qualitatively different kind of MD that is useful in dealing with potentials that are discontinuous functions of the distance. This kind of MD is *collision driven*, in fact a so called collision takes place each time the distance between two particles in the system becomes equal to a point of discontinuity in the interaction potential. Between collisions the particles travel in straight lines and at constant velocity but at the collision time the velocity of particles changes suddenly. The velocity change is determined considering the the laws of conservation of the momentum and of the energy. In Fig. 6.1 a diagram of the collision between two particles is reported.

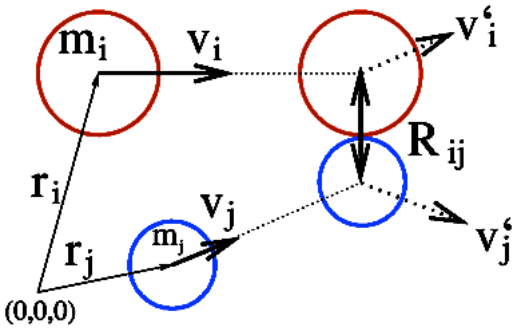

Figure 6.1: Diagram of the collision between two particles. The initial positions of the particles of mass m_i and m_j are $\mathbf{r}_i$ and $\mathbf{r}_j$ respectively. They travel at constant velocities $\mathbf{v}_i$ and $\mathbf{v}_j$, collide at distance $\mathbf{R}_{ij}$ and their velocities are modified to $\mathbf{v}'_i$ and $\mathbf{v}'_j$. Courtesy of S. V. Buldyrev.

Let us consider two particles of mass m_i and m_j, at initial positions $\mathbf{r}_i$ and $\mathbf{r}_j$ and traveling at constant velocities $\mathbf{v}_i$ and $\mathbf{v}_j$. The collision distance is $\mathbf{R}_{ij}$, where the interaction potential between particle i and particle j has a discontinuity. If we define $\mathbf{r}_{ij} = \mathbf{r}_i - \mathbf{r}_j$ and $\mathbf{v}_{ij} = \mathbf{v}_i - \mathbf{v}_j$ the collision time is determined by the equation

$$|\mathbf{r}_{ij}(t + t_{ij})| = |\mathbf{r}_{ij} + \mathbf{v}_{ij}t_{ij}| = \mathbf{R}_{ij} \tag{6.1}$$

whence

$$(r_{ij} + t_{ij}v_{ij})^2 = R_{ij}^2 \quad . \tag{6.2}$$

The DMD algorithm calculates the shortest collision time in the system

$$\delta t = \min_{i<j} t_{ij} \tag{6.3}$$

and moves all the particles in the system until the next collision time

$$\mathbf{r}'_i = \mathbf{r}_i + \delta t \mathbf{v}_i \tag{6.4}$$

then it assigns the new velocities to particles i and j considering the laws of conservation of the momentum

$$m_i\mathbf{v}_i + m_j\mathbf{v}_j = m_i\mathbf{v}'_i + m_j\mathbf{v}'_j \tag{6.5}$$

and of the total energy

$$\frac{m_i v_i^2}{2} + \frac{m_j v_j^2}{2} + U_{ij} = \frac{m_i v_i'^2}{2} + \frac{m_j v_j'^2}{2} + U'_{ij} \quad . \tag{6.6}$$

The DMD algorithm is more efficient than standard MD for low density systems [109]. The positions and velocities of the particles are in fact updated only when they collide. Moreover the search for the next collision time can be sped up dividing the system into small subsystems in order to calculate collision times only between particles situated in neighboring subsystems.

As in regular MD also in DMD it is possible to work in different ensembles from the microcanonical NVE. To fix the temperature, a modified Berendsen algorithm [12, 208] can be applied to rescale the velocities of the particles. The temperature of the thermal bath T_0 can be set making use of the following equation that adjusts the temperature after N collisions,

$$T' = \bar{T}(1 - \kappa_T \Delta t) + T_0 \kappa_T \Delta T \tag{6.7}$$

where T' is the new temperature, $\bar{T}$ is the average temperature in the time Δt during which N collisions take place and κ_T is the heat exchange coefficient.

If we want also to fix the pressure of the system, this can be done using the Berendsen algorithm [181] that rescales the positions of the particles of the system and the box vector each Δt_P time steps. The equations read

$$\mathbf{r}_i' = \mathbf{r}_i + \mathbf{r}_i \kappa_P (\bar{P} - P_0) \tag{6.8}$$

$$\mathbf{L} = \mathbf{L} + \mathbf{L} \kappa_P (\bar{P} - P_0) \tag{6.9}$$

where $\mathbf{L} = (L_x, L_y, L_z)$ is a vector containing the lengths of the edges of the simulation box, P_0 is the barostat pressure, $\bar{P}$ is the average pressure during Δt_P and κ_P is the pressure rescaling coefficient.

6.2 Simulation details for the HS-JRP set

The HS-JRP set is made by the simulations, performed with the DMD method, of the mixture of hard spheres (HS) and water-like solvent particles that interact between them via the spherically symmetric Jagla ramp potential (JRP). For this set we define the composition in term of the molar fraction of HS x_{HS}. We studied the solutions of HS in JRP particles, with $x_{HS} = 0.10, 0.15$ and 0.20 and the 1:1 mixture of HS and JRP particles, $x_{HS} = 0.50$ [51]. This set of simulations was mostly run during the second year of the Ph. D. program, while the analysis of the results was performed between the second and the third year.

The JRP [55, 56] belongs to a family of spherically symmetric potentials composed by a hard core plus a linear repulsive ramp. The tuning parameter of this potential is the ratio between its two characteristic lengths,the hard core distance and the soft core distance. Changing this parameter allows the JRP to span the range of behaviour from hard sphere to water-like [17, 58, 59]. With the appropriate choice of the parameters, the JRP potential displays water-like behaviour and in particular thermodynamic [12, 17, 59], dynamic [12, 57] and structural [58] anomalies of water. The JRP used for the HS-JRP simulations is shown in Fig. 6.2.

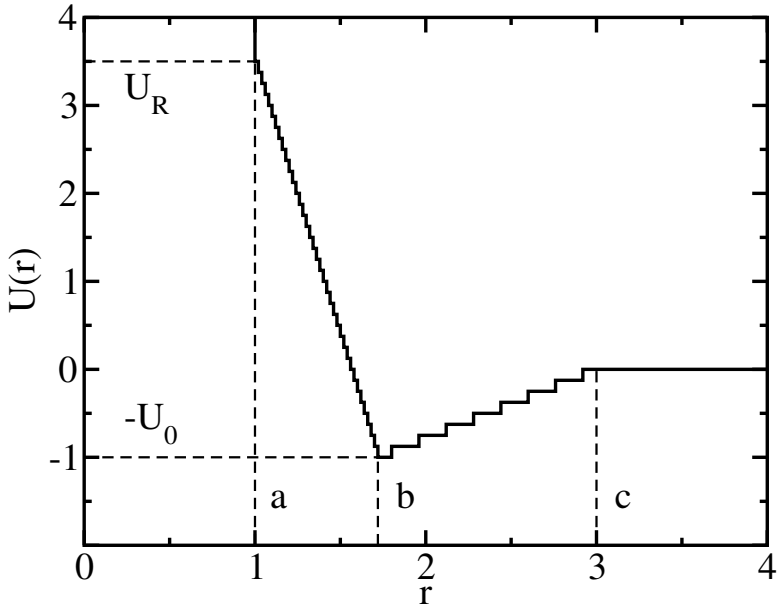

Figure 6.2: Spherically symmetric JRP. This potential has two length scales: the hard core diameter $r = a$ and the soft core diameter $r = b$. The parameters used for the simulations are $U_R/U_0 = 3.56$, $b/a = 1.72$ and $c/a = 3$. The potential has been discretised, with a discretisation step $\Delta U = U_0/8$.

The two characteristic lengths are the the hard core distance $r = a$ and the soft core distance $r = b$. The minimum of the energy is in correspondence of the soft core distance. The potential has also an attractive tail that extends to $r = c$. We have seen in Sec. 6.1 that the DMD algorithm works for potentials with discontinuities. In order to introduce such discontinuities, the interaction potential was discretised. The repulsive ramp was partitioned into 36 steps of width $0.02a$ and the attractive ramp was partitioned into 8 steps of width $0.16a$. For each step the energy jump is $\Delta U = U_0/8 = 0.125$. The parametrisation of this system, taken from previous works [12, 57], prevents the occurrence of crystallization. In particular

Table 6.1: Range of spanned box lengths, corresponding densities and range of temperatures in reduced units (see text) for each composition studied. Data for constant volume simulations.

x_{HS}	L_{min}	L_{max}	ρ_{min}	ρ_{max}	T_{min}	T_{max}
0.10	15.5	17.4	0.328	0.464	0.255	0.380
0.15	15.5	17.4	0.328	0.464	0.275	0.360
0.20	15.5	17.4	0.328	0.464	0.275	0.360
0.50	13.7	15.1	0.502	0.672	0.210	0.300

the ratio between the potential length scales was set to $b/a = 1.72$, $c/a = 3$. The value of the energy at $r = a$, $U_R = 3.56U_0$ was defined through least square linear fit to the discretised repulsive ramp. The interaction between JRP and HS and between HS and HS is given by the pure hard core potential with the same hard core distance $r = a$. The diameter of the HS is a, equal to the hard core distance of the JRP.

Most simulations were performed at constant N, V and T, with the temperature controlled rescaling the velocities employing a modified Berendsen algorithm (see Sec. 6.1). A subset of the simulations aimed to study the behaviour of the diffusion coefficient on a cooling path at constant pressure was performed at constant N, P and T, with P controlled allowing the edge of the simulation box to change over time using the Berendsen algorithm (see Sec. 6.1).

The number of particles contained in the cubic simulation box is $N_{tot} = N_{JRP} + N_{HS} = 1728$. The number of HS is $N_{HS} = 173$ for $x_{HS} = 0.10$, $N_{HS} = 260$ for $x_{HS} = 0.15$, $N_{HS} = 345$ for $x_{HS} = 0.20$ and $N_{HS} = 864$ for $x_{HS} = 0.50$.

For this set of simulations reduced units are used. Distances are in units of a, energy in units of U_0 and time in units of $a\sqrt{m/U_0}$, where m is the mass. The mass is assumed to be unitary. Densities are defined as $\rho \equiv N/L^3$, where L is the length of the edge of simulation box. The unit of density is a^{-3}; pressure is given in units of U_0/a^3 and temperatures in units of U_0/k_B.

In the reduced units, the simulation times are for all temperatures, $t_E = 1000$ for the equilibration runs and $t_P = 20000$ for the production runs.

Constant volume (density) simulations were performed for densities corresponding to box lengths $L/a = 15.5, \ldots, 17.4$ for $x_{HS} = 0.10, 0.15$ and 0.20 and for densities corresponding to box lengths $L/a = 13.7, \ldots, 15.1$ for $x_{HS} = 0.50$. The range of temperatures goes from $T = 0.255$ to $T = 0.380$ for $x_{HS} = 0.10$, from $T = 0.275$ to $T = 0.360$ for $x_{HS} = 0.15$ and 0.20 and from $T = 0.210$ to $T = 0.300$ for $x_{HS} = 0.50$. For all compositions the step

in the simulated temperatures is $\Delta T = 0.005$. In Table 6.1 the spanned ranges of box lengths, corresponding densities and of temperatures for each mole fraction are summarized.

Constant pressures simulations were also performed at $P = 0.321$ for $x_{HS} = 0.10$, $P = 0.347$ for $x_{HS} = 0.15$ and $P = 0.382$ for $x_{HS} = 0.20$. The range of temperature studied with constant pressure simulations goes from $T = 0.250$ to $T = 0.440$ (every $\Delta T = 0.010$) for $x_{HS} = 0.10$ and $T = 0.250$ to $T = 0.380$ (every $\Delta T = 0.010$) for $x_{HS} = 0.15$ and 0.20.

For the HS-JRP set [51], 20 isochores each were simulated for the $x_{HS} = 0.10, 0.15$ and 0.20 systems and 15 isochores were simulated for the $x_{HS} = 0.50$ system. For each isochores, 26 temperatures were simulated for $x_{HS} = 0.10$, 18 temperatures for $x_{HS} = 0.15$ and 0.20 and 19 temperatures for $x_{HS} = 0.50$. All together they amount to 1525 state points simulated. Adding additional 48 state points performed for the constant pressure simulations, the total states points simulated are 1573. Considering that each state point takes about one day on a Linux machine with an Intel dual-core processor (clock frequency 2.2 GHz) the total computational time amounts to about 38000 hours of CPU usage, equivalent to more than 4 CPU years.

This set of simulations were performed using a home written code by S. V. Buldyrev for DMD simulations. Most simulations were run on the Bethe cluster at Yeshiva University, New York City, New York (United States). This cluster allowed the execution of up to 20 serial jobs together, reducing the actual time needed to collect the data. Part of the simulations were also conducted on the INFN-Grid Roma Tre cluster [193] and on the HPC cluster [194] of the CNR-IOM *Democritos National Simulation Center* at SISSA, Trieste (Italy).

6.3 Thermodynamic results

The thermodynamics of the mixtures of HS and JRP particles, with mole fractions $x_{HS} = 0.10, 0.15, 0.20$ and 0.50 was studied analysing the results in the isochore $(P-T)$ plane and in the isotherms $(P-\rho)$ plane. In the ranges of temperatures and densities studied here the HS are completely soluble in JRP particles [35]. In fact in the range of state points we spanned, no demixing phenomena occurred. The thermodynamic properties of the bulk JRP liquid, with the same set of parameters used for this study, was previously extensively studied [12, 57]. In particular it was found that it shows a liquid-liquid critical point (LLCP) located at $T_c = 0.375$, $P_c = 0.243$ and $\rho_c = 0.370$.

Here the position of the LLCP was determined considering the points for

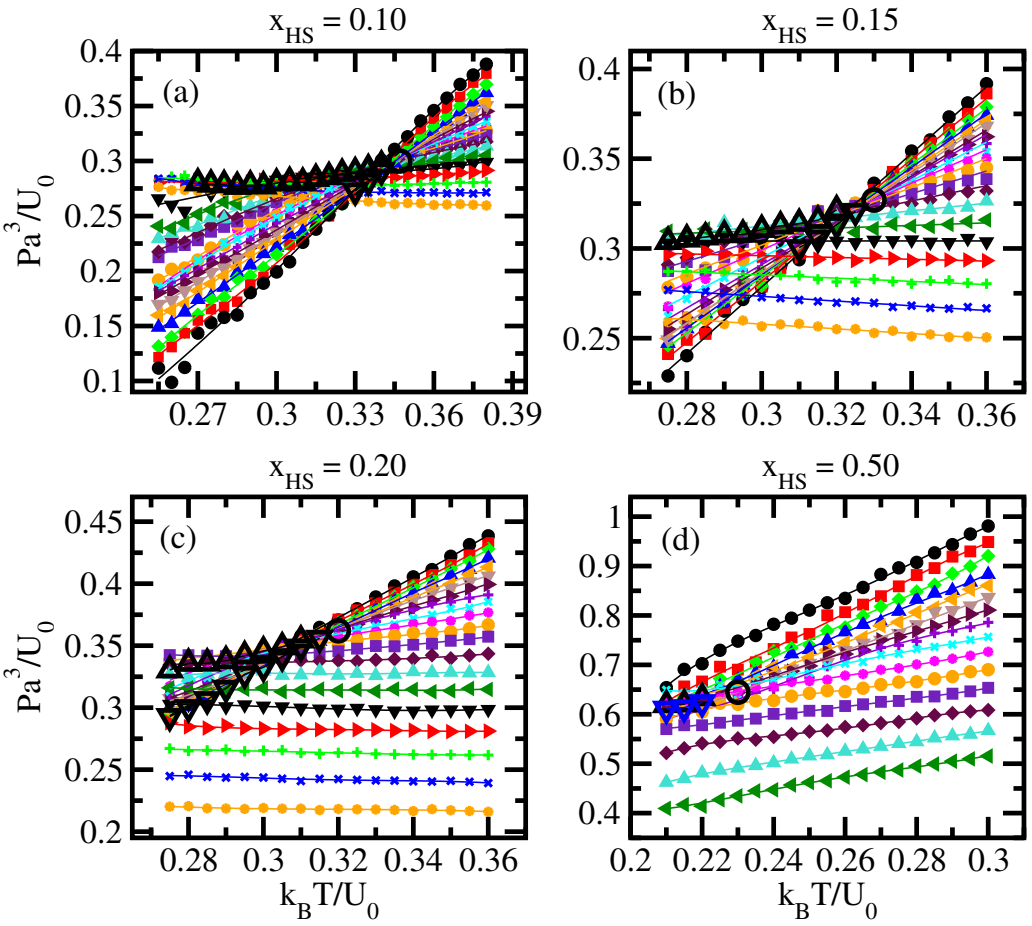

Figure 6.3: Isochores of the mixtures at the four different mole fractions, together with the positions of the LLCP (circles), LDL LMS (triangles up) and HDL LMS (triangles down). In all panels, the lines are fourth degree polynomial fits to the simulated state points. (a) $x_{HS} = 0.10$, isochores are drawn for $\rho = Na^3/L$, where $L/a = 17.4, 17.3, \ldots, 15.5$. The range of corresponding densities span from $\rho = 0.328$ to $\rho = 0.464$. (from bottom to top). The temperature range goes from $T = 0.255$ to $T = 0.380$. (b) $x_{HS} = 0.15$, the range of densities is the same of panel a. The temperature range goes from $T = 0.275$ to $T = 0.360$. (c) $x_{HS} = 0.15$, the ranges of densities and temperatures are the same as in panel b. (d) $x_{HS} = 0.50$, isochores are drawn for $\rho = Na^3/L$, where $L/a = 15.1, 17.0, \ldots, 13.7$. The range of corresponding densities span from $\rho = 0.502$ to $\rho = 0.672$. (from bottom to top). The temperature range goes from $T = 0.210$ to $T = 0.300$.

which the following relation holds

$$\left(\frac{\partial P}{\partial \rho}\right)_T = \left(\frac{\partial^2 P}{\partial \rho^2}\right)_T = 0 \quad . \tag{6.10}$$

The points of the LL-LMS have been calculated considering instead the points for which $(\partial P/\partial \rho)_T = 0$ but $(\partial^2 P/\partial \rho^2)_T \neq 0$, where the isothermal compressibility $K_T = (\partial \rho/\partial P)_T/\rho$ goes to infinity.

In Fig. 6.3 the isochores, in the $P - T$ plane, of the mixtures at the four different mole fractions are presented. Together with the isochores, the estimated position of the LLCP and the high density liquid (HDL) and the low density liquid (LDL) branches of the liquid-liquid limit of mechanical stability (LL-LMS) lines are also shown. It can be noted that for mole fractions up to $x_{HS} = 0.20$ the convergence of the isochores to the critical point is very clear. The isochores also cross at the points corresponding to the LL-LMS lines. Moreover for the three lowest mole fractions the low density isochore are almost flat. This indicates the presence of density anomaly, in fact we recall that the point of the temperature of maximum density (TMD) line are given by the zeros of the coefficient of thermal expansion α_P, where $(\partial P/\partial T)_\rho = 0$. For the 1:1 mixture of HS and JRP particles ($x_{HS} = 0.50$) the convergence of the isochores to the LLCP is not as precise at for the the three lowest mole fractions. The low density isochores in this case are not longer flat. Thus no density anomaly is observed for $x_{HS} = 0.50$.

The isotherms of the systems with $x_{HS} = 0.10, 0.15, 0.20$ and 0.50 are shown together in Fig. 6.4. Along with the isotherms of the systems, the positions of the LLCP are also reported. We can observe that the LLCP is positioned at the inflection point of the critical isotherms. Below the LLCP the isotherms show van der Waals-like loops that indicate the LL coexistence. It can be also noticed that when the mole fraction of solutes increases, the width of the region of coexistence narrows. For low densities, a crossing of the isotherms can be seen for the mole fractions $x_{HS} = 0.10, 0.15, 0.20$. For the points where isotherms cross, the relation $(\partial P/\partial T)_\rho = 0$ must hold. Thus this crossing signals the presence of density anomaly. The LLCP and the van der Waals-like structure can be found also for the highest mole fraction, $x_{HS} = 0.50$. However in this case, the crossing of the isotherms disappears, confirming what we have seen studying the isochores in Fig. 6.3. Therefore, although the density anomaly is not longer present at this high mole fraction, the LLCP does not vanish.

The coordinates of the LLCP for the four system are reported in Table 6.2, together with the coordinates of the LLCP of the bulk JRP particles system.

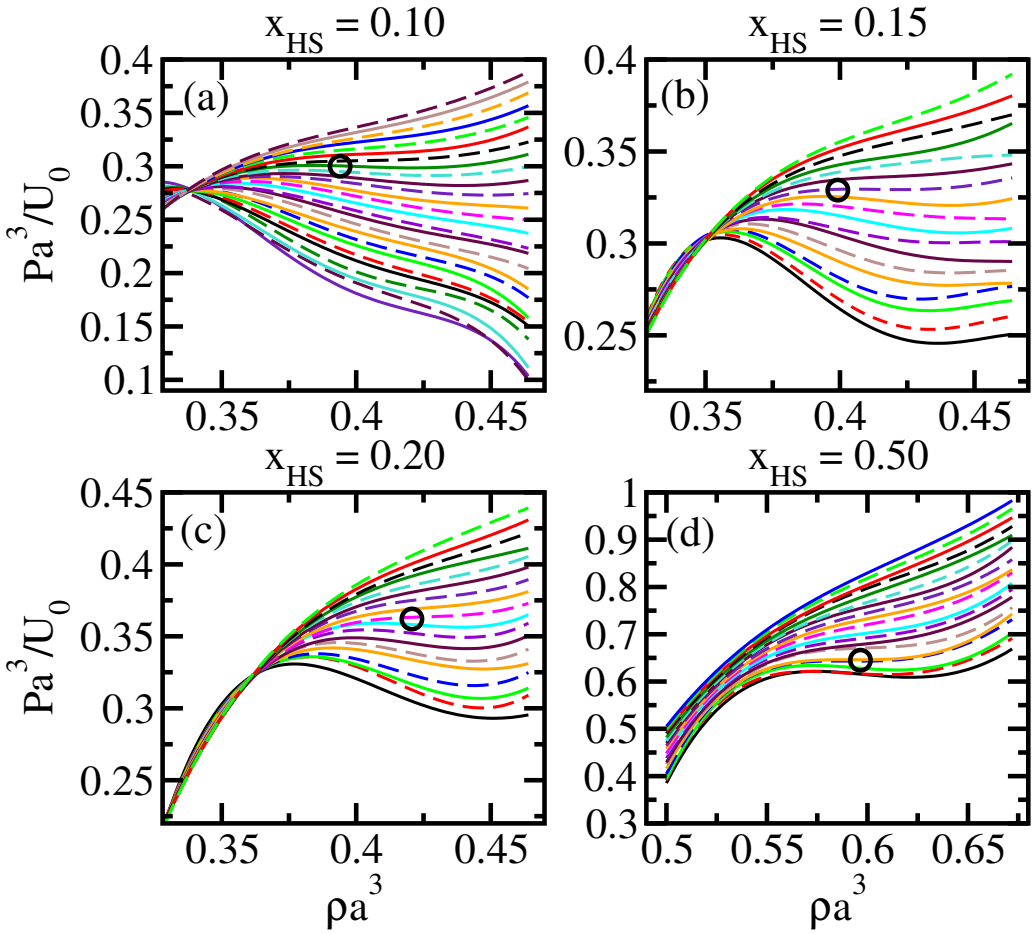

Figure 6.4: Isotherms of the mixtures at the four different mole fractions, together with the positions of the LLCP (circles). In all panels the lines are fourth degree polynomial fits to the simulated state points. (a) $x_{HS} = 0.10$, isotherms are drawn for temperatures from $T = 0.255$ to $T = 0.380$ every $\Delta T = 0.005$ (from bottom to top). (b) $x_{HS} = 0.15$, isotherms are drawn for temperatures from $T = 0.275$ to $T = 0.360$ every $\Delta T = 0.005$ (from bottom to top). (c) $x_{HS} = 0.20$, the temperature range is the same as in panel b. (d) $x_{HS} = 0.50$, isotherms are drawn for temperatures from $T = 0.210$ to $T = 0.300$ every $\Delta T = 0.005$ (from bottom to top).

Table 6.2: Coordinates of the LLCP for the bulk JRP particles system [12] and for the mixtures of HS and JRP particles, with mole fractions $x_{HS} = 0.10, 0.15, 0.20$ and 0.50.

x_{HS}	T_c	P_c	ρ_c
0.00 (bulk)	0.375	0.243	0.370
0.10	0.346	0.301	0.394
0.15	0.330	0.327	0.399
0.20	0.320	0.362	0.421
0.50 (1:1 mixture)	0.230	0.645	0.597

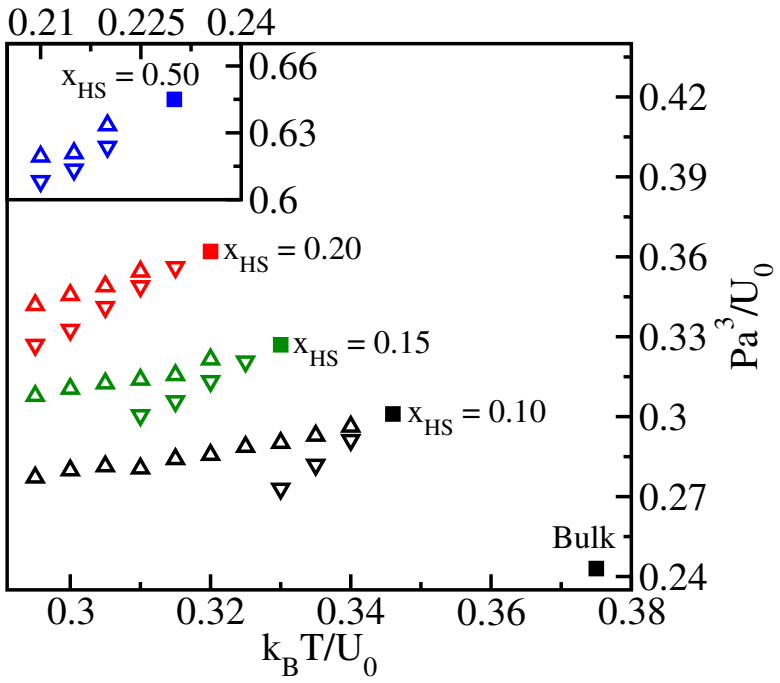

Figure 6.5: Position of the LLCP (squares) in the $P-T$ plane, LDL (triangles up) and HDL (triangles down) limit of mechanical stability (LMS) lines for the mixtures with HS mole fractions $x_{HS} = 0.10, 0.15, 0.20$. The position of the LLCP for the bulk JRP particles system is also reported for comparison. In the inset the analogous quantities are reported for the 1:1 mixture of HS and JRP particles ($x_{HS} = 0.50$).

The position of the LLCP along with the two branches of the LL-LMS line for all the studied mixtures are shown in Fig. 6.5. The LLCP moves to higher pressures and lower temperatures upon increasing the solute content. This shift of the LLCP could be connected to the fact the HS seem to be more favorably solvated in the low density phases [35]. In fact we can observe that the LDL region of the phase diagram progressively widens, as the mole fraction of HS increases.

Looking both at the isochores, Fig. 6.3, and at the isotherms, Fig. 6.4, it can be observed that the width of the coexistence envelope reduces upon increasing the solute content. The region where isochores cross in fact reduces on going from $x_{HS} = 0.10$ to $x_{HS} = 0.50$. In the isotherms, the width of the loop region becomes more and more narrow, spanning a minor range of densities, upon increasing the HS mole fraction. These results seem to indicate that upon further increasing the solute content the LLCP will disappear. The weakening of the indications of LL coexistence is consistent with what we have seen in the study of the PR-TIP4P set (Sec. 4.3) and with experimental observations of solutions of salts [131, 132].

If we want to compare the results obtained with the JRP to real water, we have to take into account the fact that the slope of the LL coexistence line is reversed for JRP particles with respect to the slope in water. In fact while the slope of the LL coexistence line is negative in water, it is positive for JRP particles [12, 13, 57]. Considering the Clausius-Clapeyron equation

$$\frac{dP}{dT} = \frac{\Delta S}{\Delta V} \tag{6.11}$$

we can derive that in the JRP system, the entropy of the HDL phase is lower than the one of the LDL phase. Thus the HDL phase is more ordered than the LDL phase. This is the opposite of what happens in water, where the LDL phase is more ordered [19]. This inversion is reflected also in the dynamic behaviour. In fact, while the LDL phase is strong and the HDL fragile in water, the opposite is true for JRP particles [12, 57]. Numerical values in real units for the LLCP of the JRP particles system and more realistic models for water, as for example the TIP5P model (see Ref. [17]) are quite distant. Nonetheless the phenomenology relative to the LLCP and to thermodynamic, dynamic and structural anomalies is preserved in the JRP system, provided the roles of HDL and LDL are exchanged [12, 57].

In Fig. 6.6 the LL coexistence line for the bulk JRP particles and the respective LLCP, calculated by Xu *et al.* [12], together with the critical line up to $x_{HS} = 0.50$, calculated in this work are reported. The critical line is the line that joins the LLCP of the mixtures. As we said before, we find that the LLCP in the mixtures moves to lower temperatures and higher pressures.

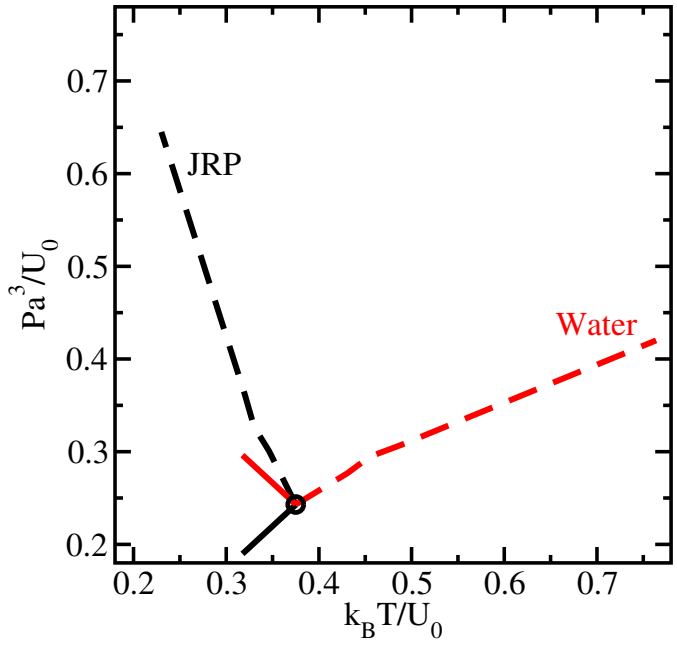

Figure 6.6: LL coexistence line (dark solid line) and LLCP (circle) for the bulk JRP system as calculated in Ref. [12] and the critical line for the mixtures up to $x_{HS} = 0.50$ as calculated in this work (dark dashed line). The same quantities have been rotated to match the slope of the coexistence line to the one of real water. The rotated coexistence line (light solid line) and the rotated critical line up to $x_{HS} = 0.50$ (light dashed line) are shown.

In order to obtain a prediction for the behaviour of mixtures of water with small hydrophobic solutes, we performed a rotation of the LL coexistence line calculated for JRP, bringing it to have a positive slope. The slope of the coexistence line has been reversed from θ to $-\theta$, performing a rotation of -2θ around the point corresponding to the LLCP. The same rotation has been applied to the critical line, calculated for the mixtures of HS and JRP. In the rotated system, see Fig. 6.6, we can see that the position of the LLCP moves to higher pressures and higher temperatures in the mixtures.

From these considerations we can predict that the temperature of occurrence of the LLCP can be elevated in mixtures of water and small hydrophobic solutes. We have seen in Sec. 5.3 that in the $c = 0.67$ mol/kg NaCl(aq) solution we studied, the LLCP moved to higher temperatures and lower pressures. Here we see that also with small hydrophobic solutes the temperature of the LLCP can be increased, being in this case the pressure higher with respect to bulk water. This shift induced by the hydrophobic solutes could be exploited in experiments to bring the LLCP in mixtures

above the homogeneous nucleation line, also avoiding to deal with negative pressures as in the case of the NaCl(aq).

6.4 Diffusivity and Structure

Now we study the diffusive behaviour of the mixtures of HS and JRP particles. First we will see the behaviour of the diffusion coefficient of the JRP particles for all mole fractions, calculated at constant temperature (isotherms of the diffusion coefficient) as a function of the density. Then we will look at the diffusion coefficient of the JRP particles and of the HS for $x_{HS} = 0.10$, 0.15 and 0.20 calculated at constant pressure, on a cooling path above the LLCP.

In Fig. 6.7 the diffusion coefficients, for the mole fractions $x_{HS} = 0.10$, 0.15, 0.20 and 0.50 calculated at constant temperature as functions of the density, are reported. The diffusivity anomaly, with the appearance of maxima in the isotherms of the diffusion coefficient is found up to highest HS content. The $x_{HS} = 0.10, 0.15, 0.20$ are studied in the same range of densities, from $\rho = 0.328$ to $\rho = 0.464$. Maxima of the diffusion coefficient are evident for $x_{HS} = 0.10, 0.15, 0.20$, while minima appear only for $x_{HS} = 0.20$. Minima for the $x_{HS} = 0.10, 0.15$ solutions are to be found for lower densities, out of the spanned range of densities. This can be due to the restriction of the region of existence of the diffusivity anomaly. Therefore the dynamic anomalies also, beyond the thermodynamic ones exist in a smaller range of densities, upon increasing the solute content. The diffusion coefficients at constant temperature for $x_{HS} = 0.50$ are calculated in the density range from $\rho = 0.502$ to $\rho = 0.672$, therefore they cannot be directly compared with the lower HS mole fraction cases. Nonetheless it can be observed that also for this high content of HS, the maxima in the the diffusion coefficient are present. Thus, while the density anomaly disappears for $x_{HS} = 0.50$, the diffusivity anomaly is still present.

Now we look at the behaviour of the diffusion coefficients for $x_{HS} = 0.10, 0.15, 0.20$, calculated at constant pressure on a cooling path above the LLCP. In the bulk JRP particles system it was found that the trend of the diffusion coefficient, calculated along a cooling path above the LLCP, displays a crossover from a high-temperature behaviour (LDL-like) to a low-temperature (HDL-like) behaviour, upon crossing the Widom line [12]. Both trends are Arrhenius but only the one on the low-temperature side of the Widom line can be classified as that of a strong liquid because of the magnitude of the activation energy. The high-temperature part instead resembles the behavior observed in the LDL phase at high temperature, that in the

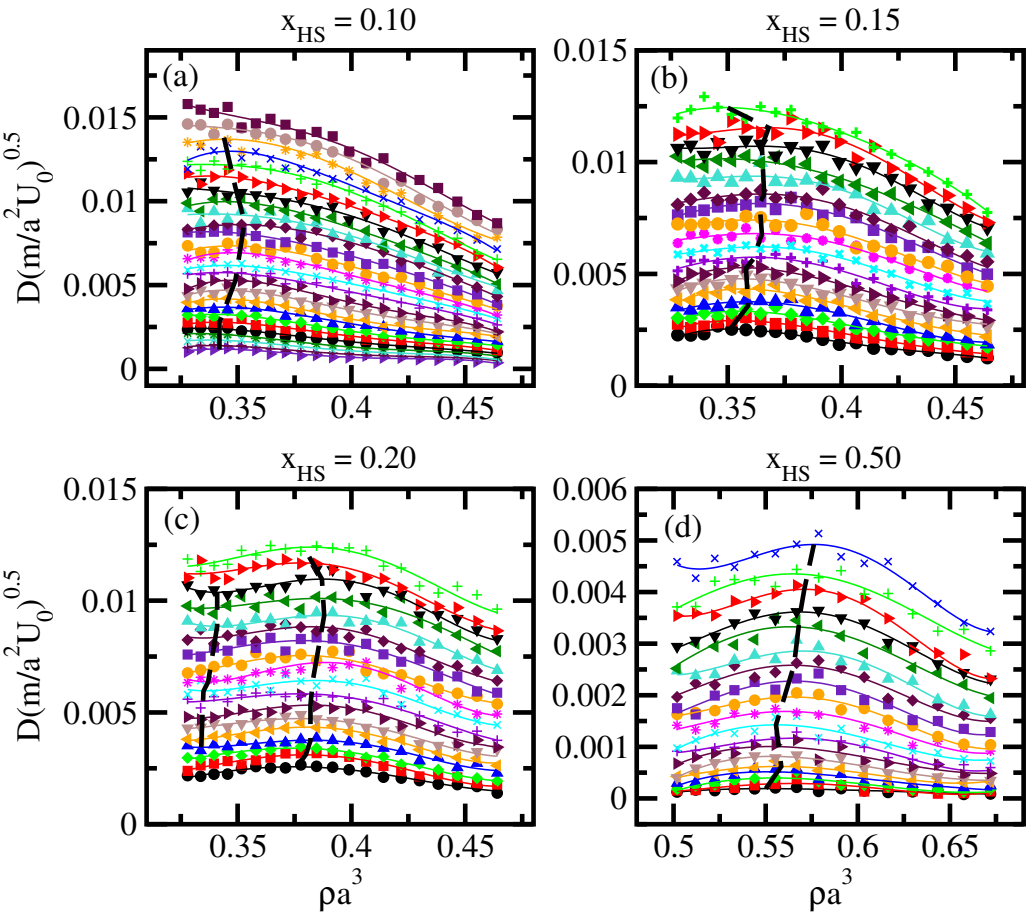

Figure 6.7: Diffusion coefficients of the JRP particles at constant temperature for the four mixtures at different HS mole fractions. In all panels the lines are fourth degree polynomial fits to the simulated state points. The dashed lines join the diffusivity extrema (maxima for $x_{HS} = 0.10, 0.15, 0.50$, maxima and minima for $x_{HS} = 0.20$. (a) $x_{HS} = 0.10$, isotherms of D are drawn for temperatures from $T = 0.255$ to $T = 0.380$ every $\Delta T = 0.005$ (from bottom to top). (b) $x_{HS} = 0.15$, isotherms of D are drawn for temperatures from $T = 0.275$ to $T = 0.360$ every $\Delta T = 0.005$ (from bottom to top). (c) $x_{HS} = 0.20$, the temperature range is the same as in panel b. (d) $x_{HS} = 0.50$, isotherms are drawn for temperatures from $T = 0.210$ to $T = 0.300$ every $\Delta T = 0.005$ (from bottom to top).

JRP particles system is fragile. From this observation it was deducted that also the JRP particles exhibits a dynamic crossover from a LDL-like (fragile) behaviour at high temperature to HDL-like (strong) behaviour at low temperature, in a way similar to the fragile to strong transition observed in water [98], with the difference that the strong liquid in the JRP particles system is the HDL. Furthermore, the diffusive crossover was connected to the maximum in the specific heat occurring at the Widom line, through the Adam-Gibbs relation $D = D_0 \exp(-C/TS_{\text{conf}})$, where S_{conf} is the configurational entropy. This is due to the proportionality between S_{conf} and S_{ex}, the excess entropy of the liquid with respect to the crystal [209]. As $C_P = T(\partial S/\partial T)_P$ and $C_P \propto C_P^{\text{ex}} \equiv T(\partial S_{\text{ex}}/\partial T)_P$, a rapid change of excess entropy, and consequently of the configurational entropy which constitute its largest part, can be expected close to the temperature for which the maximum of the specific heat occurs.

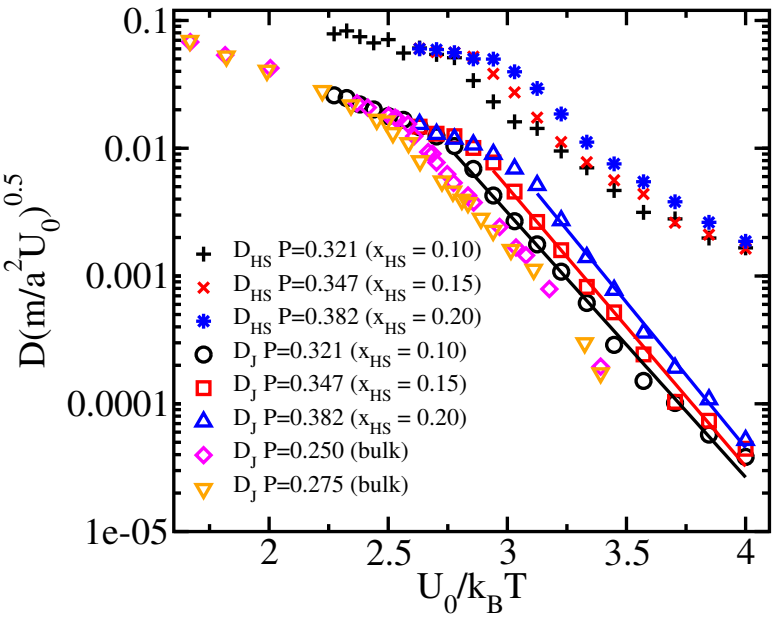

Figure 6.8: Diffusion coefficients for JRP particles and HS calculated along a constant pressure path above the LLCP. The pressures are $P = 0.321$ for $x_{HS} = 0.10$, $P = 0.347$ for $x_{HS} = 0.15$ and $P = 0.382$ for $x_{HS} = 0.20$. The lines correspond to the Arrhenius fit for JRP particles. The diffusion coefficients at constant pressure for the bulk JRP particles system at $P = 0.250$ and $P = 0.275$ are also reported for comparison.

In Fig. 6.8, the diffusion coefficients at constant pressure for JRP particles and HS are shown. For all compositions the pressure has been set to the critical pressure plus $\Delta P = 0.020$. For JRP particles, the crossover

present in bulk JRP, is also found in the $x_{HS} = 0.10, 0.15$ and 0.20 mixtures and at low enough temperature, below the Widom line, the diffusivity behaviour becomes that of HDL JRP liquid. The temperature of occurrence of the crossover in the diffusive behaviour decreases, upon increasing the mole fraction of solutes. As the Widom line is emanated from the LLCP, the shift of the crossover temperature to lower values is consistent with the shift to lower temperatures of the LLCP that we have seen studying the thermodynamics (see Fig. 6.5). The trend of the diffusive behaviour of the HS closely follows the one of the JRP particles, therefore we can derive that the diffusive behaviour of the HS solute is determined by the diffusivity of the solvent.

To summarize the study of the diffusive behaviour of our systems, we can say that the appearance of the diffusivity anomaly, with extrema in the trend of the isotherms of the diffusion coefficient, is preserved up to highest mole fraction, $x_{HS} = 0.50$. This is opposed to density anomaly that is no longer present at $x_{HS} = 0.50$. The region of existence of the diffusivity anomaly seems to narrow upon increasing the mole fraction of solutes, in analogy with what observed for the thermodynamic anomalies. The study of the behaviour of the diffusion coefficients at constant pressure, on a cooling path above the LLCP, for $x_{HS} = 0.10, 0.15, 0.20$ revealed that there exists a crossover from a LDL-like to a HDL-like behaviour, in analogy with what previously found for the bulk JRP particles system [12]. The crossover temperature decreases when the mole fraction of HS increases, consistently with the shift of the Widom line in the phase diagram.

Finally we can have a look at the solute-solute radial distribution functions (RDFs) of the systems at all mole fractions. In Fig. 6.9 the $g_{\text{HS-HS}}(r)$ calculated at the critical density of each systems, are reported. The temperatures considered are $T = 0.360$, the critical temperature and $T = 0.290$ for the solutions with $x_{HS} = 0.10, 0.15$ and 0.20 and $T = 0.300$, the critical temperature and $T = 0.210$ for the mixture with $x_{HS} = 0.50$. The progressive increase in the $g(r)$ close to the hard core distance indicates a small tendency to the clustering of HS, upon increasing the HS content. An anomalous behaviour of the solute-solute RDFs can be see for the lowest temperatures, below the LLCP. In fact they show a progressive decay towards the asymptotic behaviour on 1 at large r. This decay signals the segregation of the HS into the LDL phase below the critical point, along the coexistence line.

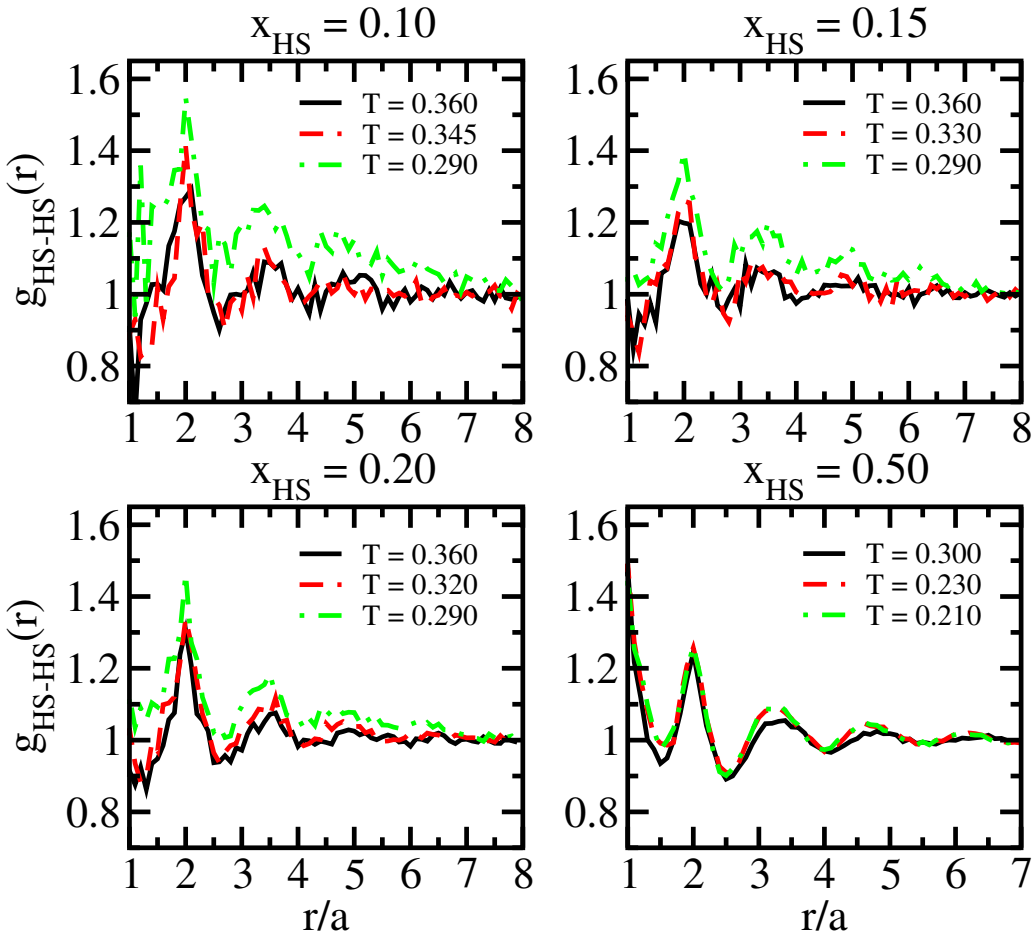

Figure 6.9: HS-HS RDFs for the mixtures with $x_{HS} = 0.10, 0.15, 0.20$ and 0.50 calculated for densities corresponding to the critical value (see Table 6.2). The $g_{\text{HS-HS}}(r)$ are reported for temperatures $T = 0.360, 0.345$ and 0.290 for $x_{HS} = 0.10$, $T = 0.360, 0.330$ and 0.290 for $x_{HS} = 0.15$, $T = 0.360, 0.320$ and 0.290 for $x_{HS} = 0.20$ and $T = 0.300, 0.230$ and 0.210 for $x_{HS} = 0.50$.

Chapter 7

Conclusions

In this brief chapter we summarize the results obtained for the three sets of simulations reported in this thesis, the PR-TIP4P set (Chap. 4), the JJ-TIP4P set (Chap. 5) and the HS-JRP set (Chap. 6). General conclusions are given at the end of the chapter.

7.1 PR-TIP4P set

In this set, molecular dynamics (MD) simulations were performed on TIP4P bulk water and on sodium chloride solutions in TIP4P water, NaCl(aq) [43–48]. The Lennard-Jones (LJ) ion parameters for this set were taken from Pettitt and Rossky [52]. The concentrations investigated are $c = 0.67, 1.36$ and 2.10 mol/kg. The results were also compared with water confined in a hydrophobic environment of soft spheres [54].

Thermodynamics was studied looking at the isochores and the isotherms planes. The analysis of those planes consented the determination of the temperature of maximum density (TMD) line and of the liquid-gas limit of mechanical stability (LG-LMS) line for all the systems investigated. When the concentration is increased, the isochores progressively pack near the LG-LMS line, showing a general downward shift in pressure. This can be connected to the previously observed equivalence of the presence of ions with the application of an external pressure [136, 141, 150, 195]. The study of the isotherms planes of the systems revealed that low temperature isotherms show inflections, crossing higher temperature isotherms, up to the highest concentration investigated. These inflections are indications of the approach of the systems to liquid-liquid coexistence [7, 18]. The width of the density region where these inflections occur, progressively reduces, upon increasing the concentration of salt. Indications of the liquid-liquid coexistence were

confirmed looking at the behaviour of the potential energy as a function of the density, for which minima appear. They can be connected to liquid-liquid coexistence [21]. The minima become closer to each other as concentration is increased. This, together with the restriction of the region of inflections of the isotherms, seems to indicate that the width of the coexistence envelope reduces, upon increasing the salt content.

A comparison of the TMD and of the LG-LMS lines for bulk water, for $c = 0.67, 1.36, 2.10$ mol/kg NaCl(aq) and for water in the hydrophobic environment was also performed. The presence of polar solutes, in the case of NaCl(aq), only mildly affects the LG-LMS that remains fairly similar to that of bulk water. In the case of the apolar solutes, the soft spheres, the LG-LMS shift to higher pressures by about 200 MPa, due to excluded volume effects. The TMD line in the NaCl(aq) solutions progressively moves to lower temperatures and pressures with respect to bulk water, upon increasing concentration. The amplitude of the curve also progressively reduces. In the case of the apolar solutes instead the TMD line moves to lower temperatures but to higher pressures. From this we could hypothesize, that while the addition of solutes always shifts the TMD to lower temperatures, the direction of the shift in temperature may be determined by the polar or apolar nature of the solute.

The structural properties of the $c = 1.36$ mol/kg NaCl(aq) were also compared to the case of water in the hydrophobic confinement of soft spheres. The intermediate concentrations was chosen, because its structure does not differ significantly from the other two concentrations. The hydration structure of the ions and of the soft spheres was compared, at different temperatures and densities. The hydration structure of the two kinds of solutes was also compared inside and outside the region of density anomaly. For soft spheres the hydration shells become more rigid in the anomalous region, with well separated first and second shells. This allows water to maintain its open network, at least at high enough pressures. For ions, in the anomalous region, the hydration shells become more compact, so that water is more effective in screening the ionic charge and more free space is available, at least at low enough temperatures.

7.2 JJ-TIP4P set

This set consists in the extensive MD simulations performed on TIP4P water and on $c = 0.67$ mol/kg NaCl(aq) [49, 50]. The LJ ion parameters for this set were taken from Jensen and Jorgensen [53]. The TIP4P model has been previously widely used for the investigation of water at low temperatures

and it was shown that it can reproduce the phase diagram of the stable ice phase of water [189]. Limits have been found for the position of the liquid-liquid critical point (LLCP) in TIP4P, $T < 200$ K and $P > 70$ K [24], but so far a clear determination of its position was not available.

The large number of state points simulated permitted to locate the position of the LLCP in both systems. The position of the LLCP calculated directly from simulations is $T = 190$ K and $P = 150$ K for bulk water and $T = 200$ K and $P = -50$ K for NaCl(aq). Therefore in the solution the LLCP shifts to lower pressures and higher temperatures. The TIP4P phase diagram calculated in simulations was compared with available experimental data for water. It was found that applying a rigid shift of $\Delta T = +31$ K and $\Delta P = -73$ MPa, the simulated phase diagram can be superimposed to the experimental one. The LLCP for bulk water thus calculated is found at $T = 221$ K and $P = 77$ K, very close the values indicated by Mishima and Stanley [31], $T \simeq 220$ K and $P \simeq 100$ MPa.

Comparing the TMD point at ambient pressure for NaCl(aq) obtained in simulations with the experimental one, we hypothesized that the same shift applied to bulk water, can be applied also to NaCl(aq). Upon performing this shift, the LLCP of the NaCl(aq) falls at $T \simeq 230$ K and $P \simeq -120$ MPa. It can be estimated, extrapolating available experimental data at ambient pressure [41, 68], that the homogeneous nucleation line for $c = 0.67$ mol/kg NaCl(aq) should shift downward by circa 5 K, with respect to bulk water. Thus the LLCP in NaCl(aq) should be found in the experimental accessible region. This finding is important because it shows that the use of solutions can be a viable route to bring the LLCP in a region that can be experimentally investigated in order to definitively proof the validity of the LLCP hypothesis. The comparison of the phase diagrams of bulk water and NaCl(aq) also showed that the ions stabilize the high density liquid (HDL) phase, with a consequent reduction of the extension of the low density liquid (LDL) phase in the solution. This is in agreement with the apparent favored solvation of ions in HDL observed experimentally [133, 134].

The structure of the HDL and LDL phases of bulk water and of NaCl(aq) was also investigated. It was found that the TIP4P model is able to reproduce the LDL and HDL structures when compared to available experimental results [104]. This confirms that the TIP4P model is a very good potential for the study of supercooled water. The comparison of the water-water and ion-water radial distribution functions showed that the LDL phase is more affected by the presence of ions, as already found studying the thermodynamics. From the comparison of the hydration shells, a possible mechanism of disturbance of the LDL phase was found in the substitution of the oxygen atom with the chloride ion in the coordination shells. The ion would pull

inwards the second shell of oxygen atoms, disrupting the ordered LDL structure. This in turn would render the LDL phase less stable, as also indicated by the reduction of its region of existence with respect to bulk water.

7.3 HS-JRP set

The simulations in the HS-JRP were performed with the discrete molecular dynamics (DMD) technique on mixtures of hard spheres (HS) on Jagla ramp potential (JRP) particles [51]. The HS mole fractions investigated are $x_{HS} = 0.10, 0.15, 0.20$ and 0.50. The mixtures are idealized systems for mixtures of water and hydrophobic solutes. The study of the isochores and the isotherms planes revealed the presence of a LLCP up to highest mole fraction investigated, $x_{HS} = 0.50$. The position of the LLCP progressively moves to lower temperatures and higher pressures as the solute content is increased. This shift indicates a progressive increase of the region of existence of the LDL phase and it may be related to the favored solvation of HS in the LDL phase [35].

The liquid-liquid coexistence line of the bulk JRP system has a positive slope, as opposed to water which shows a negative slope. Thus the coexistence line and the mixture critical line were rotated around the LLCP of the bulk JRP system of the angle needed to bring the coexistence line to have the same slope but with reversed sign. Upon applying this rotation, the LLCP of the mixtures is found to shift to higher pressures and temperatures as the mole fraction is increased. Thus we see that the temperature of occurrence of the LLCP could be elevated also using hydrophobic solutes, beyond hydrophilic ones as in the JJ-TIP4P set. In this case also the pressure increases, which might reveal experimentally useful in order to avoid dealing with negative pressures.

The shift of the LLCP to higher temperatures and pressures is also consistent with the results obtained by Gallo and Rovere on water in a hydrophobic environment [54], if we hypothesize that the TMD line and the LLCP get closer to each other in solutions, as in the case of NaCl(aq).

The analysis of the isochores and isotherms planes also showed that while the density anomaly is preserved up to $x_{HS} = 0.20$, it disappears for the highest HS mole fraction, $x_{HS} = 0.50$. Moreover the width of the coexistence envelope becomes narrower when the solute content increases.

The dynamic behaviour of the mixtures was also studied looking at the behaviour of the isotherms of the diffusion coefficient as functions of the density for $x_{HS} = 0.10, 0.15, 0.20, 0.50$ and at the diffusion coefficient at constant pressure calculated along a cooling path above the LLCP for $x_{HS} =$

$0.10, 0.15, 0.20$. The diffusivity anomaly was found to be present up to the highest mole fraction, $x_{HS} = 0.50$, as opposed to the density anomaly. In fact extrema in the behaviour of the isotherms of the diffusion coefficient appear for all mole fractions. Looking at the mixtures with $x_{HS} = 0.10, 0.15, 0.20$, simulated in the same set of densities, we saw that the width of the region of diffusive anomaly reduces upon increasing the HS mole fraction. In analogy with what found for the bulk JRP system [12, 57], we observed a crossover in the behaviour of the diffusion coefficient at constant pressure above the LLCP, from a LDL-like behaviour to a HDL-like behaviour. This crossover can be related to the crossing of the Widom line, above the LLCP. The temperature of occurrence of the crossover decreases upon increasing the HS content.

7.4 General conclusions

The results of the simulations reported in this thesis showed that the anomalies of supercooled water and the appearance of a LLCP are preserved in solutions both of hydrophilic and hydrophobic solutes, at least for concentrations from low to moderate. Therefore the systematic study of the properties of aqueous solutions in the supercooled region could be a novel route to the understanding of the many unsolved mysteries of water. The most debated question on water is probably whether a LLCP actually exists or not. We have seen, in the solutions we studied, that the LLCP occurs at temperatures higher with respect to bulk water and in the experimentally accessible region. Thus an experimental measurement of the LLCP in aqueous solutions, although challenging, appears now possible.

Publications and Presentations

List of publications

1. *Thermodynamic behavior and structural properties of an aqueous sodium chloride solution upon supercooling*

Reference: D. Corradini, P. Gallo and M. Rovere, J. Chem. Phys. **128**, 244508 (2008).

Abstract: We present the results of a molecular dynamics simulation study of thermodynamic and structural properties upon supercooling of a low concentration sodium chloride solution in TIP4P water and the comparison with the corresponding bulk quantities. We study the isotherms and the isochores for both the aqueous solution and bulk water. The comparison of the phase diagrams shows that thermodynamic properties of the solution are not merely shifted with respect to the bulk. Moreover, from the analysis of the thermodynamic curves, both the spinodal line and the temperatures of maximum density curve can be calculated. The spinodal line appears not to be influenced by the presence of ions at the chosen concentration, while the temperatures of maximum density curve displays both a mild shift in temperature and a shape modification with respect to bulk. Signatures of the presence of a liquid-liquid critical point are found in the aqueous solution. By analyzing the water-ion radial distribution functions of the aqueous solution, we observe that upon changing density, structural modifications appear close to the spinodal. For low temperatures, additional modifications appear also for densities close to that corresponding to a low density configurational energy minimum.

2. *Effect of concentration on the thermodynamics of sodium chloride aqueous solutions in the supercooled regime*

Reference: D. Corradini, P. Gallo and M. Rovere, J. Chem. Phys. **130**, 154511 (2009).

Abstract: Molecular dynamics simulations are performed on two sodium chloride solutions in TIP4P water with concentrations c=1.36 mol/kg and c=2.10 mol/kg upon supercooling. The isotherms and isochores planes are calculated. The temperature of maximum

density line and the limit of mechanical stability line are obtained from the analysis of the thermodynamic planes. The comparison of the results shows that for densities well above the limit of mechanical stability, the isotherms and isochores of the sodium chloride aqueous solution shift to lower pressures upon increasing concentration while the limit of mechanical stability is very similar to that of bulk water for both concentrations. We also find that the temperature of maximum density line shifts to lower pressures and temperatures upon increasing concentration. Indications of the presence of a liquid-liquid coexistence are found for both concentrations.

3. *Thermodynamics of supercooled water in solutions*

Reference: D. Corradini, P. Gallo and M. Rovere, J. Phys.: Conference Series **177**, 012003 (2009).

Abstract: Molecular dynamics simulations are performed on bulk TIP4P water and on a low concentration aqueous sodium chloride solution. The thermodynamic properties of the systems are studied by analysing the isotherms and the isochores planes. The comparison of the thermodynamics planes of the two systems reveals that modifications beyond a trivial shift occur in the solution. Moreover the limit of mechanical stability and the temperatures of maximum density line can be calculated from the analysis of the thermodynamic planes. While the limit of mechanical stability results unaffected by the presence of the ions, the temperatures of maximum density line is both mildly shifted in temperature and modified in shape in the solution, with respect to bulk water. Signatures of the presence of liquid-liquid coexistence are found in the aqueous solution. The results are also compared to water in a hydrophobic environment and to water confined between hydrophobic plates.

4. *Structural properties of supercooled sodium chloride aqueous solutions*

Reference: D. Corradini, P. Gallo and M. Rovere, International Journal of Liquid State Sciences (2010). Accepted for publication.

Abstract: The structural properties of sodium chloride aqueous solutions in the supercooled regime are investigated by means of the molecular dynamics simulation technique for two different ions concentrations. The hydration of sodium and chloride ions is analyzed studying the ion-water radial distribution functions and the first shell coordination numbers as a function of the density of the system. The effect of varying the concentration of ions is also evaluated comparing the ion-water radial distribution functions for same density and temperature and different concentrations. It is found that the effect of changing density is analogous for different concentrations. In particular the trend of peaks intensities as a function of density is influenced both by the limit of mechanical stability

and by the approach to the high density liquid phase. We find that upon increasing the salt content ions substitute water molecules in the hydration shell, causing a shift of the secondary shell. We also find that sodium ion induces a more compact water structure around itself while the chloride ion is less effective in reorganizing water structure.

5. *Molecular dynamics studies on the thermodynamics of supercooled sodium chloride aqueous solution at different concentrations*

Reference: D. Corradini, P. Gallo and M. Rovere, J. Phys.: Condens. Matter **22**, 284104 (2010).

Abstract: In this paper we compare recent results obtained by means of molecular dynamics computer simulations on the thermodynamics of TIP4P bulk water and on solutions of sodium chloride in TIP4P water. The concentrations studied are c = 0.67, 1.36 and 2.10 mol kg^{-1}. The results are checked against change of water-salt potential and size effects. The systems are studied in a wide range of temperatures, going from ambient temperature to the supercooled region. Analysis of simulated state points, performed on the isochores and on the isotherm plane, allowed the determination of the limit of mechanical stability and of the temperature of maximum density lines. While the presence of ions in the system does not affect the limit of mechanical stability with respect to the bulk, it causes the temperature of the maximum density line to shift to lower pressure and temperature upon increasing concentration. The occurrence of minima in the trend of potential energy as a function of density and the inflections in the low temperature isotherms suggest the presence of liquid-liquid coexistence for bulk water and for the sodium chloride solutions at all concentrations studied.

6. *Structure and thermodynamics of supercooled aqueous solutions: Ionic solutes compared with water in a hydrophobic environment*

Reference: D. Corradini, P. Gallo and M. Rovere, J. Mol. Liq. (2010). In press.

Abstract: Molecular dynamics results are presented for bulk TIP4P water and for aqueous solutions of sodium chloride at two different concentrations. Thermodynamical and structural properties are calculated in the supercooled region. The behaviour in the thermodynamic plane is compared with the case of water in interaction with a hydrophobic environment. Structural modifications induced by the hydrophilic and hydrophobic interactions are discussed. It is found that the phase diagram of water is shifted in different directions in the case of the hydrophobic system and the ionic solutions. The region

inside the temperatures of the maximum density curve is reduced upon increasing the concentration of ions.

7. *A route to explain water anomalies from results on an aqueous solution of salt*

Reference: D. Corradini, M. Rovere and P. Gallo, J. Chem. Phys. **132**, 134508 (2010).

Abstract: In this paper we investigate the possibility to detect the hypothesized liquid-liquid critical point of water in supercooled aqueous solutions of salts. Molecular dynamics computer simulations are conducted on bulk TIP4P water and on an aqueous solution of sodium chloride in TIP4P water, with concentration c=0.67 mol/kg. The liquid-liquid critical point is found both in the bulk and in the solution. Its position in the thermodynamic plane shifts to higher temperature and lower pressure for the solution. Comparison with available experimental data allowed us to produce the phase diagrams of both bulk water and the aqueous solution as measurable in experiments. Given the position of the liquid-liquid critical point in the solution as obtained from our simulations, the experimental determination of the hypothesized liquid-liquid critical point of water in aqueous solutions of salts appears possible.

8. *Effect of hydrophobic solutes on the liquid-liquid critical point*

Reference: D. Corradini, S. V. Buldyrev, P. Gallo and H. E. Stanley, Phys. Rev. E **81**, 061504 (2010).

Abstract: Jagla ramp particles, interacting through a ramp potential with two characteristic length scales, are known to show in their bulk phase thermodynamic and dynamic anomalies, similar to what is found in water. Jagla particles also exhibit a line of phase transitions separating a low density liquid phase and a high density liquid phase, terminating in a liquid-liquid critical point in a region of the phase diagram that can be studied by simulations. Employing molecular dynamics computer simulations, we study the thermodynamics and the dynamics of solutions of hard spheres (HS) in a solvent formed by Jagla ramp particles. We consider the cases of HS mole fraction x_{HS}=0.10, 0.15, and 0.20, and also the case $x_{HS} = 0.50$ (a 1:1 mixture of HS and Jagla particles). We find a liquid-liquid critical point, up to the highest HS mole fraction; its position shifts to higher pressures and lower temperatures upon increasing x_{HS}. We also find that the diffusion coefficient anomalies appear to be preserved for all the mole fractions studied.

List of presentations

Thermodynamics and liquid-liquid critical point in the supercooled sodium chloride solution

Contributed Talk

Workshop "Modeling and Simulation of Water at Interfaces from Ambient to Supercooled Conditions"

Lausanne (Switzerland), 29th June - 1st July 2009

Thermodynamics and liquid-liquid critical point in the supercooled sodium chloride solution

Contributed Talk

Summer School "CCP5 Methods in Molecular Simulation" - Students' Talks

Sheffield (UK), 5th-14th July 2009

Effects of hydrophobic solutes on the liquid-liquid critical point

Seminar. Held during a three months leave at Center for Polymer Studies - Department of Physics, Boston University (director H. E. Stanley), Boston, MA (USA)

Boston University Water Group Meeting

Boston, MA (USA), 11th March 2010

The liquid-liquid critical point in aqueous solutions

Contributed Talk

International School of Physics "Enrico Fermi" Course CLXXVI "Complex System in Physics and Biology" - Young Researchers' Section

Varenna, LC (Italy), 29th June - 9th July 2010

Thermodynamic behaviour and structural properties of an aqueous sodium chloride solution upon supercooling

Poster Presenter

Acta Biophysica Romana

Rome (Italy), 10th-11th April 2008

Thermodynamics and structural properties of sodium chloride solutions upon supercooling

Poster Presenter

Gordon Research Conference: Water and Aqueous Solutions

Holderness, NH (USA), 27th July - 1st August 2008

Thermodynamics and structural properties of sodium chloride solutions upon supercooling

Poster Presenter

EPS Condensed Matter Division 22 Conference

Rome (Italy), 25th-29th August 2008

Thermodynamics and liquid-liquid critical point in the supercooled sodium chloride solution

Poster Presenter

International Discussion Meeting on Relaxation in Complex Systems

Rome (Italy), 30th August - 5th September 2009

A route to explain water anomalies from results on an aqueous solution of salt

Poster Presenter

International School of Physics "Enrico Fermi" Course CLXXVI "Complex System in Physics and Biology"

Varenna, LC (Italy), 29th June - 9th July 2010

Effect of hydrophobic solutes on the liquid-liquid critical point

Poster Presenter

International School of Physics "Enrico Fermi" Course CLXXVI "Complex System in Physics and Biology"

Varenna, LC (Italy), 29th June - 9th July 2010

Acronyms and abbreviations

In the following we report a list of the acronyms and abbreviations used throughout the thesis together with their meaning (page of first occurrence within bracket). The spelling out of acronyms was given at the first occurrence in each chapter and wherever it was deemed necessary for greater clarity. The TIP4P acronym was spelt out only when comparing to other water potentials (Chap. 4).

LLCP liquid-liquid critical point (7)

LDL low density liquid (8)

HDL high density liquid (8)

PR-TIP4P Set of simulations performed with the molecular dynamics (MD) technique on bulk TIP4P water and on $c = 0.67, 1.36$ and 2.10 mol/kg NaCl(aq) using the Pettitt-Rossky (PR) ion parameters (8).

JJ-TIP4P Set of simulations performed with the molecular dynamics (MD) technique on bulk TIP4P water and on $c = 0.67$ mol/kg NaCl(aq) using the Jensen-Jorgensen (JJ) ion parameters (8).

HS-JRP Set of simulations performed with the discrete molecular dynamics (DMD) technique on mixtures of hard spheres (HS) and Jagla Ramp potential (JRP) particles, with HS mole fraction $x_{HS} = 0.10, 0.15, 0.20$ and 0.50 (8)

MD molecular dynamics (8)

DMD discrete molecular dynamics (8)

PR Pettitt-Rossky (ion parameters) (9)

JJ Jensen-Jorgensen (ion parameters) (9)

HS hard spheres (9)

JRP Jagla ramp potential (9)

TMD temperature of maximum density (9)

LG-LMS liquid-gas limit of mechanical stability (9)

LMS limit of mechanical stability (13).

HDA high density amorphous (23).

LDA low density amorphous (23).

VHDA very high density amorphous (23).

VFT Vogel-Fulcher-Tamman (law) (30)

MCT mode coupling theory (30)

FSC fragile to strong crossover (30)

RDF(s) radial distribution function(s) (35)

LJ Lennard-Jones (45)

ST2 Stillinger and Rahaman potential (55)

SPC simple point charge (55)

SPC/E simple point charge/extended (55)

TIP5P transferable intermolecular potential with five points (55)

TIP4P transferable intermolecular potential with four points (first occurrence 9, spelling out 55)

S spheres (70)

LL-LMS liquid-liquid limit of mechanical stability (87)

Acknowledgments

First, I would like to thank the supervisor of my Ph. D. program and of this Ph. D. thesis, Prof. Paola Gallo. No part of the work presented in this thesis could have been done without her guidance, support and advice. Many thanks go to Prof. Mauro Rovere, with whom I collaborated at Roma Tre University, for his helpful insights and suggestions. I wish also to thank Prof. H. E. Stanley who kindly invited me to spend three months as a visiting Ph. D. student in his very active research group at Center for Polymer Studies, Boston University. His thoughtful advice and the critical reading of the manuscripts of the papers were precious. Also I would like to thank Prof. S. V. Buldyrev of Yeshiva University (New York), with whom I collaborated in Boston, for his help and suggestions.

The computational resources used for the simulations reported in this thesis have been already mentioned in the respective chapters. I wish to acknowledge here again the computational support received by the INFN-Grid at Roma Tre University, by the CNR-IOM Democritos National Simulation Center at SISSA, Trieste (Italy) and by CINECA in the framework of the grant *Progetto Calcolo 891*. I also gratefully acknowledge the usage of the Bethe cluster at Yeshiva University thanks to Prof. S. V. Buldyrev.

Bibliography

[1] P. Ball, *H_2O - A biography of water* (Phoenix, London, 2000).

[2] F. Franks, *Water, a matrix for life* (Royal Society of Chemistry, Cambridge, 2000).

[3] H. E. Stanley, P. Kumar, L. Xu, Z. Yan, M. G. Mazza, S. V. Buldyrev, S.-H. Chen and F. Mallamace, *The puzzling unsolved mysteries of liquid water: Some recent progress*, Physica A **386**, 729 (2007).

[4] P. G. Debenedetti and H. E. Stanley, *Supercooled and Glassy water*, Physics Today **56**, 40 (2003).

[5] P. G. Debenedetti, *Supercooled and glassy water*, J. Phys.: Condens. Matt. **15**, R1669 (2003).

[6] P. G. Debenedetti, *Metastable liquids: Concepts and Principles* (Princeton University Press, Princeton NJ, 1996).

[7] P. H. Poole, F. Sciortino, U. Essmann and H. E. Stanley, *Phase behaviour of metastable water*, Nature **360**, 324 (1992).

[8] S. Sastry, P. G. Debenedetti, F. Sciortino and H. E. Stanley, *Singularity-Free Interpretation of the Thermodynamics of Supercooled Water*, Phys. Rev. E **53**, 6144 (1996).

[9] C. A. Angell, *Insights into Phases of Liquid Water from Study of Its Unusual Glass-Forming Properties*, Science **319**, 582 (2002).

[10] R. J. Speedy, *Stability-limit conjecture. An interpretation of the properties of water*, J. Phys. Chem. **86**, 982 (1982).

[11] O. Mishima and H. E. Stanley, *The relationship between liquid, supercooled and glassy water*, Nature **396**, 329 (1998).

[12] L. Xu, S. V. Buldyrev, C. A. Angell and H. E. Stanley, *Thermodynamics and dynamics of the two-scale spherically symmetric Jagla ramp potential model of anomalous liquids*, Phys. Rev. E **74**, 031108 (2006).

[13] L. Xu, P. Kumar, S. V. Buldyrev, S.-H. Chen, P. H. Poole, F. Sciortino and H. E. Stanley, *Relation between the Widom line and the dynamic crossover in systems with a liquid-liquid phase transition*, Proc. Natl. Acad. Sci. U.S.A. **102**, 16558 (2005).

[14] G. Franzese and H. E. Stanley, *The Widom line of supercooled water*, J. Phys.: Condens. Matter **19**, 205126 (2007).

[15] P. Kumar, G. Franzese and H. E. Stanley, *Predictions of Dynamic Behavior under Pressure for Two Scenarios to Explain Water Anomalies*, Phys. Rev. Lett. **100**, 105701 (2008).

[16] K. Stokely, M. G. Mazza, H. E. Stanley and G. Franzese, *Effect of hydrogen bond cooperativity on the behvior of water*, Proc. Natl. Acad. Sci. U.S.A. **107**, 1301 (2010).

[17] Z. Yan, S. V. Buldyrev, P. Kumar, N. Giovambattista and H. E. Stanley, *Correspondence between phase diagrams of the TIP5P water model and a spherically symmetric repulsive ramp potential with two characteristic length scales*, Phys. Rev. E **77**, 042201 (2008).

[18] P. H. Poole, F. Sciortino, U. Essmann and H. E. Stanley, *Spinodal of liquid water*, Phys. Rev. E **48**, 3799 (1993).

[19] P. H. Poole, F. Sciortino, T. Grande, H. E. Stanley and C. A. Angell, *Effect of Hydrogen Bonds on the Thermodynamic Behavior of Liquid Water*, Phys. Rev. Lett. **73**, 1632 (1994).

[20] P. H. Poole, I. Saika-Voivod and F. Sciortino, *Density minimum and liquid-liquid phase transition*, J. Phys.: Condens. Matter **17**, L431 (2005).

[21] P. Kumar, S. V. Buldyrev, F. W. Starr, N. Giovambattista and H. E. Stanley, *Thermodynamics, structure, and dynamics of water confined between hydrophobic plates*, Phys. Rev. E **72**, 051503 (2005).

[22] D. Paschek, *How the Liquid-Liquid Transition Affects Hydrophobic Hydration in Deeply Supercooled Water*, Phys. Rev. Lett. **94**, 217802 (2005).

[23] D. Paschek, A. Rüppert and A. Geiger, *Thermodynamic and Structural Characterization of the Transformation from a Metastable Low-Density to a Very High-Density Form of Supercooled TIP4P-Ew Model Water*, ChemPhysChem. **9**, 2737 (2008).

[24] F. Sciortino, P. H. Poole, U. Essmann and H. E. Stanley, *Line of compressibility maxima in the phase diagram of supercooled water*, Phys. Rev. E **55**, 727 (1997).

[25] Y. Liu, A. Z. Panagiotopoulos and P. G. Debenedetti, *Low-temperature fluid-phase behavior of ST2 water*, J. Chem. Phys. **131**, 104508 (2009).

[26] M. Yamada, S. Mossa, H. Stanley and F. Sciortino, *Interplay between Time-Temperature Transformation and the Liquid-Liquid Phase Transition in Water*, Phys. Rev. Lett. **88**, 195701 (2002).

[27] P. Jedlovszky and R. Vallauri, *Liquid-vapor and liquid-liquid phase equilibria of the Brodholt-Sampoli-Vallauri polarizable water model*, J. Chem. Phys. **122**, 081101 (2005).

[28] H. Tanaka, *Phase behaviors of supercooled water: Reconciling a critical point of amorphous ices with spinodal instability*, J. Chem. Phys. **105**, 5099 (1996).

[29] S. Harrington, P. H. Poole, F. Sciortino and H. E. Stanley, *Equation of state of supercooled water simulated using the extended simple point charge intermolecular potential*, J. Chem. Phys **107**, 7443 (1997).

[30] T. M. Truskett, P. G. Debenedetti, S. Sastry and S. Torquato, *A single-bond approach to orientation-dependent interactions and its implications for liquid water*, J. Chem. Phys. **111**, 2647 (1999).

[31] O. Mishima and H. E. Stanley, *Decompression-induced melting of ice IV and the liquid-liquid transition in water*, Nature **392**, 164 (1998).

[32] A. Sakai, T. Matsumoto, D. Hirai and T. Niino, *Newly developed encapsulation-dehydration protocol for plant cryopreservation*, CryoLetters **21**, 53 (2000).

[33] F. Franks, *Biophysics and Biochemistry at Low Temperatures* (Cambridge University Press, Cambridge, 1988).

[34] W. Kauzmann, *Some Factors in the Interpretation of Protein Denaturation*, Adv. Protein. Chem. **14**, 1 (1959).

[35] S. V. Buldyrev, P. Kumar, P. G. Debenedetti, P. J. Rossky and H. E. Stanley, *Water-like solvation thermodynamics in a spherically symmetric solvent model with two characteristic lengths*, Proc. Natl. Acad. Sci. U.S.A. **104**, 20177 (2007).

[36] C. Tanford, *The Hydrophobic Effect: Formation of Micelles and Biological Membranes* (Wiley, New York, 1980).

[37] R. L. Scott and P. H. van Konynenburg, *Static properties of solutions. Van der Waals and related models for hydrocarbon mixtures*, Discuss. Faraday Soc. **49**, 87 (1970).

[38] P. H. van Konynenburg and R. L. Scott, *Critical Lines and Phase Equilibria in Binary Van Der Waals Mixtures*, Philos. Trans. R. Soc. London, Ser. A **298**, 495 (1980).

[39] A. I. Abdulagatov, G. V. Stepanov and I. M. Abdulagatov, *Critical Properties of Aqueous Solutions. Part 1: Experimental Data*, Therm. Eng. **55**, 706 (2008).

[40] A. I. Abdulagatov, G. V. Stepanov and I. M. Abdulagatov, *Critical Properties of Aqueous Solutions. P. II*, Therm. Eng. **55**, 795 (2008).

[41] K. Miyata, H. Kanno, T. Niino and K. Tomizawa, *Cationic and anionic effects on the homogeneous nucleation of ice in aqueous alkali halide solutions*, Chem. Phys. Lett. **354**, 51 (2002).

[42] Y. Zhang, A. Faraone, W. A. Kamitakahara, K. H. Liu, C. Y. Mou, J. B. Leão, S. Chang and S.-H. Chen, *Unusual phase behavior of nano-confined water: new insights* (2010). `arXiv:1005.5387v1 [cond-mat.soft]`.

[43] D. Corradini, P. Gallo and M. Rovere, *Thermodynamic behavior and structural properties of an aqueous sodium chloride solution upon supercooling*, J. Chem. Phys. **128**, 244508 (2008).

[44] D. Corradini, P. Gallo and M. Rovere, *Effect of concentration on the thermodynamics of sodium chloride aqueous solutions in the supercooled regime*, J. Chem. Phys. **130**, 154511 (2009).

[45] D. Corradini, P. Gallo and M. Rovere, *Thermodynamics of supercooled water in solutions*, J. Phys: Conference Series **177**, 012003 (2009).

[46] D. Corradini, P. Gallo and M. Rovere, *Structural properties of supercooled sodium chloride aqueous solutions*, International Journal of Liquid State Sciences (2010). Accepted for publication.

[47] D. Corradini, P. Gallo and M. Rovere, *Molecular Dynamics studies on the thermodynamics of the supercooled sodium chloride aqueous solution at different concentrations*, J. Phys: Condens. Matter **22**, 284104 (2010).

[48] D. Corradini, P. Gallo and M. Rovere, *Structure and thermodynamics of supercooled aqueous solutions: Ionic solutes compared with water in a hydrophobic environment*, J. Mol. Liq. (2010). In press.

[49] D. Corradini, M. Rovere and P. Gallo, *A route to explain water anomalies from results on an aqueous solution of salt*, J. Chem. Phys. **132**, 134508 (2010).

[50] D. Corradini, M. Rovere and P. Gallo, *Structural properties of high density and low density water in a supercooled aqueous solution of salt* (2010). In preparation.

[51] D. Corradini, S. V. Buldyrev, P. Gallo and H. E. Stanley, *Effect of hydrophobic solutes on the liquid-liquid critical point*, Phys. Rev. E **81**, 061504 (2010).

[52] B. M. Pettitt and P. J. Rossky, *Alkali halides in water: Ion-solvent correlations and ion-ion potentials of mean force at infinite dilution*, J. Chem. Phys. **84**, 5836 (1986).

[53] K. P. Jensen and W. L. Jorgensen, *Halide, Ammonium and Alkali Metal Ion Parameters for Modeling Aqueous Solutions*, J. Chem. Theory Comput. **2**, 1499 (2006).

[54] P. Gallo and M. Rovere, *Structural properties and liquid spinodal of water confined in a hydrophobic environment*, Phys. Rev. E **76**, 061202 (2007).

[55] E. A. Jagla, *Phase behavior of a system of particles with core collapse*, Phys. Rev. E **58**, 1478 (1998).

[56] E. A. Jagla, *Core-softened potentials and the anomalous properties of water*, J. Chem. Phys. **111**, 8980 (1999).

[57] L. Xu, S. V. Buldyrev, N. Giovambattista, C. A. Angell and H. E. Stanley, *A monatomic system with a liquid-liquid critical point and two distinct glassy states*, J. Chem. Phys. **130**, 054505 (2009).

[58] Z. Yan, S. V. Buldyrev, N. Giovambattista and H. E. Stanley, *Structural Order for One-Scale and Two-Scale Potentials*, Phys. Rev. Lett. **95**, 130604 (2005).

[59] Z. Yan, S. V. Buldyrev, N. Giovambattista, P. G. Debenedetti and H. E. Stanley, *Family of tunable spherically symmetric potentials that span the range from hard spheres to waterlike behavior*, Phys. Rev. E **73**, 051204 (2006).

[60] J. B. Hasted, *Liquid water: Dielectric properties - in Water A comprehensive treatise*, page 255 (Plenum Press, New York, 1972). Ed. F. Franks.

[61] A. G. Császár, G. Czakó, T. Furtenbacher, J. Tennyson, V. Szlay, S. V. Shirin, N. F. Zobov and O. L. Polyansky, *On equilibrium structures of water molecules*, J. Chem. Phys. **122**, 214305 (2005).

[62] F. Martin and H. Zipse, *Charge distribution in the water molecule - A comparison of methods*, J. Comput. Chem. **26**, 97 (2005).

[63] F. Lovas, *Microwave spectral tables II. Triatomic molecules*, J. Chem. Ref. Data **7**, 1445 (1978).

[64] L. Pauling, *General Chemistry* (Dover, New York, 1970).

[65] V. Aquilanti, E. Cornicchi, M. M. Teixidor, N. Saendig, F. Pirani and D. Cappelletti, *Glory-Scattering Measurement of Water-Noble-Gas Interactions: The Birth of the Hydrogen Bond*, Angew. Chem. Int. Ed. **44**, 2536 (2005).

[66] V. F. Petenko and R. W. Whitworth, *Physics of Ice* (Oxford Univeristy Press, Oxford, 1999).

[67] C. G. Salzmann, P. G. Radaelli, E. Mayer and J. L. Finney, *Ice XV: A New Thermodynamically Stable Phase of Ice*, Phys. Rev. Lett. **103**, 105701 (2009).

[68] H. Kanno, R. J. Speedy and C. A. Angell, *Supercooling of Water to -92° C Under Pressure*, Science **189**, 880 (1975).

[69] C. A. Angell, *Liquid Fragility and the Glass Transition in Water and Aqueous Solutions*, Chem. Rev. **102**, 2627 (2002).

[70] T. Loerting, C. Salzmann, I. Kohl, E. Mayer and A. Hullbrucker, *A 2nd Distinct Structural State Of High-Density Amorphous Ice At 77 K And 1 Bar*, Phys. Chem. Chem. Phys. **3**, 5355 (2001).

[71] F. Franks, *Water...a Comprehensive Treatise - vol. 7* (Plenum Press, New York, 1982).

[72] E. Mayer, *New method for vitrifying water and other liquids by rapid cooling of their aerosols*, J. Appl. Phys. **58**, 663 (1985).

[73] O. Mishima, L. D. Calvert and E. Whalley, *Melting ice at 77 K and 10 kbar: a new method for making amorphous solids*, Nature **310**, 393 (1984).

[74] K. Winkel, M. S. Elsaesser, E. Mayer and T. Loerting, *Water polyamorphism: Reversibility and (dis)continuity*, J. Chem. Phys. **128**, 044510 (2008).

[75] P. Ball, *Water - an enduring mistery*, Nature **452**, 291 (2008).

[76] See http://www1.lsbu.ac.uk/water/index2.html for more details.

[77] C. A. Angell and H. Kanno, *Density Maxima in High-Pressure Supercooled Water and Liquid Silicon Dioxide*, Science **193**, 1121 (1976).

[78] R. A. Fine and F. J. Millero, *The high pressure PVT properties of deuterium oxide*, J. Chem. Phys. **63**, 89 (1975).

[79] D. Liu, Y. Zhang, C.-C. Chen, C.-Y. Mou, P. Poole and S.-H. Chen, *Observation of the density minimum in deeply supercooled confined water*, Proc. Natl. Acad. Sci. U.S.A. **104**, 9570 (2007).

[80] F. Mallamace, C. Branca, M. Broccio, C. Corsaro, C.-Y. Mou and S.-H. Chen, *The anomalous behavior of the density of water in the range 30 K < T < 373 K*, Proc. Natl. Acad. Sci. U.S.A. **104**, 18387 (2007).

[81] H. Kanno and C. A. Angell, *Water: Anomalous compressibilities to 1.9 kbar and correlation with supercooling limits*, J. Chem. Phys. **70**, 4008 (1979).

[82] C. A. Angell, W. J. Sichina and M. Oguni, *Heat capacity of water at extremes of supercooling and superheating*, J. Phys. Chem. **86**, 998 (1982).

[83] H. Kanno and C. A. Angell, *Volumetric and derived thermal characteristics of liquid D_2O at low temperatures and high pressures*, J. Chem. Phys. **73**, 1940 (1980).

[84] R. J. Speedy and C. A. Angell, *Isothermal compressibility of supercooled water and evidence for a thermodynamic singularity at 45° C*, J. Chem. Phys. **65**, 851 (1976).

[85] J. R. Errington and P. G. Debenedetti, *Relationship between structural order and the anomalies of liquid water*, Nature **409**, 318 (2001).

[86] A. B. de Oliveira, G. Franzese, P. A. Netz and M. Barbosa, *Waterlike hierarchy of anomalies in a continuous spherical shouldered potential*, J. Chem. Phys. **128**, 064901 (2008).

[87] W. Kob, *Computer simulations of supercooled liquids and glasses*, J. Phys.: Condens. Matter **11**, R85 (1999).

[88] W. Götze and L. Sjogren, *Relaxation processes in supercooled liquids*, Rep. Prog. Phys. **55**, 241 (1992).

[89] W. Götze, *Complex Dynamics of Glass-Forming Liquids: A Mode Coupling Theory* (Oxford University Press, Oxford, 2009).

[90] P. Gallo, M. Rovere and E. Spohr, *Supercooled confined water and the mode coupling crossover temperature*, Phys. Rev. Lett. **85**, 4317 (2000).

[91] P. Gallo, M. Rovere and E. Spohr, *Glass transition and layering effects in confined water: A computer simulation study*, J. Chem. Phys. **113**, 11324 (2000).

[92] L. Liu, S.-H. Chen, A. Faraone, C.-W. Yen and C.-Y. Mou, *Pressure Dependence of Fragile-to-Strong Transition and a Possible Second Critical Point in Supercooled Confined Water*, Phys. Rev. Lett. **95**, 117802 (2005).

[93] F. Mallamace, M. Broccio, C. Corsaro, A. Faraone, U. Wanderlingh, L. Liu, C.-Y. Mou and S.-H. Chen, *The fragile-to-strong dynamic crossover transition in confined water: nuclear magnetic resonance results*, J. Chem. Phys. **124**, 161102 (2006).

[94] A. Faraone, L. Liu, C.-Y. Mou, C.-W. Wen and S.-H. Chen, *Fragile-to-strong liquid transition in deeply supercooled confined water*, J. Chem. Phys. **121**, 10843 (2004).

[95] Y. Zhang, M. Lagi, E. Fratini, P. Baglioni, E. Mamontov and S.-H. Chen, *Dynamic susceptibility of supercooled water and its relation to the dynamic crossover phenomenon*, Phys. Rev. E **79**, 040201(R) (2009).

[96] L. Liu, S.-H. Chen, A. Faraone, C.-W. Yen, C.-Y. Mou, A. I. Kolesnikov, E. Mamontov and J. Leão, *Quasielastic and inelastic neutron scattering investigation of fragile-to-strong crossover in deeply supercooled water confined in nanoporous silica matrices*, J. Phys.: Condens. Matter **18**, S2261 (2006).

[97] P. Gallo, F. Sciortino, P. Tartaglia and S.-H. Chen, *Slow Dynamics of Water Molecules in Supercooled States*, Phys. Rev. Lett. **76**, 2730 (1996).

[98] P. Gallo, M. Rovere and S.-H. Chen, *Dynamic Crossover in Supercooled Confined Water: Understanding Bulk Properties through Confinement*, J. Phys. Chem. Lett. **1**, 729 (2010).

[99] P. Kumar, G. Franzese and H. E. Stanley, *Dynamics and thermodynamics of water*, J. Phys.: Condens. Matter **20**, 244114 (2008).

[100] S.-H. Chen, F. Mallamace, C.-Y. Mou, M. Broccio, C. Corsaro, A. Faraone and L. Liu, *The violation of the Stokes-Einstein relation in supercooled water*, Proc. Natl. Acad. Sci. U.S.A. **103**, 12974 (2006).

[101] F. Mallamace, C. Branca, C. Corsaro, N. Leone, J. Spooren, H. E. Stanley and S.-H. Chen, *Dynamical Crossover and Breakdown of the Stokes-Einstein Relation in Confined Water and in Methanol-Diluted Bulk Water*, J. Phys. Chem. B **114**, 1870 (2010).

[102] Z. Yan, S. V. Buldyrev, P. Kumar, N. Giovambattista, P. G. Debenedetti and H. E. Stanley, *Structure of the first- and second-neighbor shells of simulated water: Quantitative relation to translational and orientational order*, Phys. Rev. E **76**, 051201 (2007).

[103] M. A. Anisimov, J. V. Sengers and J. M. H. Levelt-Sengers, *Near-critical behavior of aqueous systems - in Aqueous Systems at Elevated Temperatures and Pressures: Physical Chemistry in Water, Steam and Hydrothermal Solutions* (Academic Press, Elsevier, Amsterdam, 2004). Eds. D. A. Palmer, R. Fernandez-Prini and A. H. Harvey.

[104] A. K. Soper and M. A. Ricci, *Structures of high-density and low-density water*, Phys. Rev. Lett. **84**, 2881 (2000).

[105] D. Banarjee, S. N. Bhat, S. V. Bhat and D. Leporini, *ESR evidence for 2 coexisting liquid phases in deeply supercooled bulk water*, Proc. Natl. Acad. Sci. U.S.A. **106**, 11448 (2009).

[106] R. J. Speedy, P. G. Debenedetti, S. R. Smith, C. Huang and B. D. Kay, *The evaporation rate, free energy, and entropy of amorphous water at 150 K*, J. Chem. Phys. **105**, 240 (1996).

[107] I. Brovchenko, A. Geiger and A. Oleinikova, *Liquid-liquid phase transitions in supercooled water studied by computer simulations of various water models*, J. Chem. Phys. **123**, 044515 (2005).

[108] L. Xu, I. Ehrenberg, S. V. Buldyrev and H. E. Stanley, *Relationship between the Liquid-Liquid Phase Transition and Dynamic Behavior in the Jagla Model*, J. Phys.: Condens. Matter **18**, S2239 (2006).

[109] P. Kumar, S. V. Buldyrev, F. Sciortino, E. Zaccarelli and H. E. Stanley, *Static and dynamic anomalies in a repulsive spherical ramp liquid: Theory and simulation*, Phys. Rev. E **72**, 021501 (2005).

[110] M. Canpolat, F. W. Starr, M. R. Sadr-Lahijany, A. Scala, O. Mishima, S. Havlin and H. E. Stanley, *Local Structural Heterogeneities in Liquid Water under Pressure*, Chem. Phys. Lett. **294**, 9 (1998).

[111] M. R. Sadr-Lahijany, A. Scala, S. V. Buldyrev and H. E. Stanley, *Liquid State Anomalies for the Stell-Hemmer Core-Softened Potential*, Phys. Rev. Lett. **81**, 4895 (1998).

[112] H. M. Gibson and N. B. Wilding, *Metastable liquid-liquid coexistence and density anomalies in a core-softened fluid*, Phys. Rev. E **73**, 061507 (2006).

[113] E. Lomba, N. G. Almarza, C. Martin and C. McBride, *Phase behavior of attractive and repulsive ramp fluids: Integral equation and computer simulation studies*, J. Chem. Phys. **126**, 244510 (2007).

[114] B. Bernu, J.-P. Hansen, Y. Hiwatari and G. Pastore, *Soft-sphere model for the glass transition in binary alloys: Pair structure and self-diffusion*, Phys. Rev. A **36**, 4891 (1987).

[115] G. Pastore, B. Bernu, J.-P. Hansen and Y. Hiwatari, *Soft-sphere model for the glass transition in binary alloys: II. Relaxation of the incoherent density-density correlation functions*, Phys. Rev. A **38**, 454 (1988).

[116] J. Fornleitner and G. Kahl, *Lane formation vs. cluster formation in two-dimensional square-shoulder systems - A genetic algorithm approach*, EPL **82**, 18001 (2008).

[117] G. Malescio and G. Pellicane, *Stripe patterns in two-dimensional systems with core-corona molecular architecture*, Phys. Rev. E **70**, 021202 (2004).

[118] S. V. Buldyrev, G. Malescio, C. A. Angell, N. Giovambattista, S. Prestipino, F. Saija, H. E. Stanley and L. Xu, *Unusual Phase Behavior of One-Component Systems with Two-Scale Isotropic Interaction*, J. Phys.:Condens. Matter **21**, 504106 (2009).

[119] S. Sastry and C. A. Angell, *Liquid-liquid phase transition in supercooled silicon*, Nature Materials **2**, 739 (2003).

[120] H. Bhat, V. Molinero, V. Solomon, E. Soignard, S. Sastry, J. L. Yarger and C. A. Angell, *Vitrification of a monatomic metallic liquid*, Nature **448**, 787 (2007).

[121] I. Saika-Voivod, P. H. Poole and F. Sciortino, *Fragile-to-strong transition and polyamorphism in the energy landscape of liquid silica*, Nature **412**, 514 (2001).

[122] M. Hemmati, C. T. Moynihan and C. A. Angell, *Interpretation of the molten BeF_2 viscosity anomaly in terms of a high temperature density maximum, and other waterlike features*, J. Chem. Phys. **115**, 6663 (2001).

[123] J. S. Tse and D. K. Klug, *Structure and dynamics of liquid sulphur*, Phys. Rev. B **59**, 34 (1999).

[124] Y. Katayama, *XAFS study on liquid selenium under high pressure*, J. Synchrotron. Rad. **8**, 182 (2001).

[125] J.-M. Zanotti, M.-C. Bellissent-Funel and S.-H. Chen, *Relaxational dynamics of supercooled water in porous glass*, Phys. Rev. E **59**, 3084 (1999).

[126] L. P. N. Rebelo and P. G. Debenedetti, *Singularity-free interpretation of the thermodynamics of supercooled water. II. Thermal and volumetric behavior*, J. Chem. Phys. **109**, 626 (1998).

[127] C. A. Angell and J. E. Sare, *Glass-Forming Composition Regions and Glass Transition Temperatures for Aqueous Electrolyte Solutions*, J. Chem. Phys. **52**, 1058 (1970).

[128] S. Chatterjee, H. S. Ashbaugh and P. G. Debenedetti, *Effects on non-polar solutes on the thermodynamic response functions of aqueous mixtures*, J. Chem. Phys **123**, 164503 (2005).

[129] S. Chatterjee and P. G. Debenedetti, *Fluid-phase behavior of binary mixtures in which one component can have two critical points*, J. Chem. Phys **124**, 154503 (2006).

[130] T. Koop, H. P. Ng, L. T. Molina and M. J. Molina, *A New Optical Technique to Study Aerosol Phase Transitions: The Nucleation of Ice from H_2SO_4 Aerosols*, J. Phys. Chem. A **102**, 8924 (1998).

[131] D. G. Archer and R. W. Carter, *Thermodynamic Properties of the $NaCl + H_2O$ System. 4. Heat Capacities of H_2O and NaCl(aq) in Cold-Stable and Supercooled States*, J. Phys. Chem. B **104**, 8563 (2000).

[132] R. W. Carter and D. G. Archer, *Heat capacity of $NaNO_3$(aq) in stable and supercooled states. Ion association in the supercooled solution*, Phys. Chem. Chem. Phys. **2**, 5138 (2000).

[133] R. Souda, *Liquid-liquid transition in supercooled water investigated by interaction with LiCl and Xe*, J. Chem. Phys. **125**, 181103 (2006).

[134] O. Mishima, *Phase separation in dilute LiCl-H_2O solution related to the polyamorphism of liquid water*, J. Chem. Phys. **126**, 244507 (2007).

[135] O. Mishima, *Application of polyamorphism in water to spontaneous crystallization of emulsified LiCl-H_2O solution*, J. Chem. Phys. **123**, 154506 (2005).

[136] R. Mancinelli, A. Botti, F. Bruni, M. A. Ricci and A. K. Soper, *Perturbation of water structure due to monovalent ions in solution*, Phys. Chem. Chem. Phys. **9**, 2959 (2007).

[137] J. D. Smith, R. J. Saykally and P. L. Geissler, *The Effects of Dissolved Halide Anions on Hydrogen Bonding in Liquid Water*, J. Am. Chem. Soc. **129**, 13847 (2007).

[138] A. K. Soper and K. Weckström, *Ion solvation and water structure in potassium halide aqueous solutions*, Biophys. Chem. **124**, 180 (2006).

[139] Y. J. Lü and B. Wei, *Supercooling of aqueous NaCl and KCl solutions under acoustic levitation*, J. Chem. Phys. **125**, 144503 (2006).

[140] S. Imberti, A. Botti, F. Bruni, G. Cappa, M. A. Ricci and A. K. Soper, *Ions in water: The microscopic structure of concentrated hydroxide solutions*, J. Chem. Phys. **122**, 194509 (2005).

[141] A. Botti, F. Bruni, S. Imberti, M. A. Ricci and A. K. Soper, *Ions in water: The microscopic structure of concentrated NaOH solutions*, J. Chem. Phys. **120**, 10154 (2004).

[142] R. Mancinelli, A. Botti, F. Bruni and M. A. Ricci, *Hydration of Sodium, Potassium, and Chloride Ions in Solutions and the Concept of Structure Maker/Breaker*, J. Phys. Chem. B **111**, 13570 (2007).

[143] Y. Georgalis, A. M. Kierzek and W. Saenger, *Cluster Formation in Aqueous Electrolyte Solutions Observed by Dynamic Light Scattering*, J. Phys. Chem. B **104**, 3405 (2000).

[144] G. W. Neilson, P. E. Mason, S. Ramos and D. Sullivan, *Neutron and X-ray scattering studies of hydration in aqueous solutions*, Philos. Trans. R. Soc. London, Ser. A **359**, 1575 (2001).

[145] H. Ohtaki, *Ionic solvation in aqueous and nonaqueous solutions*, Monatshefte für Chemie **132**, 1237 (2001).

[146] B. Hribar, N. T. Southall, V. Vlachy and K. A. Dill, *How Ions Affect the Structure of Water*, J. Am. Chem. Soc. **124**, 12302 (2002).

[147] S. Koneshan and J. C. Rasaiah, *Computer simulation studies of aqueous sodium chloride solutions at 298 K and 683 K*, J. Chem. Phys. **113**, 8125 (2000).

[148] J. S. Kim and J. Yethiraj, *Diffusive Anamaly of Water in Aqueous Sodium Chloride Solutions at Low Temperatures*, J. Phys. Chem. B **112**, 1729 (2008).

[149] H. Du, J. C. Rasaiah and J. D. Miller, *Structural and Dynamic Properties of Concentrated Alkali Halide Solutions: A Molecular Dynamics Simulation*, J. Phys. Chem B **111**, 209 (2007).

[150] J. Holzmann, R. Ludwig, A. Geiger and D. Paschek, *Temperature and Concentration Effects on the Solvophobic Solvation of Methane in Aqueous Salt Solutions*, ChemPhysChem. **9**, 2722 (2008).

[151] P. J. Lenart, A. Jusufi and A. Z. Panagiotopoulos, *Effective potentials for 1:1 electrolyte solutions incorporating dielectric saturation and repulsive hydration*, J. Chem. Phys. **126**, 044509 (2007).

[152] J. Alejandre and J.-P. Hansen, *Ions in water: From ion clustering to crystal nucleation*, Phys. Rev. E **76**, 061505 (2007).

[153] B. Gu, F. S. Zhang, Z. P. Wang and Y. Zhou, *The solvation of NaCl in model water with different hydrogen bond strength*, J. Chem. Phys. **129**, 184505 (2008).

[154] P. Auffinger, T. E. Cheatham-III and A. C. Vaiana, *Spontaneous Formation of KCl Aggregates in Biomolecular Simulations: A Force Field Issue?*, J. Chem. Theory Comput. **3**, 1851 (2007).

[155] M. Patra and M. Karttunen, *Systematic comparison of force fields for microscopic simulations of NaCl in aqueous solutions: Diffusion, free energy of hydration, and structural properties*, J. Comput. Chem. **25**, 678 (2004).

[156] I. S. Joung and T. E. Cheatham-III, *Determination of alkali and halide monovalent ion parameters for use in explicitly solvated biomolecular simulations*, J. Phys. Chem. B **112**, 9020 (2008).

[157] S. Koneshan, J. C. Rasaiah, R. M. Lynden-Bell and S. H. Lee, *Solvent Structure, Dynamics, and Ion Mobility in Aqueous Solutions at 25° C*, J. Phys. Chem. B **102**, 4193 (1998).

[158] S. Chowdhuri and A. Chandra, *Molecular dynamics simulations of aqueous NaCl and KCl solutions: Effects of ion concentration on the single-particle, pair, and collective dynamical properties of ions and water molecules*, J. Chem. Phys. **115**, 3732 (2001).

[159] S. Chowdhuri and A. Chandra, *Hydration structure and diffusion of ions in supercooled water: Ion size effects*, J. Chem. Phys. **118**, 9719 (2003).

[160] K. Lum, D. Chandler and J. D. Weeks, *Hydrophobicity at Small and Large Length Scales*, J. Phys. Chem. B **103**, 4570 (1999).

[161] H. S. Ashbaugh, S. Garde, G. Hummer, E. W. Kaler and M. E. Paulaitis, *Conformational Equilibria of Alkanes in Aqueous Solution: Relationship to Water Structure Near Hydrophobic Solutes*, Biophys. J. **77**, 645 (1999).

[162] H. S. Ashbaugh, T. M. Truskett and P. G. Debenedetti, *A simple molecular thermodynamic theory of hydrophobic hydration*, J. Chem. Phys. **116**, 2907 (2002).

[163] H. S. Ashbaugh and L. R. Pratt, *Colloquium: Scaled particle theory and the length scales of hydrophobicity*, Rev. Mod. Phys. **78**, 159 (2006).

[164] F. H. Stillinger and A. Rahman, *Improved simulation of liquid water by molecular dynamics*, J. Chem. Phys. **60**, 1545 (1974).

[165] L. R. Pratt and D. Chandler, *Theory of the hydrophobic effect*, J. Chem. Phys. **67**, 3683 (1977).

[166] L. R. Pratt, *Molecular Theory of the Hydrophobic Effect: "She is too mean to have her name repeated"*, Annu. Rev. Phys. Chem. **53**, 409 (2002).

[167] S. Garde, G. Hummer, A. E. García, M. E. Paulaitis and L. R. Pratt, *Origin of Entropy Convergence in Hydrophobic Hydration and Protein Folding*, Phys. Rev. Lett. **77**, 4966 (1996).

[168] G. Hummer, S. Garde, A. E. García, A. Pohorille and L. R. Pratt, *An information theory model of hydrophobic interactions*, Proc. Natl. Acad. Sci. U.S.A. **93**, 8951 (1996).

[169] G. Hummer, S. Garde, A. E. García, M. E. Paulaitis and L. R. Pratt, *Hydrophobic Effects on a Molecular Scale*, J. Phys. Chem. B **102**, 10649 (1998).

[170] S. Rajamani, T. M. Truskett and S. Garde, *Hydrophobic hydration from small to large lengthscales: Understanding and manipulating the crossover*, Proc. Natl. Acad. Sci. U.S.A. **102**, 9475 (2005).

[171] B. Widom, P. Bhimalapuram and K. Koga, *The hydrophobic effect*, Phys. Chem. Chem. Phys. **5**, 3085 (2003).

[172] E. Wilhelm, R. Battino and R. J. Wilcox, *Low-pressure solubility of gases in liquid water*, Chem. Rev. **77**, 219 (1977).

[173] E. V. Ivanov, E. J. Lebedeva, V. K. Abrosimov and N. G. Ivanova, *Structural contribution to the effect of hydrophobic hydration of noble gases*, J. Struct. Chem. **46**, 253 (2005).

[174] N. Metropolis, A. W. Rosenbluth, M. N. Rosenbluth, A. H. Teller and E. Teller, *Equation of state Calculations by Fast Computing Machines*, J. Chem. Phys. **21**, 1087 (1953).

[175] B. J. Alder and T. E. Wainwright, *Phase Transition for a Hard Sphere System*, J. Chem. Phys. **27**, 1208 (1957).

[176] A. Rahman, *Correlation in the Motion of Atoms in liquid Argon*, Phys. Rev. A **136**, 405 (1964).

[177] J.-P. Hansen and I. R. McDonald, *Theory of Simple Liquids* (Academic Press, London, 1990).

[178] M. P. Allen and D. J. Tildesley, *Computer simulation of liquids* (Clarendon, Oxford, 1987).

[179] W. Smith, T. R. Forester and I. T. Todorov, *The DL_POLY_2.0 User Manual*, Daresbury Laboratory, Daresbury, UK (2006).

[180] W. G. Hoover, *Canonical Dynamics: Equilibrium phase-space distributions*, Phys. Rev. A **31**, 1695 (1985).

[181] H. J. C. Berendsen, J. P. M. Postma, W. F. van Gunsteren, A. DiNola and J. R. Haak, *Molecular dynamics with coupling to an external bath*, J. Chem. Phys. **81**, 3684 (1984).

[182] D. J. Evans and G. P. Morris, *Non-Newtonian Molecular Dynamics*, Computer Physics Reports **1**, 297 (1984).

[183] S. Melchionna, G. Ciccotti and B. L. Holian, *Hoover NPT dynamics for systems varying in shape and size*, Molecular Physics **78**, 533 (1993).

[184] B. Guillot, *A reppraisal of what we have learnt during three decades of computer simulations on water*, J. Mol. Liq. **101**, 219 (2002).

[185] H. J. C. Berendsen, J. P. M. Postma, W. F. van Gunsteren and J. Hermans, *Intermolecular Forces*, page 331 (Reidel, Dordrecht, 1981). Edited by B. Pullman.

[186] H. J. C. Berendsen, J. F. Grigera and T. P. Straatsma, *The missing term in effective pair potentials*, J. Chem. Phys. **91**, 6269 (1987).

[187] M. W. Mahoney and W. L. Jorgensen, *A five-site model for liquid water and the reprodcution of the density anomaly by rigid, nonpolarizable potential functions*, J. Chem. Phys. **112**, 8910 (2000).

[188] W. L. Jorgensen, J. Chandrasekhar, J. D. Madura, R. W. Impey and M. L. Klein, *Comparison of simple potential functions for simulating liquid water*, J. Chem. Phys. **79**, 926 (1983).

[189] E. Sanz, C. Vega, J. L. F. Abascal and L. G. MacDowell, *Phase Diagram of Water from Computer Simulation*, Phys. Rev. Lett. **92**, 255701 (2004).

[190] M. L. Huggins and J. E. Mayer, *Interatomic Distances in Crystals of the Alkali Halides*, J. Chem. Phys. **1**, 643 (1933).

[191] F. G. Fumi and M. P. Tosi, *Ionic sizes and Born repulsive parameters in the NaCl-type alkali halides*, J. Phys. Chem. Solids **25**, 45 (1964).

[192] C. Vega, E. Sanz and J. L. F. Abascal, *The melting temperature of the most common models of water*, J. Chem. Phys. **122**, 114507 (2005).

[193] See http://web-cluster.fis.uniroma3.it/ for more details.

[194] See http://doc.escience-lab.org/index.php/HPC/MainPage for more details.

[195] J. Holzmann, R. Ludwig, D. Paschek and A. Geiger, *Pressure and Salt Effects in Simulated Water: Two Sides of the Same Coin?*, Angew. Chem. Int. Ed. **46**, 8907 (2007).

[196] See https://hpc.cineca.it/docs/old-guides/IBMBCXStartUp for more details.

[197] See https://hpc.cineca.it/docs/guide2010/31IBMSP6UserGuide for more details.

[198] See http://www.open-mpi.org/ for more details.

[199] S. J. Henderson and R. J. Speedy, *Temperature of maximum density in water at negative pressure*, J. Phys. Chem. **91**, 3062 (1987).

[200] NIST Chemistry WebBook, *Thermophysical Properties of Fluid Systems* (2008). URL `http://webbook.nist.gov/chemistry/fluid/`.

[201] P. G. Hill, *A Unified Fundamental Equation for the Thermodynamic Properties of H_2O*, J. Phys. Chem. Ref. Data **19**, 1233 (1990).

[202] J. L. F. Abascal, E. Sanz, R. G. Fernández and C. Vega, *A potential model for the study of ices and amorphous water: TIP4P/Ice*, J. Chem. Phys. **122**, 234511 (2005).

[203] J. L. Green, D. J. Durben, G. H. Wolf and C. A. Angell, *Water and Solutions at Negative Pressure: Raman Spectroscopic Study to -80 Megapascals*, Science **249**, 649 (1990).

[204] E. Mamontov, *Diffusion Dynamics of Water Molecules in a LiCl Solution: A Low-Temperature Crossover*, J. Phys. Chem. B **113**, 14073 (2009).

[205] M. C. Bellissent-Funel and L. Bosio, *A neutron scattering study of liquid D_2O under pressure and at various temperatures*, J. Chem. Phys. **102**, 3727 (1995).

[206] M. C. Bellissent-Funel, L. Bosio, A. Hullbrucker, R. Sridi-Dorbez and E. Mayer, *X-ray and neutron scattering studies of the structure of hyperquenched glassy water*, J. Chem. Phys. **97**, 1282 (1992).

[207] M. C. Bellissent-Funel, J. Texeira, L. Bosio and J. C. Dore, *A structural study of deeply supercooled water*, J. Phys.: Condens. Matter **1**, 7123 (1992).

[208] S. V. Buldyrev and H. E. Stanley, *A system with multiple liquid-liquid critical points*, Physica A **330**, 124 (2003).

[209] F. W. Starr, C. A. Angell and H. E. Stanley, *Prediction of entropy and dynamic properties of water below the homogeneous nucleation temperature*, Physica A **323**, 51 (2003).